Seasonality of the Agulhas Current with respect to near- and far-field winds

Katherine Hutchinson

Supervised by: Pierrick Penven, Lisa Beal, Isabelle Ansorge, and Juliet Hermes

A thesis presented for the degree of Doctor of Philosophy

February 2018

Abstract

The Agulhas Current plays a critical role in both local and global ocean circulation and climate regulation, yet the mechanisms that determine the seasonal cycle of the current remain poorly understood. Model studies predict an austral winter-spring maximum in poleward volume transport, whilst observations reveal an austral summertime (February-March) maximum. Here, the role of winds on Agulhas Current seasonality is investigated using shallow water models, satellite measurements, and a 23-year transport proxy based on observations. A one-and-a-half layer reduced gravity model is shown to successfully reproduce the seasonal phasing of the current. This seasonality is found to be highly sensitive to the propagation speed of Rossby waves, which determines the arrival time of the wind stress signal at the western boundary. By matching Rossby wave speeds to those observed using altimetry, an Agulhas Current with a maximum flow in February and a minimum flow in July is simulated, agreeing well with observations. Near-field winds, to the west of 35°E, dominate this seasonality, as signals from more remote wind forcing dissipate due to destructive interference while crossing the basin. Local winds driving coastal upwelling/downwelling directly over the Agulhas cannot, alone, account for the observed seasonal phasing, as they force a November-December maximum and June minimum in flow. The seasonal response to Indian Ocean winds is also investigated using a barotropic (single layer) model with realistic topography. A barotropic adjustment cannot explain the observed Agulhas Current seasonality, predicting a wintertime maximum in transport. The results from the barotropic simulation are similar to previous model studies, where seasonality is dominated by a southward propagation of signals via the Mozambique Channel, suggesting that these models are too barotopic in their response to the winds. Findings from this study elucidate the role of near-field winds and baroclinic processes in determining the seasonality of the Agulhas Current.

Plagiarism Declaration

This thesis is my own research work. Wherever contributions from others are involved, every effort has been made to indicate this clearly, with due reference to the literature. Aside from guidance from my supervisors, I have received no assistance except as acknowledged.

I have not allowed, and will not allow, anyone to copy the contents of this thesis with the intention of passing it off as their own work.

Signed by candidate

Contents

List of Figures **11**

List of Symbols **12**

List of Acronyms **13**

1 Introduction **14**

2 Literature Review **17**

2.1 The Indian Ocean 17

2.2 The Agulhas Current 19

2.3 Sverdrup Dynamics 25

2.4 Rossby Planetary Waves 28

2.5 The Reduced Gravity Model 31

2.6 Observed Versus Theoretical Propagation Speeds of Baroclinic Waves 33

2.7 Seasonal Variability of Western Boundary Currents 35

2.7.1 The Gulf Stream System 36

2.7.2 The Kuroshio and the East Australian Current 40

2.7.3 The Agulhas Current 41

3 Key Questions and Layout Explained **49**

4 Characteristics of Agulhas Current Seasonality **51**

4.1 Introduction 51

4.2 Key Question 51

4.3 Data and Methods 51

4.3.1 The Agulhas Current Time-series Experiment 51

4.4 Results 58

4.4.1 Seasonal Variability of Velocity Structure 2010-2013 58

4.4.2 Seasonal Variability of Sea Surface Height 65

4.5 Summary and Discussion 67
4.6 Conclusion 68

5 Climatological Indian Ocean Winds **69**
5.1 Introduction 69
5.2 Key Question 69
5.3 Data and Methods 70
5.3.1 QuikSCAT Winds 70
5.3.2 ERA-Interim Winds 70
5.3.3 NCEP-NCAR 70
5.3.4 Calculation of Wind Stress Curl 71
5.3.5 Sverdrup Transport 71
5.3.6 Radon Transform 72
5.4 Results 72
5.4.1 Seasonal Comparison of Wind Products 72
5.4.2 QuikSCAT Wind Stress Variability 77
5.4.3 Rossby Wave Propagation in the Southern Indian Ocean 82
5.5 Summary and Discussion 85
5.6 Conclusion 86

6 Barotropic Adjustment to Indian Ocean winds **87**
6.1 Introduction 87
6.2 Key Question 87
6.3 Data and Methods 87
6.3.1 Barotropic Shallow Water Model 87
6.3.2 Regional Ocean Modelling System - Barotropic Solution 89
6.3.3 Topographic Sverdrup Relation 90
6.3.4 ETOPO2 Bathymetry 91
6.3.5 Climatological Winds 93

6.4 Results . . . 93
6.4.1 Mean circulation of the Barotropic Model . . . 93
6.4.2 Seasonality in the Barotropic Model . . . 94
6.5 Summary and Discussion . . . 97
6.6 Conclusion . . . 98

7 First Baroclinic Mode Adjustment to Indian Ocean Winds 99
7.1 Introduction . . . 99
7.2 Key Question . . . 99
7.3 Data and Methods . . . 100
7.3.1 1 ½ Layer Reduced Gravity Set-up using ROMS Framework . . . 100
7.4 Results . . . 103
7.4.1 Mean Circulation of the 1 ½ Layer Baroclinic Model . . . 103
7.4.2 Initialization with Realistic Pycnocline Depth . . . 104
7.4.3 Influence of Friction on the Seasonal Cycle of the Simulated Agulhas Current . . . 109
7.4.4 Sensitivity of Simulated Seasonal Cycle to Reduced Gravity Parameters 110
7.4.5 Matching Rossby Wave Speeds to Observations . . . 115
7.5 Summary and Discussion . . . 120
7.6 Conclusion . . . 122

8 Sensitivity to Indian Ocean Wind Forcing 123
8.1 Introduction . . . 123
8.2 Key Question . . . 123
8.3 Data and Methods . . . 124
8.3.1 1 ½ Layer Model That Resolves Agulhas Current Seasonality . . . 124
8.4 Results . . . 126
8.4.1 Role of Zonally Varying winds . . . 126
8.4.2 Role of Local Winds . . . 127

8.4.3 Role of Near-Field Wind Stress Forcing . . . 129
8.4.4 Role of Background Circulation . . . 132
8.5 Summary and Discussion . . . 134
8.6 Conclusion . . . 136

9 Summary and Concluding Remarks 137
9.1 Summary of Results . . . 137
9.1.1 How does the Agulhas Current vary seasonally? . . . 137
9.1.2 What is the annual variability of Southern Indian Ocean winds, and what is the nature of the Rossby wave adjustment to this wind forcing? 137
9.1.3 How does a barotropic adjustment to wind forcing contribute to the observed seasonality of the Agulhas Current? . . . 138
9.1.4 How is the seasonality of the Agulhas Current influenced by a first baroclinic mode adjustment to climatological Indian Ocean winds? . . . 139
9.1.5 Which characteristics of Indian Ocean wind forcing predominantly influence the seasonal phasing at the western boundary? . . . 139
9.2 Assumptions, Limitations, and Suggestions for Future Work . . . 140
9.2.1 A Smaller Amplitude of Seasonal Change . . . 140
9.2.2 Other Processes at Play? . . . 141
9.2.3 Climatological QuikSCAT Winds . . . 142
9.2.4 AC Sensitivity to Rossby Wave Propagation Speeds in Realistic Models? 142
9.2.5 Climate Change and Alterations in Stratification . . . 142
9.3 Conclusion . . . 143

10 Acknowledgements 144

11 Supplementary Material 146
11.1 Simplification of 1 ½ Layer Reduced Gravity Model using an Analytical Rossby Wave Simulation . . . 146

12 Appendix **150**

12.1 Supplementary Figures 150

12.2 Derivations 158

12.2.1 Potential Vorticity 158

12.2.2 Sverdrup Balance 159

12.2.3 Topographic Sverdrup Relation 161

13 Bibliography **163**

List of Figures

1.1 Map showing mean SSH of the western boundary region of the Southern Indian Ocean with main circulation features labelled 15
2.1 Map showing main circulation features of the Indian Ocean. From Talley (2011) 18
2.2 Map showing main oceanographic circulation features around Southern Africa. From Ansorge and Lutjeharms (2007) 20
2.3 Map showing the location of ACT array instruments. From Beal et al. (2015) 23
2.4 Downstream evolution of Agulhas Curent transport. From Casal et al. (2009) 24
2.5 Wind stress curl driven Sverdrup transport. From Casal et al. (2009) 27
2.6 Atlas of first baroclinic radius of deformation. From: Chelton et al. (1998) . 33
2.7 Map showing the main western boundary currents of the global ocean. From: Vallis (2017) 36
2.8 Seasonal cycle of Florida Current. From Baringer and Larsen (2001) 38
2.9 Florida Current seasonality for various time periods From Meinen et al. (2010) 40
2.10 Sea surface height anomalies for various sections of the Indian Ocean. From Ffield et al. (1997) 42
2.11 Agulhas Current, Mozambique Channel and East Madagascar Current seasonal cycles simulated using a MOM2 model. From Biastoch et al. (1999) . . 43
2.12 Agulhas Current transport from POCM model. From Matano et al. (2002) . 45
2.13 Agulhas Current seasonal cycle from ACT mooring array. From Beal et al. (2015) 47
2.14 Summary table of reported seasonal cycles of Agulhas Current transport . . 48
4.1 Map of ACT monitoring array. From Beal and Elipot (2016) 52
4.2 ACT 23-year transport proxy 54
4.3 Frequency spectra of 23-year transport time-series 55
4.4 Seasonal cycle of 23-year transport time-series 56
4.5 Seasonal cycle of volume transport for various time periods 57
4.6 Summer versus winter velocity structure of the Agulhas Current 59

4.7 Summer cross sections of Agulhas Current velocity 61
4.8 Composite of summertime SLA maps during ACT mooring experiment . . . 62
4.9 Winter cross sections of Agulhas Current velocity 63
4.10 Composite of wintertime SLA maps during ACT mooring experiment 64
4.11 Summer versus winter sea surface height patterns around ACT 66
5.1 Summer versus winter wind stress curl from different products 74
5.2 Summer versus winter Sverdrup transport from different wind products . . . 75
5.3 Comparison of seasonal cycles of implied Sverdrup transport (Sv) at the ACT line for various wind products 77
5.4 Mean QuikSCAT wind stress over the Southern Indian Ocean 78
5.5 First EOF of QuikSCAT winds stress curl 79
5.6 Wind stress curl at 34.5°S with seasons 81
5.7 Comparison of ACT proxy seasonal cycle with implied Sverdrup transport at the ACT line from QuikSCAT 82
5.8 SLA propagation speeds within the ACT range across the Indian Ocean . . . 84
6.1 Schematic of barotropic shallow water model set-up 89
6.2 Bathymetry of barotropic shallow water model 92
6.3 Map of f/H contours for the Southern Indian Ocean 93
6.4 Mean circulation of the barotropic model 94
6.5 Seasonal anomalies in circulation of the barotropic model 95
6.6 Seasonal cycles of western boundary flows in the barotropic model 96
7.1 Schematic of reduced gravity baroclinic model set-up 101
7.2 Mean circulation of reduced gravity model 104
7.3 Average depth of wind driven layer for reduced gravity model initialized with an active layer depth of 800 m and $g' = 0.0134\ m.s^{-2}$ 106
7.4 Seasonal cycle and hovmöller for reduced gravity simulation initialized with an active layer depth of 800 m and $g' = 0.0134\ m.s^{-2}$ 107
7.5 Effect of friction on the seasonal cycle of the simulated Agulhas Current . . . 110

7.6 Sensitivity of seasonal cycle to reduced gravity parameters 112
7.7 Comparison of theoretical phase speeds and depths of wind driven layer between models of differing g' 114
7.8 Seasonal cycle and hovmöller of reduced gravity simulation initialized with an active layer depth of 800 m and $g' = 0.0076\ m.s^{-2}$ 118
7.9 Seasonal cycle of Tbox during QuikSCAT operational period 120
8.1 Summary of results from reduced gravity model 125
8.2 Seasonal cycle and hovmöller from simulation forced by zonal mean WSC . . 127
8.3 Seasonal cycle and hovmöller from simulation forced by seasonally varying local WSC 128
8.4 Seasonal cycle of AC flow in simulations forced with regional versus remote winds 130
8.5 Seasonal cycle of AC flow in simulations forced with near- versus far-field winds 131
8.6 Seasonal cycle and hovmöller from simulation forced by WSC anomalies only 133
8.7 Seasonal cycle and hovmöller from simulation forced only with WSC anomalies to the west of 35°E 134
11.1 Seasonal cycle from analytical Rossby wave model 148
12.1 Histogram showing number of years in each transport bin for March 150
12.2 Histogram showing number of years in each transport bin for July 150
12.3 Topography across Southern Indian Ocean at 34.5°S 151
12.4 Map showing mean steric height of Pacific-Indian inter-basin gyre. From Ridgway (2007) 151
12.5 WOCE density section across the Southern Indian Ocean 152
12.6 Hovmöller plot showing how the propagation speed of SLA is estimated by eye 153
12.7 Sensitivity of seasonal cycle to reduced gravity parameters with alternative baseline H_o and g' 154
12.8 Seasonal cycle and hovmöller of reduced gravity simulation initialized with an active layer depth of 500 m and $g' = 0.0155\ m.s^{-2}$ 155

12.9 SLA for November for simulation forced with seasonally varying local wind only. 156
12.10SLA for July for simulation forced with seasonally varying local wind only . 157

List of Symbols

Symbol	Parameter description
u, v	zonal and meridional velocities
U, V	zonal and meridional mass transports
w	vertical velocity
x, y, z	cartesian coordinates
ς	relative vorticity
f	planetary vorticity
Ω	earth's rotational rate
β	change in planetary vorticity with latitude
P	pressure
g	gravitational acceleration
g'	reduced gravity
H	thickness of water column/active layer
H_o	initial thickness of active layer
η	sea surface anomaly height
a	anomaly in active layer thickness
τ	wind stress
ρ	sea water density
ρ_o	reference density of sea water
A_h	horizontal friction (viscosity)
λ	Rossby radius of deformation
C	phase speed of a Rossby wave
k, l	zonal and meridional components of the wave number
ω	frequency
n	mode number

List of Acronyms

Acronym	Meaning
AC	Agulhas Current
ACC	Antarctic Circumpolar Current
ACT	Agulhas Current Time-series Experiment
ADCP	Acoustic Doppler Current Profiler
ADCM	Acoustic Doppler Current Meter
ADT	Absolute Dynamic Topography
AVISO	Archiving, Validation and Interpretation of Satellite Oceanographic data
CPIES	Current Pressure Inverted Echo Sounders
CTD	Conductivity-Temperature-Depth sensor
ECMWF	European Centre for Medium- range Weather Forecast
EMC	East Madagascar Current
EOF	Empirical Orthogonal Function
ITF	Indonesian Throughflow
NCEP	National Center for Environmental Prediction
NCAR	National Center for Atmospheric Research
ROMS	Regional Ocean Modelling System
SEC	South Equatorial Current
SLA	Sea Level Anomalies
SSH	Sea Surface Height
Tbox	Boundary layer transport out to 219 km offshore
Tjet	South-westward jet transport
Tx	Transport per unit distance
WOCE	World Ocean Circulation Experiment
WSC	Wind Stress Curl

1 Introduction

The Agulhas Current (AC) is the western boundary flow of the South Indian Ocean subtropical gyre (Beal et al., 2015). It dominates what is thought to be the highest meridional heat flux in the world's oceans (Bryden and Beal, 2001). The current flows along the east coast of South Africa as a narrow, fast flowing and largely stable jet. It is the mechanism whereby warm, saline Indian Ocean water is exported from the Indian Ocean basin and injected into the South Atlantic via a process of ring shedding filaments at the southern tip of Africa (illustrated in Figure 1.1). The current is consequently regarded as an essential limb of the Global Thermohaline Circulation (Beal et al., 2011). At a regional scale the current is thought to play an important role in controlling rainfall and climate over Southern Africa (Njouodo et al., 2018). Furthermore, the current supports a productive local ecosystem as the it is thought to provide a critical mechanism for the dispersal of fish larvae at the early life history stage (Beckley, 1995). The AC is thus thought to play important roles in both ocean circulation and in moderating local and global climate. Despite this, the principal processes that govern the seasonality in volume transport of the current are poorly understood.

Theory suggests that the variability of the AC is related to the large-scale wind stress pattern over the Southern Indian Ocean (Beal et al., 2015). This wind stress variability is communicated across the basin by Rossby waves (Gill, 1982; Killworth, 2001; Subrahmanyam et al., 2001). Theoretically, when there is an alteration in wind stress curl over the Indian Ocean, there is an adjustment of the circulation within the basin, ultimately resulting in a modification in the volume transport of the western boundary current.

This study investigates the seasonality of the AC transport, explores how barotropic and baroclinic processes may contribute to the observed phasing of the seasonal cycle, and examines how the wind stress curl signals are communicated across the Indian Ocean by Rossby waves. The Agulhas Current Time-series (ACT) experiment (Beal et al., 2015) provides a source of *in-situ* data with high spatial and temporal resolution. From the ACT mooring data, a 23-year proxy for AC transport was developed by coupling the *in-situ* current meter measurements with two decades of along-track satellite altimetry (Beal and Elipot, 2016).

This proxy shows that the AC transport is at a maximum in austral summer (February-March) and a minimum in austral winter (July-August). The observed AC seasonality is opposite to the winter-spring maximum predicted by historic model studies (Biastoch et al., 1999; Matano et al., 1999, 2002; Reason et al., 2003). The principal processes that determine the observed seasonal phasing of the AC have, to this date, remained largely unknown.

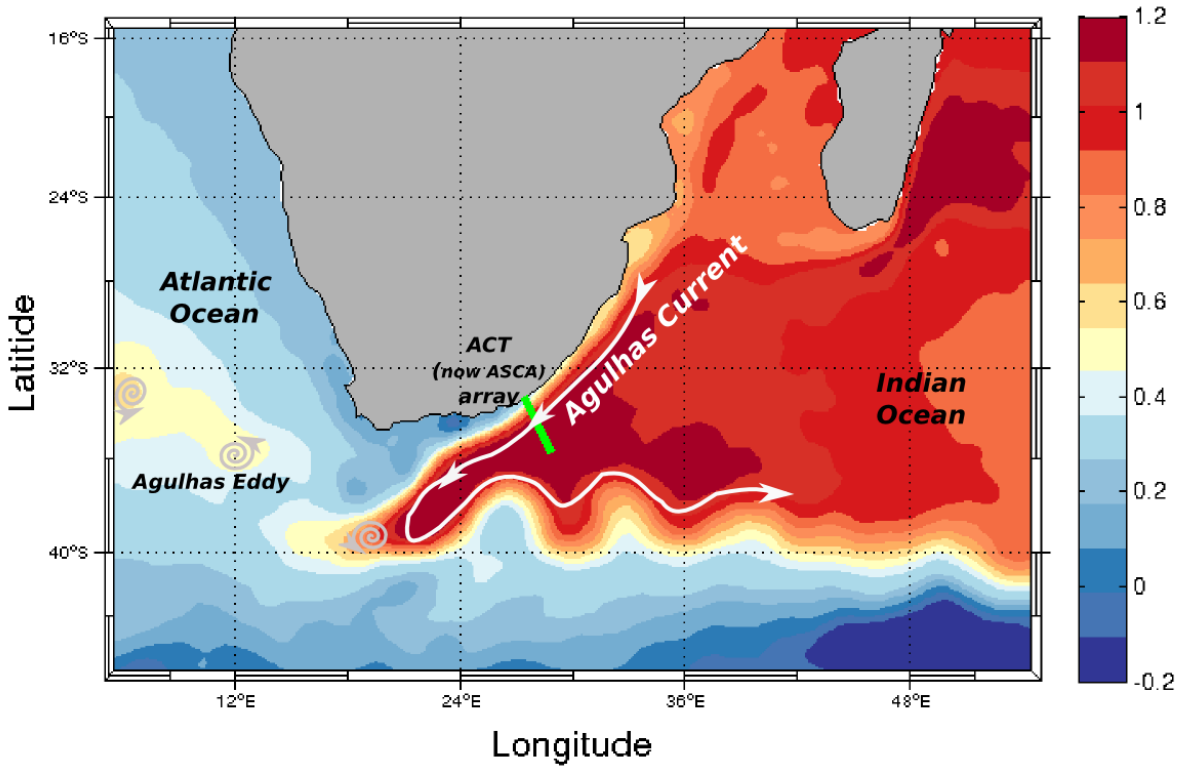

Figure 1.1: *Map showing mean AVISO sea surface height (SSH; dyn meters) of the western boundary region of the Southern Indian Ocean with main circulation features overlaid. Position of the ACT line is shown in green. Leakage of Indian Ocean waters into the South Atlantic in the form of Agulhas rings is illustrated by grey spinning vortexes*

The thesis starts off with a summary of the literature in Chapter 2 and goes on to present the key questions and their motivations in Chapter 3. Chapter 4 reviews the observed seasonal alterations in AC transport, velocity structure and sea surface height patterns. Chapter 5 goes on to examine the accompanying changes in the wind stress curl field, assesses

the relative performance of various wind atlases, and calculates the observed propagation speeds of sea level anomalies across the Southern Indian Ocean. These first two results chapters provide context for the analysis of the shallow water model results presented in Chapters 6 to 8. The extent that a barotropic adjustment to climatological winds contributes to the observed AC seasonality is discussed in Chapter 6 using a single layer idealized model. The model complexity is increased in Chapter 7 where a reduced gravity model is used to investigate how the seasonal phasing of the AC is influenced by a first baroclinic mode adjustment to climatological winds. The reduced gravity model provides a useful platform from which the influence of winds over different portions of the Southern Indian Ocean is investigated in Chapter 8. The aim of using the shallow water models is not to simulate the details of the system, but rather to preserve the essential components using an idealized set-up, thereby providing an analogy of the natural system and insight into the dynamics of the observed changes. The study is concluded with a discussion where the results are summarised along with their assumptions and limitations, and suggestions for future work are proposed (Chapter 9). This study is the first to use *in-situ* observations, satellite measurements, and idealized ocean models to obtain a better understanding of the drivers of the AC seasonality.

2 Literature Review

2.1 The Indian Ocean

The Indian Ocean plays a vital role in the Global Thermohaline Circulation and climate regulation (Gordon, 1985). It provides a link between the Pacific and Atlantic Oceans and is a source of warm water for the upper limb of the global ocean conveyor belt (Gordon, 1985). Like most ocean basins, the Indian Ocean possesses modes of variability from sub-seasonal to inter-annual. Most of these modes are in some way connected to the seasonal cycle (Schott et al., 2009). Improving knowledge regarding the seasonal variability of the various systems within the Indian Ocean is essential when attempting to understand the role that this ocean basin plays in influencing local and global climate. The Indian Ocean differs from other ocean basins in a number of ways. The two most striking differences are that it is confined in the north by the Asian land mass and that it receives an additional input of water at low latitudes via the Indonesian Throughflow (Talley, 2011). The circulation of the Indian Ocean can be divided up into two major systems: the seasonal monsoon gyre in the north, and the Southern Hemisphere subtropical gyre at mid-latitudes. The surface circulation of the Indian Ocean is illustrated in Figure 2.1 where these distinct circulation systems can be seen. This study will focus on the southern portion of Indian Ocean, hereafter termed the Southern Indian Ocean. This domain consists of the Indian Ocean subtropical gyre, bounded in the north by the South Equatorial Current (SEC) and in the south by the Antarctic Circumpolar Current (ACC), and excludes the cyclonic equatorial gyre.

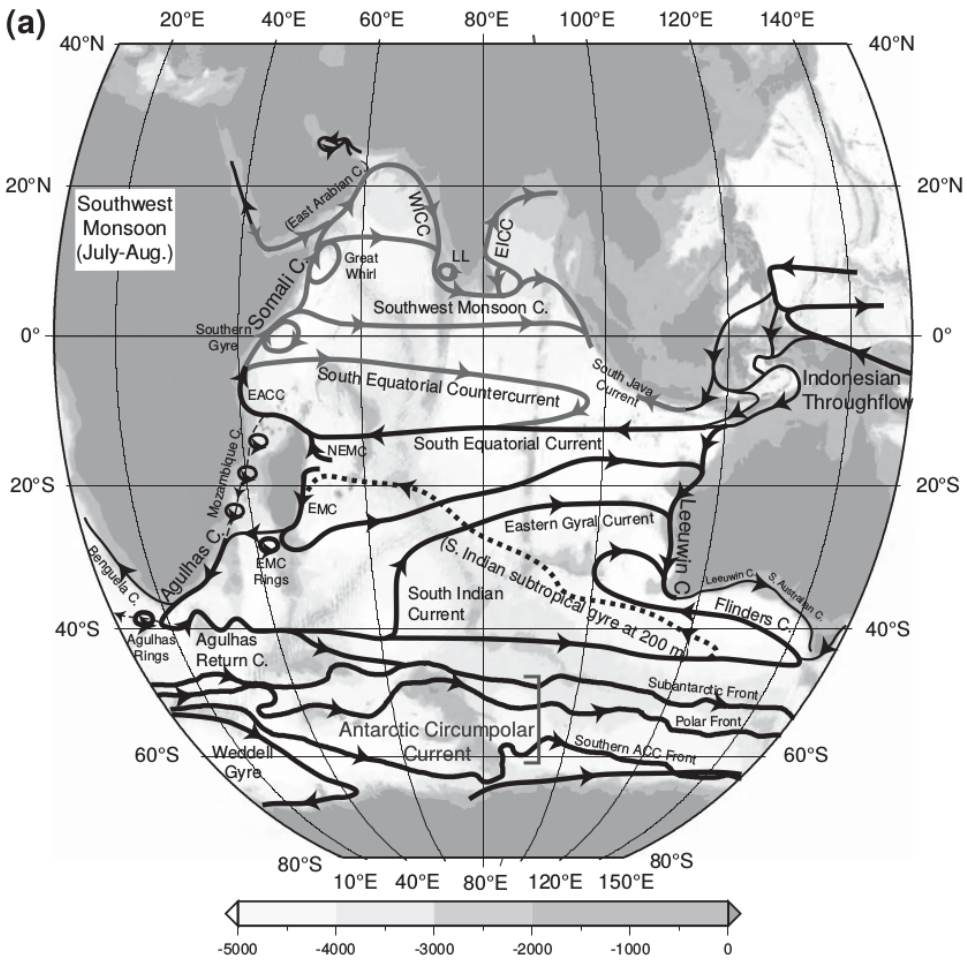

Figure 2.1: *Schematic showing main features of Indian Ocean circulation. Grey lines indicate seasonally reversing monsoonal currents in the Northern Indian Ocean. Black lines show mean flows with no seasonal reversals. Grey shading shows location of land masses and shallow topographic features with degree of shading indicating depth below sea level (m). From Talley (2011)*

One of the first studies to investigate the annual strengthening and weakening of the Southern Indian Ocean gyre was conducted by Ffield et al. (1997) using satellite and *in-situ* hydrographical data. The gyre circulation was found to strengthen in March and September (when the sun crosses the equator) and weaken in June and December (when the sun is furthest from the equator). The circulation pattern is strongly influenced by the westerly

wind field south of 30°S and by the meridional movement of the Inter-Tropical Convergence Zone (ITCZ) with the seasons (Ffield et al., 1997). These shifts in the strength and position of the winds change the wind stress curl (WSC), and therefore can force basin-wide changes in the magnitude and pattern of ocean circulation (Baquero-Bernal and Latif, 2005). The seasonal variations of flows throughout the basin, however, do not directly correlate with the months of strengthening and weakening of the subtropical gyre. The wind stress curl variability is principally communicated by Rossby waves which, at mid-latitudes, take years to travel westwards across the basin. These waves facilitate a cross-basin transfer of energy and provide a mechanism whereby ocean circulation can adjust to wind stress forcing. The arrival of these waves at the western boundary is thought to affect the East Madagascar Current, the flow through the Mozambique Channel and the Agulhas Current (AC) (Schouten et al., 2002; Zhai et al., 2010; Braby et al., 2016), as well as influencing features such as the Seychelles - Chagos thermocline ridge (Hermes and Reason, 2009).

2.2 The Agulhas Current

The AC is the western boundary jet of the Southern Indian Ocean. It is responsible for the poleward transport of water along the east coast of southern Africa and is the strongest western boundary current at 30° latitude (Bryden et al., 2005). A schematic of the current is shown in Figure 2.2 where the position of the current in relation to the Southern African land mass and the surrounding oceanographic features can be seen. The AC and its leakage provide a critical link between the Indian and Atlantic Oceans, thereby playing a key role in global ocean circulation and climate regulation (Gordon, 1985; Lutjeharms, 2006; Beal et al., 2011). The current also exerts a climatic influence on the African subcontinent, as it provides a source of latent heat for onshore weather systems, thereby influencing local rainfall (Reason, 2001). Furthermore, it is of socio-economic importance as it sustains lucrative local fisheries (Lutjeharms and De Ruijter, 1996).

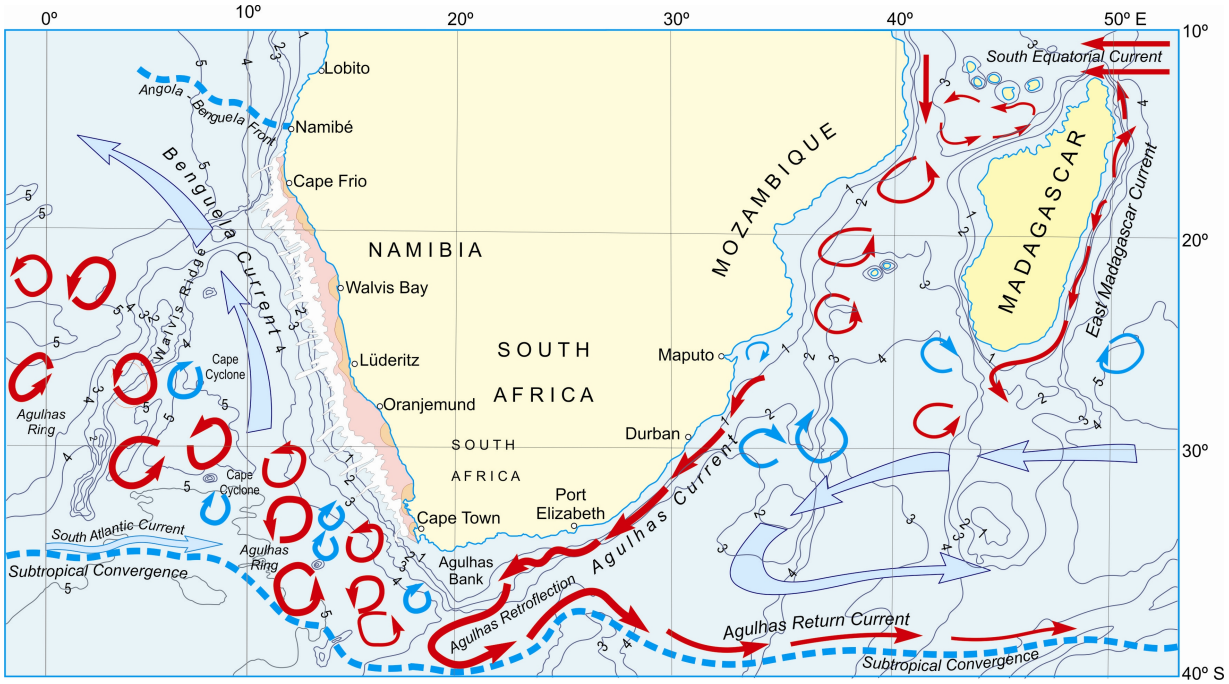

Figure 2.2: *Diagram showing the main oceanographic circulation features around Southern Africa with relatively warmer currents marked in red, and colder features, along with the division between warm and cold areas, shown in blue. Background shading indicates depth of bathymetry in thousands of meters. The principal currents are labelled in black along with the countries and main cities of Southern Africa, so as to provide insight into the relative positions of the ocean circulation features. From Ansorge and Lutjeharms (2007)*

The current flows along the East Coast of South Africa from approximately 27°S to 40°S (see Figure 2.2), carrying water sourced from Mozambique Channel eddies, the East Madagascar Current, and re-circulated water from the Southern Indian Ocean sub-gyre (Gordon, 1985; Stramma and Lutjeharms, 1997; de Ruijter et al., 2002). When the AC jet reaches the tip of the African continental shelf it separates from the topographic boundary and continues south-westwards as a free jet until about 20°E where it then loops back on itself and travels eastwards as the Agulhas Return Current (Matano et al., 1999; Schouten et al., 2000). This loop is known as the Agulhas Retroflection and is thought to arise due to the inertia of the current and the shape of the Southern African land mass (Ou and De

Ruijter, 1986; Chassignet and Boudra, 1988). During this retroflection, pockets of warm and salty Indian Ocean water, known as Agulhas Rings, are periodically shed into the South Atlantic (van Leeuwen et al., 2000).

The dominant mode of variability of the AC is associated with the passing of a meander event known as a Natal Pulse (Lutjeharms and Van Ballegooyen, 1988; van Leeuwen et al., 2000; Backeberg et al., 2008). These are solitary meanders that originate through the interaction of eddies with the AC, typically near the Natal Bight, and travel downstream covering between 10 and 20 kilometres a day. The passing of these features shift the core of the current further away from the coast, inducing a cyclonic circulation inshore and an anticyclonic circulation offshore, with a strong positive transfer of kinetic energy from the mean flow to the meander through non-linear interactions (de Ruijter et al., 1999; Elipot and Beal, 2015). Leber and Beal (2015) and Elipot and Beal (2015) showed that a Natal Pulse event does not change the volume transport of the AC, as the weakening of the core is accompanied by a compensating broadening of the width of the current.

Up until recently, there has been a deficiency of *in-situ* time-series data on the AC, and so studies focusing on the variability of this current have largely relied on ocean models or satellite data. The Agulhas System is, however, highly complex and has proven to be challenging to model adequately, partly due to the elevated levels of turbulence (Backeberg et al., 2008). The first extensive set of *in-situ* hydrographic data was obtained during the Agulhas Undercurrent Experiment, undertaken from March 2003 to August 2004 (Beal, 2009; Casal et al., 2009). This experiment consisted of four hydrographic transects of the current with the sections connected offshore to provide three closed boxes (positions of which can be seen in Figure 2.5). Results suggested that there was no inertial recirculation of the AC between 30°S and 36°S (Casal et al., 2009). Using data from the Agulhas Undercurrent Experiment, Casal et al. (2009) defined baroclinic transport as the integrated transport from the surface to a level of no motion (approximately the upper 1500 m), and the remainder of the flow as the barotropic transport. Casal et al. (2009) investigated the possible presence of an inertial recirculation by examining the changes in barotropic transport between each

sampling line, following the dynamics based method of Johns et al. (1995). No downstream increase in barotropic transport was found, and thus it was concluded that there was no evidence for recirculation.

The Agulhas Current Time-series (ACT) experiment produced the longest and most extensive set of *in-situ* velocity measurements of the AC to date. These measurements span the period from April 2010 to February 2013, providing 34 months of high resolution velocity and transport measurements (Beal et al., 2015). The array left the South African coastline at 33.4°S and stretched out to sea along the path of a satellite altimeter groundtrack - at an angle of 15° south of perpendicular with the continental slope (see Figure 2.3)(Beal et al., 2015). The array consisted of 7 full-depth current meter moorings and 4 current pressure inverted echo sounders (CPIES)(positions marked in Figure 2.3).

The full cross-current coverage of the ACT experiment allows for the estimation of both a 'jet' transport and a 'box' transport (Beal et al., 2015). The jet transport (Tjet) depends on the strength and cross-sectional area of the current at each time step. It excludes the counter flows on the flanks of the jet and therefore only measures the south-westward transport. The box transport (Tbox), on the other hand, is the net transport from the coast out to a fixed distance of 219 km offshore (mean position of the zero velocity isotach)(Beal et al., 2015). This estimate is the boundary layer transport and can include counter flows in surrounding waters in the transport estimate. The mean and standard error of the mean of the AC Tbox and Tjet transports calculated from the ACT mooring array time-series were found to be -84 $\pm$ 2 Sv and -77 $\pm$ 5 Sv respectively (Beal et al., 2015).

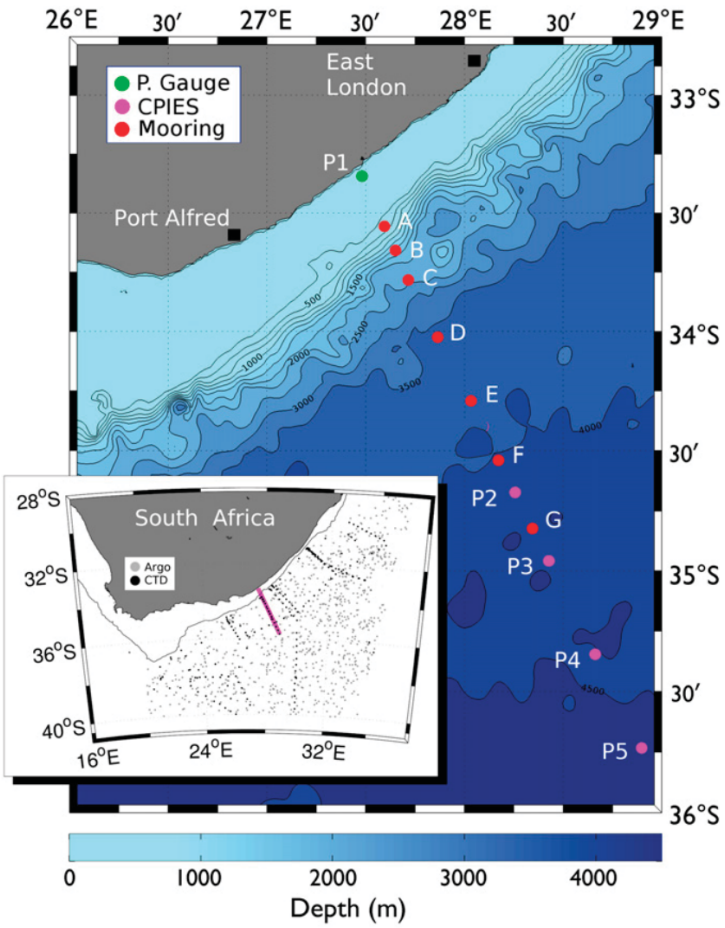

Figure 2.3: *Geographical location of the Agulhas Current Time-series (ACT) mooring array. Location of current meter moorings are shown as red dots and labelled A-G, CPIES positions are shown by magenta dots and labelled P2-P5). Background shading and associated contours show depth of bathymetry. The smaller map inset in the figure shows the ACT line (magenta) in context of the greater Southern Africa coastline. From Beal et al. (2015)*

The Tbox estimate, based on the traditional method of transport calculations, is 10 Sv greater than that calculated at the World Ocean Circulation Experiment (WOCE) line at 32°S. This increase is equal to that predicted by the Sverdrup Balance due to an increase in wind driven transport with a southward increase in WSC (Beal et al., 2015). However, the AC transport cannot be entirely accounted for by calculating the interior Sverdrup WSC driven flow. The ITF and the Indian Ocean overturning must also be included, contributing

less than a third to the total volume transport of the AC (Casal et al., 2009). The majority of the flow is driven by the Sverdrup transport in the interior. This is illustrated in Figure 2.4 by the difference in magnitude between the blue line showing Sverdrup transport and its southward increase and the pink line showing the sum of all three contributions.

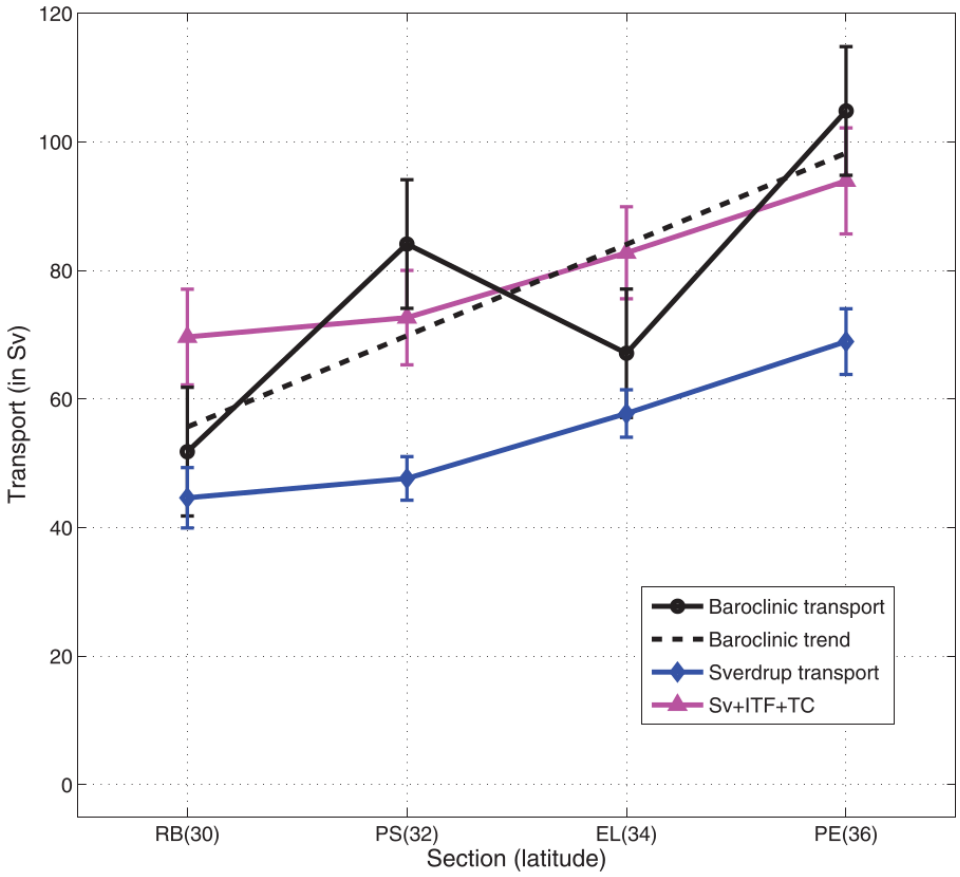

Figure 2.4: *Downstream evolution of various transport estimates obtained during the Agulhas Undercurrent Experiment. The x-axis marks the latitude of four coastal towns which coincide with the position of the four offshore hydrographic sections of the survey, Richards Bay (RB), Port Shepstone (PS), East London (EL) and Port Elisabeth (PE). The magenta line shows the concatenated transport from the Sverdrup driven interior flow (Sv), the Indonesian Throughflow (ITF), and the Thermohaline Circulation (TC). From Casal et al. (2009)*

2.3 Sverdrup Dynamics

Wind is the dominant source of kinetic energy to the world's oceans (Ferrari and Wunsch, 2008). The transfer of momentum from the atmosphere to the ocean determines the pattern and magnitude of large-scale circulation (Gill, 1982). In 1947 Harald Ulrich Sverdrup combined the geostrophic and Ekman theories to describe the ocean's response to wind stress forcing, called the Sverdrup Relation:

$$V = \frac{1}{\beta} \nabla \times \tau \tag{1}$$

Where V is the vertically integrated meridional transport ($V = \rho H v$), H is the water column height, ρ represents the mean density of the water column, τ is the wind stress, and v is the mean meridional velocity of the water. From Equation 1, β is the gradient of Earth's planetary vorticity:

$$\beta = \frac{\partial f}{\partial y} \tag{2}$$

The Sverdrup Relation (see Appendix for full derivation) states that the magnitude of the depth integrated meridional transport is proportional to the WSC. Sverdrup's theory can be used to explain how the responds to turbulent stresses acting on the mixed layer. Wind driven convergence or divergence within the upper ocean force Ekman pumping or suction at the base of the mixed layer. This, in turn, results in either a squashing or stretching of the water column below. Potential Vorticity (PV), given by Equation 3, must always be conserved within the Sverdrup framework:

$$\frac{D}{Dt}\left(\frac{f + \delta}{H}\right) = 0 \tag{3}$$

This equation states that the change in absolute vorticity ($f + \delta$), over water column height (H), is zero over time. If the water column is stretched or squashed, H is increased or decreased. In order to maintain a constant PV, the whole water column must consequently shift to a position of higher or lower planetary vorticity (Sverdrup, 1947; Pedlosky, 1987).

The water parcel could alternatively change its relative vorticity (δ), but if this process is happening on a large scale, the entire basin would need to spin up, and so PV is conserved through a change in the planetary vorticity. In this way, an entire water column is set into motion due to WSC forcing at the surface. This is known as the 'Sverdrup Balance' and it has proven to be a very powerful tool for oceanographers, as it is possible to determine meridional transport using information regarding the magnitude of local WSC alone. No measurement of vertical density profiles, or the distribution of velocity with depth, is needed. The limitation is that this theory is only useful to describe large scale steady flows on the assumption that the Ekman layer experiences no friction and that the ocean has a flat bottom (i.e. no topography). In reality ocean movement is more complicated. These assumptions are, however, valid when attempting to describe the mean state of large-scale circulation (Sverdrup, 1947; Pedlosky, 1987).

Let us take the Southern Indian Ocean basin as our example to examine the application of Sverdrup theory. Positive WSC is set up by the Easterly Trade Winds at low latitudes and the Southern Hemisphere Westerlies at high latitudes. Positive WSC drives a convergence of fluid within the Ekman layer and forces a downward Ekman pumping out of the Ekman layer, resulting in a squashing of the water column below. To conserve PV (Equation 3), the water column must move to a position of lower planetary vorticity (move towards the equator). Figure 2.5 from Casal et al. (2009) shows the mean Sverdrup transport in the Indian Ocean calculated from IFREMER monthly WSC from 1999 to 2006. The magnitude of Sverdup transport increases westward across the basin (Figure 2.5). This is due to the fact that the transport is proportional to the integral of the WSC, and therefore the further west the calculation is computed, the larger the area of wind forcing to be integrated.

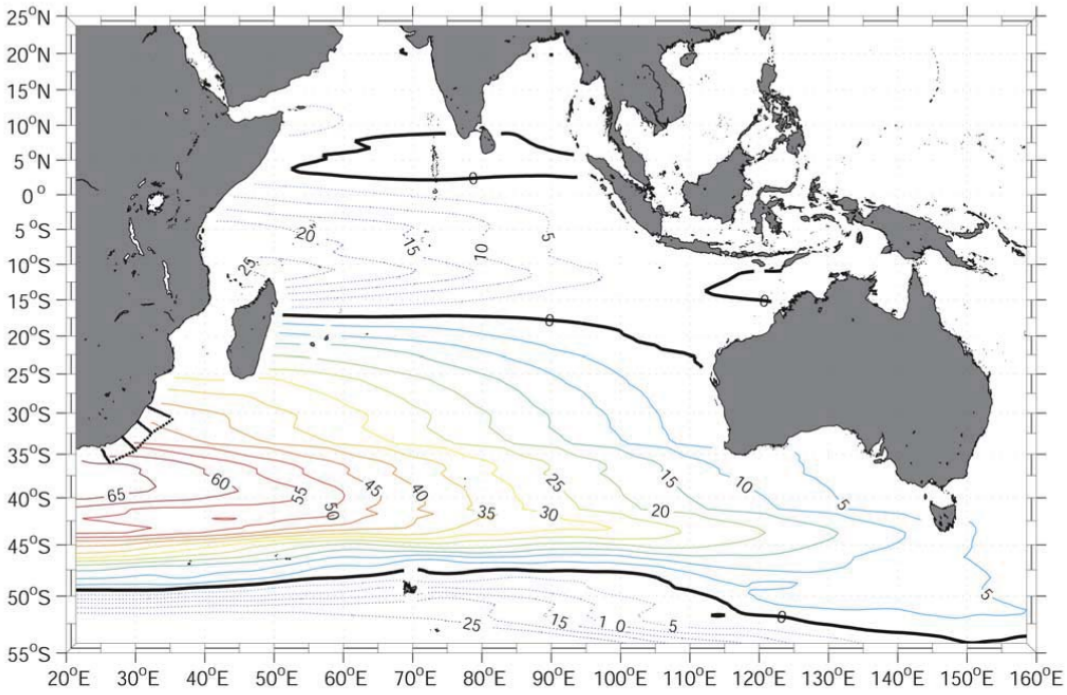

Figure 2.5: *Sverdrup transport (Sv) calculated using IFREMER monthly wind stress curl for the period 1999-2006. The positions of the hydrographic sections undertaken as part of the Agulhas Undercurrent Experiment are shown in black along the east coast of South Africa. From Casal et al. (2009)*

To conserve mass, the equatorward meridional transport in the centre of the Southern Indian Ocean basin must be compensated by a flow of equal magnitude, but opposite in direction, located at the western boundary (Stommel, 1948). This flow is the poleward flowing AC which acts to remove the vorticity imparted by the positive WSC onto the subtropical Indian Ocean gyre. The Sverdrup equation is therefore only valid up until the western boundary layer, as in this area the approximations appropriate for the mid-ocean, such as a uniform depth of no motion, are no longer valid. This pattern of circulation is not unique to the Indian Ocean, in fact, all 5 major ocean basins experience an equatorward Sverdrup transport in the interior of the basin compensated by a poleward western boundary current (Stommel, 1948; Gill, 1982). The mean volume transport of each western boundary current can therefore be approximated using the Sverdrup Relation by measuring the mean

WSC across the basin at the latitude of the current. The actual volume transport of a western boundary current may in reality be much larger, as the thermohaline component must be included, along with the possible presence of re-circulations (Imawaki et al., 2013).

2.4 Rossby Planetary Waves

Beyond the time-mean Sverdrup circulation, the ocean responds to wind forcing through adjustment achieved by Rossby waves (Anderson and Corry, 1985; Siedler et al., 2001). Rossby waves are ubiquitous features of the ocean and interact strongly with the general circulation. These waves provide the mechanism responsible for the westward intensification of ocean gyres and therefore play a critical role in the dynamics of western boundary currents (Chelton and Schlax, 1996; Killworth et al., 1997; Fyfe and Saenko, 2007). They are the main mechanism whereby energy is transferred across ocean basins (Subrahmanyam et al., 2001). Rossby waves are created by the need to conserve potential vorticity in response to changes in the ocean's vertical structure. Various processes can give rise to the creation of a Rossby wave, ranging from variations in WSC to topographical features and buoyancy forcing (Gill, 1982; Chelton and Schlax, 1996).

Rossby waves can be divided up into 'barotropic' and 'baroclinic' waves, with the corresponding wave number delineating the degree of stratification. Barotropic waves are insensitive to stratification and can therefore be thought of as propagating in a homogeneous fluid. Barotrotropic waves have a vertical wave number of 0, and are thus known as the 'zeroth mode'. These waves propagate through the ocean at high speeds, crossing an ocean basin in a number of weeks (Cipollini et al., 2010). Baroclinic waves can have vertical modes from one to infinity, determined by the degree of stratification, and travel much slower than the barotropic waves, taking years to cross an ocean basin (Gill, 1982; Killworth, 2001). The first baroclinic mode applies to an ocean consisting of two layers separated by the 'main' thermocline or pycnocline. The barotropic mode and first baroclinic modes together communicate the majority of the WSC signal (Anderson and Corry, 1985).

Detecting the presence of a Rossby wave from sea surface height (SSH) data is challenging

as they have a small SSH signature and can have wavelengths of hundreds to thousands of kilometers long (Chelton and Schlax, 1996). Barotropic waves travel too fast to be observed by satellite. First baroclinic mode waves, on the other hand, travel westwards at similar speeds to large scale ocean eddies and so their phase speed can be estimated by observing sea level anomalies from altimeter data (Chelton et al., 2007).

Rossby waves arise due to the fact that planetary vorticity is a function of latitude (Gill, 1982):

$$f = 2\Omega sin\Theta \tag{4}$$

Where f is the coriolis parameter, Ω is the rotation rate of the Earth ($7.29 \times 10^{-5} rad.s^{-1}$) and Θ is the latitude. The horizontal restoring force of this Rossby wave is the change in the vertical component of the angular rotation vector of the Earth, known as the Beta effect (Sverdrup, 1947; Pedlosky, 1987) (Equation 2). The dispersion relation for barotropic Rossby waves (a single homogeneous layer) is:

$$\omega_0 = -\frac{\beta k}{k^2 + l^2 + \frac{f^2}{C_0^2}} \tag{5}$$

where k and l are the zonal and meridional components of the wave number , and w_n is the frequency for mode n. C_0 is the gravity wave phase speed of barotropic waves which is denoted as:

$$C_0 = \sqrt{gH} \tag{6}$$

Barotropic waves travel fast, providing a rapid adjustment to surface forcing. C_0 is therefore very large and $\frac{f^2}{C_0^2}$ in Equation 5 is usually negligible in the denominator.

The dispersion relation is equally applicable to stratified flows, where C_0 is replaced by C_n, the gravity wave phase speed of baroclinic waves, where $C_n = \sqrt{g'H}$, g' is the reduced gravity parameter and n is any number from 1 to infinity.

The dispersion relation for baroclinic waves is:

$$\omega_n = -\frac{\beta k}{k^2 + l^2 + \frac{1}{\lambda_n^2}} \tag{7}$$

Where λ_n is the Rossby radius of deformation for each mode n. λ_n depends on the baroclinic gravity wave phase speed by:

$$\lambda_n = \frac{C_n}{|f|} \tag{8}$$

Equation 7 can be used to calculate the Rossby wave phase speed, Cr_n. As the zonal component of flow is much greater than the meridional components, the zonal component of the Rossby wave phase speed can be approximated to:

$$Cr_{xn} = \frac{\omega_n}{k} = -\frac{\beta}{k^2 + l^2 + \frac{1}{\lambda_n^2}} \tag{9}$$

This indicates that for every positive wave number, there is only one solution, and it is always negative, thereby implying that the baroclinic Rossby wave phase speed will always be westward. The approximation of the meridional (north-south) component of movement being much smaller than the zonal (east-west) component is especially true for long wavelength baroclinic Rossby waves, as the waves move almost entirely in a westward direction. This allows for the longwave approximation to be made, where the group and phase speeds are equal, and $\lambda_n k \ll 1$, meaning the waves are non-dispersive. For this case the baroclinic Rossby wave phase speed becomes:

$$Cr_{xn} = Cr_{gn} = -\beta\lambda_n^2 \tag{10}$$

During their journey westwards, baroclinic waves can be reinforced or dampened through interactions with various processes or features such as a change in structure of the thermocline, the presence of a topographic barrier, or constructive or destructive interference with a localized wind forcing (Wang et al., 2001; Hermes and Reason, 2008). Once these waves and eddies reach the western boundary of an ocean basin, their energy can instigate coastal-trapped waves or can be scattered to higher wave number modes thereby facilitating

diapycnal mixing (Zhai et al., 2010). This process removes the energy imparted to the ocean by wind forcing and maintains the balance of energy in the system.

2.5 The Reduced Gravity Model

Baroclinic Rossby waves transmit WSC forcing signals in a stratified ocean. These waves provide a critical, coherent mechanism whereby WSC variations over the entire basin are communicated to the western boundary. The first baroclinic mode applies to an ocean consisting of two layers separated by the 'main' pycnocline.

A simple model of the first baroclinic mode, known as the reduced gravity model, is a two layer system with the upper layer active and the lower layer at rest (Pond and Pickard, 2013). The upper layer has a constant density ρ_1, and the lower layer a constant density of ρ_2. The pressure gradient in the upper layer is governed by anomalies in SSH (η_1) and so is given as:

$$P_1 = \rho_1 g \nabla \eta_1 \tag{11}$$

The total first layer depth is defined as $H = H_0 + \eta_1 - \eta_2$, where H_0 is the initial depth of the upper layer, η_1 is the anomaly in SSH and η_2 is the anomaly in the depth of the pycnocline (base of upper layer), where both η_1 and η_2 are smaller in magnitude than H. There is no pressure gradient in the lower layer as it is stationary. Changes in sea surface height are thus directly reflected in a change in pycnocline depth (Pond and Pickard, 2013):

$$\nabla \eta_1 = \frac{\rho_1 - \rho_2}{\rho_1} \nabla \eta_2 \tag{12}$$

and the pressure gradient in the first layer can be expressed as:

$$\nabla P_1 = \frac{\rho_1(\rho_2 - \rho_1)}{\rho_2} g \nabla H \tag{13}$$

Where ρ_o represents the mean density of the water column. Reduced gravity, g', is thus defined as a function of the pressure differences:

$$g' = \frac{(\rho_2 - \rho_1)}{\rho_2} g \tag{14}$$

For this simplified reduced gravity setup, the radius of deformation is now given as:

$$\lambda_1 = \frac{\sqrt{g'H}}{f} \tag{15}$$

By Equation 10, the phase speed of first baroclinic mode Rossby waves is:

$$Cr_1 = -\beta\lambda_1^2 \tag{16}$$

This phase speed describes the propagation of a Rossby wave in a scenario of zero background flow. Chelton et al. (1998) compiled a global map of values for the first baroclinic radius of deformation using climatological average temperature and salinity profiles (shown in Figure 2.6). As is evident from this map, the radius of deformation increases towards the equator as the value of planetary vorticity decreases (see Equation 15). First baroclinic Rossby waves have long wavelengths and fast propagation speeds in the tropics and shorter wavelengths with slow propagation speeds in the subtropics and higher latitudes.

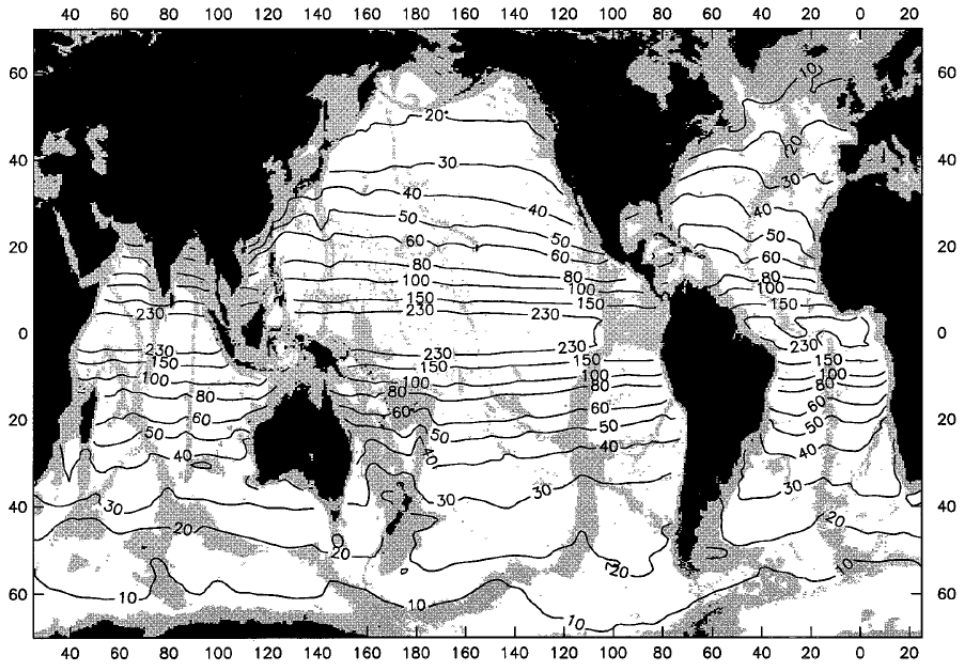

Figure 2.6: *Global map showing the first baroclinic radius of deformation in kilometres at a 1° by 1° resolution. Areas shallower than 3500m are shaded in grey. From: Chelton et al. (1998)*

2.6 Observed Versus Theoretical Propagation Speeds of Baroclinic Waves

Many studies have investigated the properties and dynamics of baroclinic Rossby waves using models and satellite data and have reported that these waves travel faster in reality than that predicted by classical theory (Chelton et al., 1998; Qiu et al., 1997; Meyers, 1979; Capotondi and Alexander, 2001; DiNezio et al., 2009; Czeschel et al., 2012). This indicates that the ocean itself responds to WSC changes more rapidly than is theoretically projected. Chelton and Schlax (1996) used three years of satellite altimetry data to observe Rossby wave propagation across the world's oceans and showed significant deviation in propagation speeds of the observed waves compared to that predicted using standard theory. Accordingly, the equations describing the properties of Rossby waves were considered "incomplete" in their

description of the phenomenon (Subrahmanyam et al., 2001). This is not surprising as the theory is only appropriate for an ocean basin of uniform depth where there is zero background flow (Killworth et al., 1997). The phase speeds of Rossby waves are generally of the same order of magnitude as the background circulation. The assumption of Equation 15 - that the background ocean is at rest - is therefore a poor assumption. The gradient in potential vorticity set up by the background circulation is likely responsible for the disagreement between observations and linear theory (Killworth et al., 1997). Rossby wave propagation speeds between 10°N to 10°S were found to be 1-1.5 times faster than theoretical values, and poleward of this waves were found to be up to 2 times faster than predicted (White, 1977; Chelton and Schlax, 1996; Killworth et al., 1997; Qiu et al., 1997). Phase speeds in the tropics tend to be closer to what is expected due to the dominance of boundary generated Rossby waves which travel at predicted wave speeds and dominate the SSH anomalies (Qiu et al., 1997). Further from the equator, the influence of waves originating at the boundary is weaker as these waves tend to dissipate rapidly due to both eddy dissipation and the vertical propagation of energy into the ocean below the thermocline (Chelton and Schlax, 1996; Qiu et al., 1997; Cummins et al., 1986). The majority of the SSH variability in the mid-latitudes is, therefore, generated in the interior by the overlying WSC (Fu and Qiu, 2002).

Fyfe and Saenko (2007) investigated how the dynamics of Rossby waves may change in response to upper-ocean warming and the consequent alteration in stratification. They used climate model simulations of the North Pacific to show that anthropogenic warming of the upper ocean resulted in an increase in propagation speed of baroclinic Rossby waves. This was explained by an increase in the density gradient between the upper and lower layers of the ocean. Evidence suggests that the Indian Ocean has been warming over the past 50 years (Roxy et al., 2014). It has been estimated that since 1950, the Indian Ocean warmed by over 1°C at the surface (larger than the global average of 0.6°), possibly due to a faster response to climate change (Lau and Weng, 1999; Alory et al., 2007; Roxy et al., 2014). The effect that this warming has had on Rossby wave phase speeds in the Indian Ocean has yet to be examined. However, model simulations based on emission scenarios proposed by the

Intergovernmental Panel on Climate Change (IPCC) reported a 35% speed up in Rossby waves by the end of the 21st century (Fyfe and Saenko, 2007). This hypothetical increase in phase speed would imply a decrease in adjustment time of an ocean basin, which could mean a change in the seasonal cycle of the western boundary current as the system would respond more rapidly to WSC fluctuations.

2.7 Seasonal Variability of Western Boundary Currents

Western boundary currents provide the main pathway for water to flow away from the equator and towards the poles, balancing the thermohaline and wind forcing of the interior (Hogg and Johns, 1995). Observations have indicated that the Sverdrup Balance does not hold on seasonal time-scales as the seasonal cycle of volume transport at the western boundary is often weaker than that of the Sverdrup transport and out of phase (Anderson and Corry, 1985; Czeschel et al., 2012; Beal and Elipot, 2016). The Sverdrup Balance is therefore appropriate in describing the mean state, but cannot be used to explain the seasonal variations (Anderson and Corry, 1985; Matano et al., 2002).

There have been opposing theories and a considerable amount of confusion regarding what mechanisms govern the seasonal variability of western boundary currents (Gill and Niller, 1973; Anderson and Corry, 1985; Matano et al., 1999; Czeschel et al., 2012; Domingues et al., 2016). Gill and Niller (1973) and Anderson and Corry (1985) both argued that waves responsible for the adjustment of the ocean to WSC fluctuations are either too sensitive to topography (barotropic) or too slow (baroclinic) to effectively communicate the seasonal variability in wind stress to the western boundary. This section will review the existing literature addressing the seasonal variability of the main western boundary flows, namely the Gulf Stream System, the Kuroshio, the East Australian Current, and the Agulhas Current (locations can be seen in Figure 2.7).

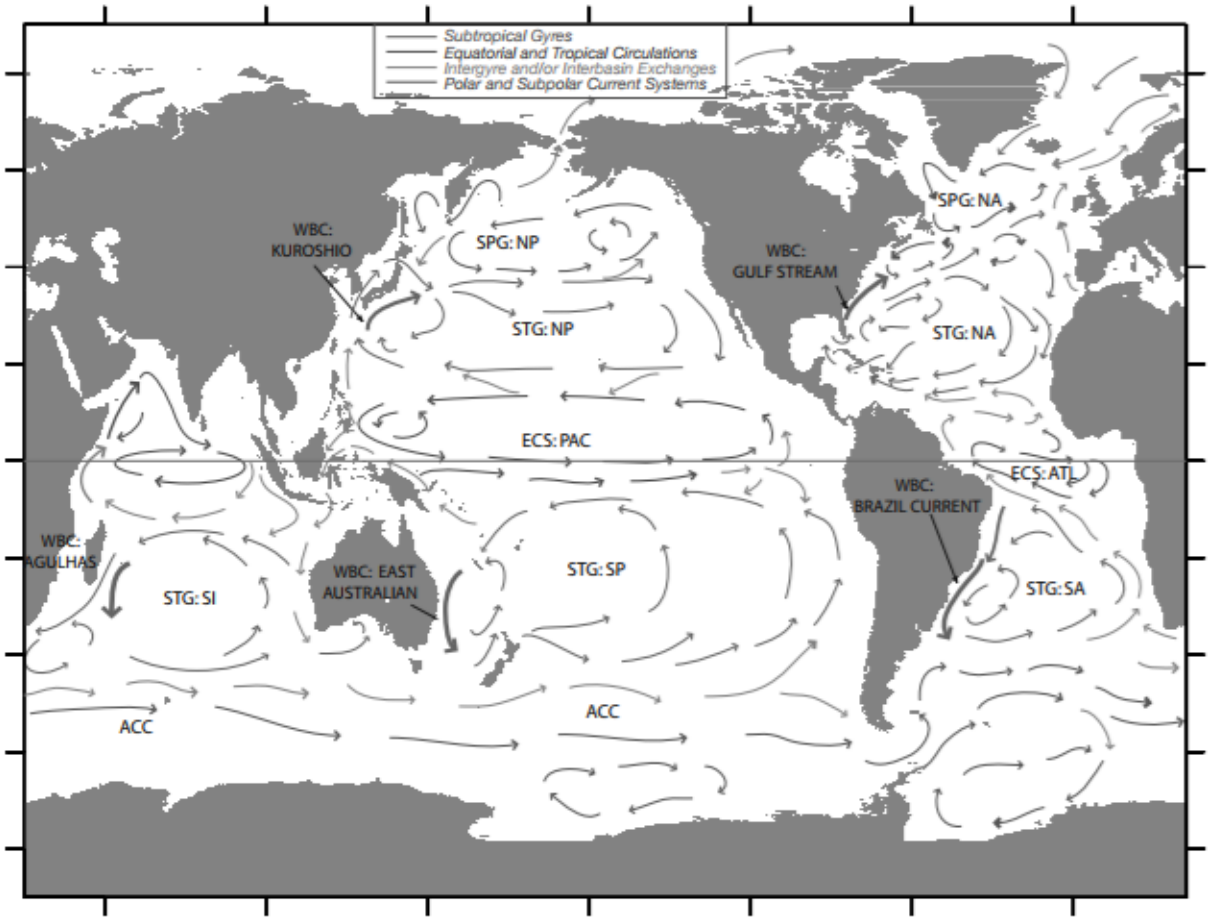

Figure 2.7: *A schematic representation of the main circulation features of the global ocean. Key: STG: Subtropical Gyre, SPG:Subpolar Gyre, WBC: Western Boundary Current, ECS: Equatorial Current System, NA: North Atlantic, SA: South Atlantic, NP: North Pacific, SP: South Pacific, SI: South Indian, ACC: Antarctic Circumpolar Current, ATL: Atlantic, PAC: Pacific. From: Vallis (2017)*

2.7.1 The Gulf Stream System

The western boundary currents of the North Atlantic are collectively known as the Gulf Stream System (see location in Figure 2.7). The Gulf Stream System carries both the wind-driven circulation and the upper limb of the thermohaline circulation northwards (Baringer and Larsen, 2001; Atkinson et al., 2010). The first segment is known as the Florida Current

(FC) as it originates where the Gulf of Mexico's loop current enters the Florida Straits. The FC flows northwards along the east coast of North America between Florida and the Bahamas. Upon exiting the Florida Straits, this flow becomes the Gulf Stream for the duration of its path along the east coast of North America until it reaches the shelf break at the latitude of Cape Hatteras. Thereafter this free flowing jet is known as the Gulf Stream Extension (Imawaki et al., 2013).

The average flow of the FC is estimated at 31 ± 4 Sv (Lund et al., 2006; Beal et al., 2008; Imawaki et al., 2013). Negative WSC over most of the North Atlantic contributes a Sverdrup transport of approximately 18 Sv to the Florida Current at 27°N. The remaining water is of South Atlantic origin and is carried through the Straits of Florida by the meridional overturning circulation (DiNezio et al., 2009). Many observational programs have measured the FC, and model studies often use it as a baseline for output validation. Some say that the dynamics and behaviour of this current are by far the best known in the world (Baringer and Larsen, 2001). Submarine cables between Florida and the Bahamas have proven to be extraordinarily useful in using electromagnetic theory to measure the overlying current's transport. The annual variability of the Florida Current is, therefore, well-known thanks to the 16 years of cable measurements (Czeschel et al., 2012). The seasonal cycle from various time periods of measurements can be seen in Figure 2.8. Transport is at a maximum in boreal summer (July) and at a minimum in boreal winter (November-January).

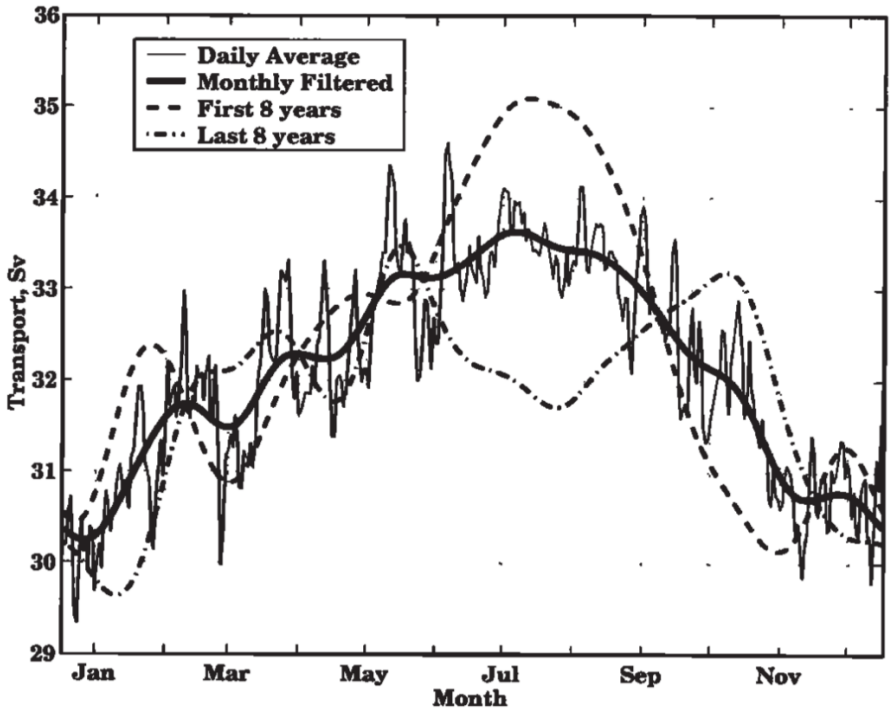

Figure 2.8: *Seasonal cycle of the Florida Current measured by underwater cables over 16 years from 1982 to 1998. From Baringer and Larsen (2001)*

The Gulf Stream System experiences different annual phasing in transport at different locations (Stommel, 1965). For example, while the maximum in flow in the Florida Straits occurs in June, the maximum transport just off Cape Hatteras is in April. The seasonal variation in the northern portion of the system is reportedly a response to a combination of wind and thermal forcing (Fu et al., 1987). Czeschel et al. (2012), however, showed that in the FC, thermohaline forcing plays no apparent role in determining the seasonal fluctuations, and that the seasonal cycle is driven by wind forcing alone.

Niiler (1973) first observed that the Sverdrup relation does not hold for the seasonal adjustment of the FC, as the summertime maximum in transport does not correspond with the wintertime maximum in WSC over the North Atlantic. Many studies have therefore proposed that local and regional winds dominate the seasonal variability in the Straits, as Rossby waves from remote forcing are either too slow to communicate changes on seasonal

time scales, or are blocked by the Bahamian Island chain (DiNezio et al., 2009; Rousset and Beal, 2011). Model analysis has exposed the importance of along channel winds in forcing the current's variability on seasonal timescales (Anderson and Corry, 1985). Observational studies have somewhat differed from this conclusion by highlighting the significance of along isobath forcing providing a link between the Florida Current and the western North Atlantic (DiNezio et al., 2009). This signal is likely communicated by barotropic waves. Baroclinic waves were found to play an important role, but as each baroclinic wave possesses a different phasing, contribution each year is inconsistent (Czeschel et al., 2012). Baroclinic wave are, therefore, considered to contribute to the anomalies of the seasonal signal, and not to determine the seasonal signal itself (Domingues et al., 2016).

The stability of the annual cycle of FC transport has also been investigated as many studies have reported a marked difference in the annual cycle from year to year, along with an occasional strong semi-annual component (Baringer and Larsen, 2001; Rousset and Beal, 2011). The transient seasonal component of the FC is significant, accounting for 27% of the variance (Domingues et al., 2016). Figure 2.9 from Meinen et al. (2010) shows the annual cycle of the current for four different time periods as anomalies from the mean. The current exhibits a strong annual cycle from 1982 to 1990, a significant semi-annual character from 1991 to 1998, and a weak semi-annual cycle in the period 2000 to 2007 with a peak in transport 30 to 50 days earlier than during the 1982 to 1990 window (Meinen et al., 2010). This unexpected change in the phasing of the annual cycle has raised many questions regarding the possible mechanisms modulating the observed shifts. Domingues et al. (2016) used telephone cable measurements from 1985 to 2013 and satellite altimetry from 1993 to 2013 to investigate the drivers of the observed transient seasonal variability. They linked seasonal changes in the FC transport to SSH anomalies in the eastern North Atlantic four to seven years earlier. These anomalies are communicated to the Straits by westward propagating signals resembling first baroclinic mode Rossby waves.

While there has been no absolute consensus on what determines the patterns and amplitudes of the FC's seasonal cycle, most studies agree that barotropic and first baroclinic

mode waves in the eastern portion of the North Atlantic play a major role.

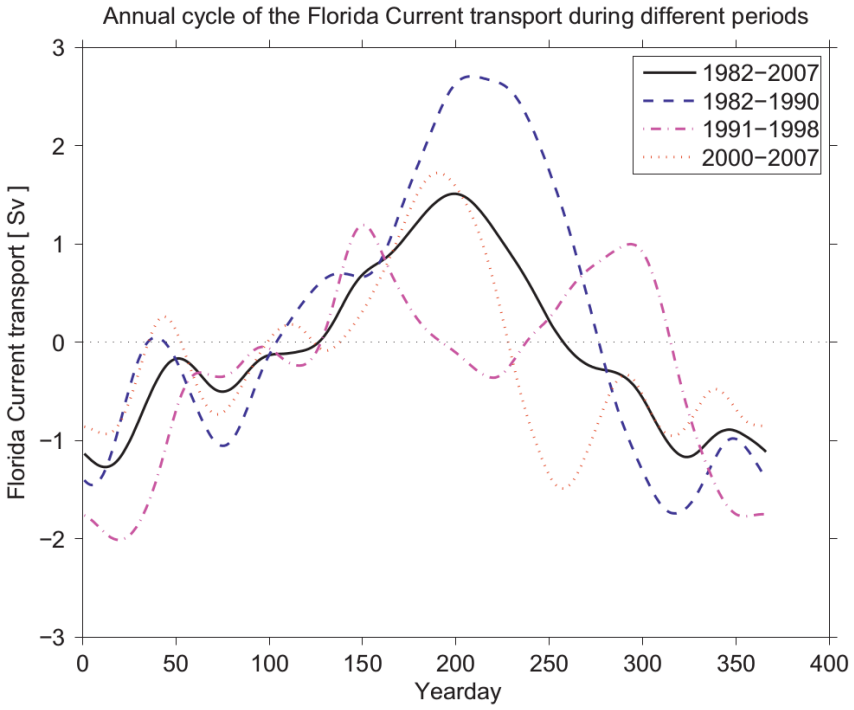

Figure 2.9: *Seasonal cycle of Florida Current transport shown as anomalies from the mean for four time periods indicated in the legend. From Meinen et al. (2010)*

2.7.2 The Kuroshio and the East Australian Current

The Kuroshio Current is the western boundary current of the subtropical North Pacific gyre (see location in Figure 2.7), and has a mean volume transport of 21.5 Sv east of Taiwan. The current originates close to the Philippine coast where the Pacific North Equatorial Current (NEC) splits into the southward flowing Mindanao Current and the northward flowing Kuroshio Current (Qiu and Lukas, 1996). The Kuroshio becomes an identifiable western boundary jet north of the Luzon Strait (22°N) where it receives an addition of water from the interior of the North Pacific wind driven gyre. The current experiences a maximum in transport of 24 Sv in boreal summer (June-July) and a minimum of 20 Sv in boreal winter (November-December) (Johns et al., 2001). The seasonality is said to be driven by

local along channel wind forcing together with Sverdrup forcing over the Philippine Sea (Lee et al., 2001; Johns et al., 2001).

Similar to the bifurcation of the NEC, the South Equatorial Current (SEC) also splits upon reaching the western boundary. The SEC bifurcates at the Great Barrier Reef, flowing north into the Queensland Current and south into the East Australian Current (EAC). The EAC carries 20 Sv southwards as a narrow boundary jet. The seasonal variation of the EAC was investigated by Ridgway and Godfrey (1997) using Expendable Bathythermograph data and the southward flow was found to be at a maximum in austral summer. No link was identified between the seasonal cycle of the current and WSC in the Tasman Sea to its east. Instead, the summertime maximum has been related to strong anticyclonic eddies and to the position of the bifurcation of the SEC, which shifts north from October to December (Ridgway and Godfrey, 1997; Holbrook and Bindoff, 1997; Kessler and Gourdeau, 2007).

Once again, there is no one accepted theory for the mechanisms responsible for setting the seasonal cycles of the western boundary currents of the Pacific Ocean. On the whole, local wind forcing and the bifurcation points of the NEC and SEC are proposed as the main drivers of seasonal adjustments.

2.7.3 The Agulhas Current

The seasonal cycle of the AC has been under debate for many years with no consensus on its principal drivers (Ffield et al., 1997; Biastoch et al., 1999; Matano et al., 2002). Early work that explored the seasonality of the AC was undertaken by Ffield et al. (1997) who investigated the strength of the South Indian subtropical gyre using hydrographic, altimeter, and wind data. They found that the gyre circulation is strongest in March and September, and weakest in December and June. SSH anomalies were used as a proxy for AC strength and showed the same semi-annual cycle (Figure 2.10) (Ffield et al., 1997).

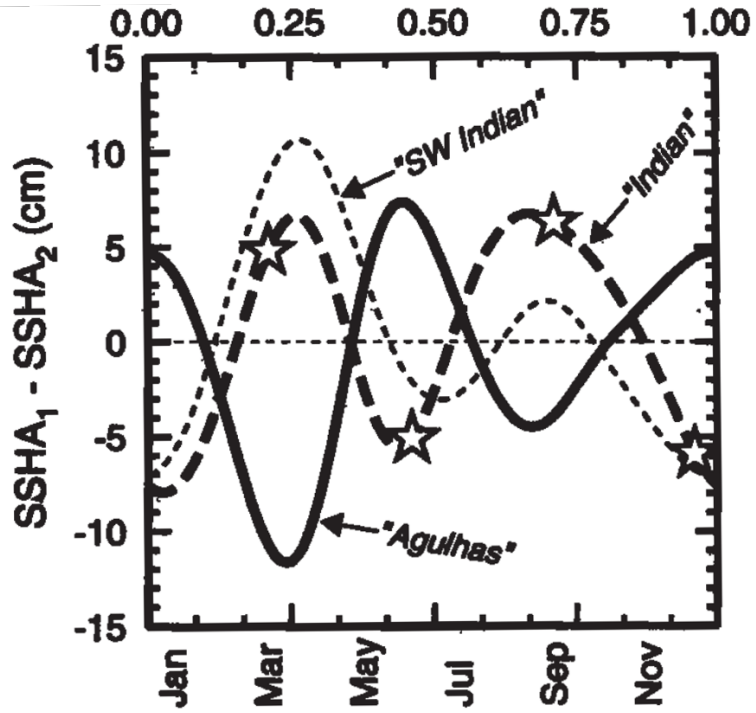

Figure 2.10: *Mean annual difference in sea surface height anomalies (SSHA) across the Agulhas Current (solid line), south-west Indian Ocean (thin-dashed line) and Indian Ocean (thick dashed line). The mean SSHA differences are smoothed with a 6 month Gaussian filter. From Ffield et al. (1997)*

.

Grundlingh (1980) used data from eight research cruises between 1975 and 1978 to calculate geostrophic volume transports of the top 1000m of the AC. The results from this study indicated a maximum in current strength in austral autumn-winter and a minimum in summer-spring. Biastoch et al. (1999) used a primitive equations Modular Oceans Model (MOM2) to study the dynamics of the AC system, including the Mozambique Channel. The flow in the Mozambique Channel was found to be at a maximum in winter (August) when the South Indian subtropical gyre is shifted north, thereby facilitating the advection of more tropical surface water into the Channel. This winter maximum in flow through the Mozambique Channel was confirmed by Ridderinkhof et al. (2010) using direct current meter measurements in the narrowest section of the Channel. The peak in flow was said to

be advected southwards to lead to an increase in AC during October-November (Biastoch et al., 1999). This is illustrated in Figure 2.11 where a 2-3 month lag time is visible between the peaks in flow of the Mozambique Channel and the AC. Biastoch et al. (1999) therefore came to the conclusion that the Mozambique Channel plays a critical role in determining the seasonality of the AC. There is no evidence for seasonality in volume transport of the East Madagascar Current (EMC), and thus this current is not considered to be of primary importance in influencing AC seasonality. It is worth noting that as the flow is southwards in the Mozambique Channel, and south-westwards for the AC, more negative values correspond to stronger currents in Figure 2.11.

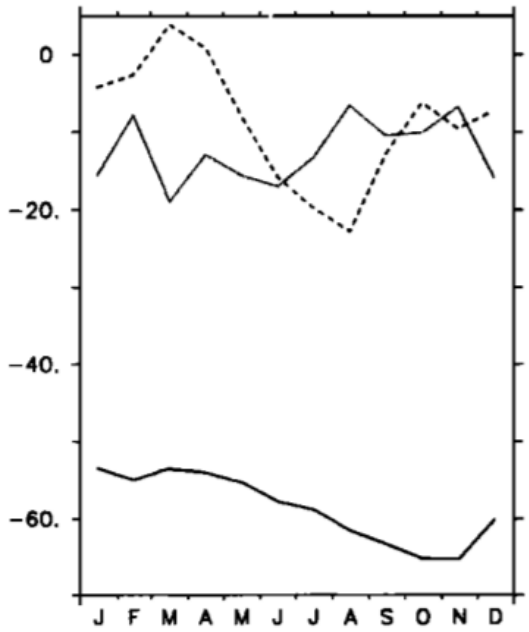

Figure 2.11: *Transport (in Sv) across sections of the Agulhas Current at 32°S (solid), the Mozambique Channel at 23°S (dashed), and the East Madagascar Current at 23°S (dotted) in the Modular Oceans Model (MOM2). Note that more negative values denote stronger southward transports. From Biastoch et al. (1999)*

.

Reason et al. (2003) later used the same regional eddy permitting MOM2 model of Biastoch et al. (1999) and also found greater AC transports in winter (August) than in summer (March). They attributed this seasonality to be driven by the Southern Hemisphere Westerlies which are strongest in winter.

Matano et al. (1999) used a general circulation ocean model to investigate the influence of seasonal variations in wind forcing on the AC. Two experiments were run; one using the thermohaline properties of the Levitus climatology, and another that isolated the barotropic mode by using constant values of temperature and salinity. The results from the experiments showed that although the annual mean circulation of the barotropic and baroclinic experiments differed substantially, their anomalies were similar south of 30°S. Separate modes of variability were found to be delimited by the quasi-meridional bathymetric features. The simulated AC had a similar annual cycle to that proposed by Biastoch et al. (1999), with a maximum southward flow between winter and spring and a minimum between summer and autumn. Matano et al. (1999) suggested that the Madagascar Ridge and the South West Indian Ridge shelter the AC from westward propagating signals originating from winds farther to the east.

The study of Matano et al. (1999) was followed by another investigation by Matano et al. (2002) into the forcing of the AC using an eddy-permitting Parallel Ocean Circulation Model (POCM). Matano et al. (2002) showed the seasonality of the western Indian Ocean to be controlled by barotropic modes that are forced directly by the winds. The seasonal cycle of the AC from Matano et al. (2002) (Figure 2.12) was found to exhibit peak flow in August (transition between winter and spring) and a minimum in February (summer), in agreement with Matano et al. (1999). Note that as Figure 2.12 shows anomalies in transport, a negative anomaly corresponds to a stronger AC.

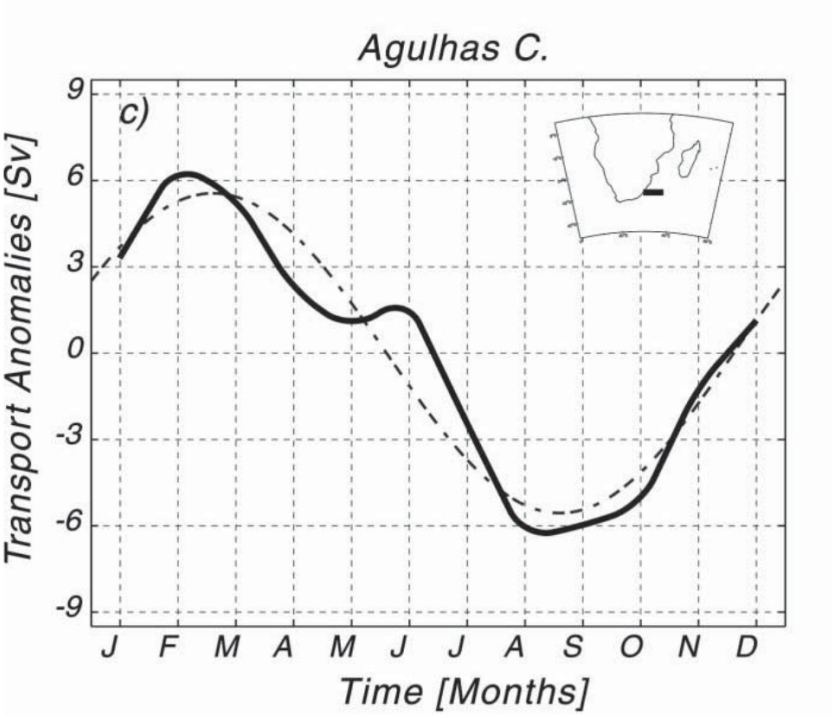

Figure 2.12: *Monthly climatological transport anomalies of the Agulhas Current (AC; solid line) using a Parallel Ocean Circulation Model (POCM) of the Southern Indian Ocean, dotted line shows its annual fit. Negative anomalies correspond to a stronger current as the AC flows south-westwards. From Matano et al. (2002).*

Matano et al. (2002) used harmonic and empirical orthogonal function (EOF) analysis to identify three distinct modes of seasonal variability in the tropical Indian Ocean, each separated by topographic features. The easternmost mode is associated with the ITF and shows no dynamical link with the AC, while the central and westernmost modes appear to be closely related to overlying winds, with a connection to the AC via the SEC and Mozambique Channel. However, Matano et al. (2008) could not find observational evidence for the simulated link between the tropical Indian Ocean and the AC, nor for the aforementioned basin modes. Instead, altimetry data suggest that the seasonal variability of the western Indian Ocean is driven by local wind forcing Matano et al. (2008).

The first study that investigated the annual cycle of the AC using satellite observations

alone was undertaken by Krug and Tournadre (2012). They used 18 years of along-track altimetry and 7 years of sea surface temperature data to investigate the position, width and magnitude of the AC. Results showed a stronger geostrophic current speed in summer (February). According to Van Sebille et al. (2010), sea surface slope can be linked to the full-depth transport of the AC. The increase in geostrophic speed can, hence, be assumed to relate to an increase in the AC transport during summer months (Krug and Tournadre, 2012). This summertime maximum in current strength is opposed to what previous modelling studies had predicted.

Up until 2010 there had been no multi-year *in-situ* measurements of the AC, and so the shape of the seasonal cycle remained a contested issue. This changed when data from the Agulhas Current Time-series (ACT) became available and Beal et al. (2015) presented the observed seasonal cycle of the AC from current meter moorings. The mooring array crossed the AC at 34°S with 39 instruments over 12 sites measuring the AC velocity and transport from 2010 to 2013 at an hourly resolution. The annual cycle of the AC sampled by the ACT array can be seen in Figure 2.13 for both box (transport to the time-mean position of the zero velocity isotach) and jet (poleward transport out to the first maximum of the vertically integrated velocity beyond the half width of the mean jet) estimates (Beal et al., 2015). The seasonality shown in Figure 2.13 is opposite in phasing to the annual cycle of the Mozambique Channel (Ridderinkhof et al., 2010), and does not match the model simulations of Biastoch et al. (1999), Matano et al. (1999), and Matano et al. (2002).

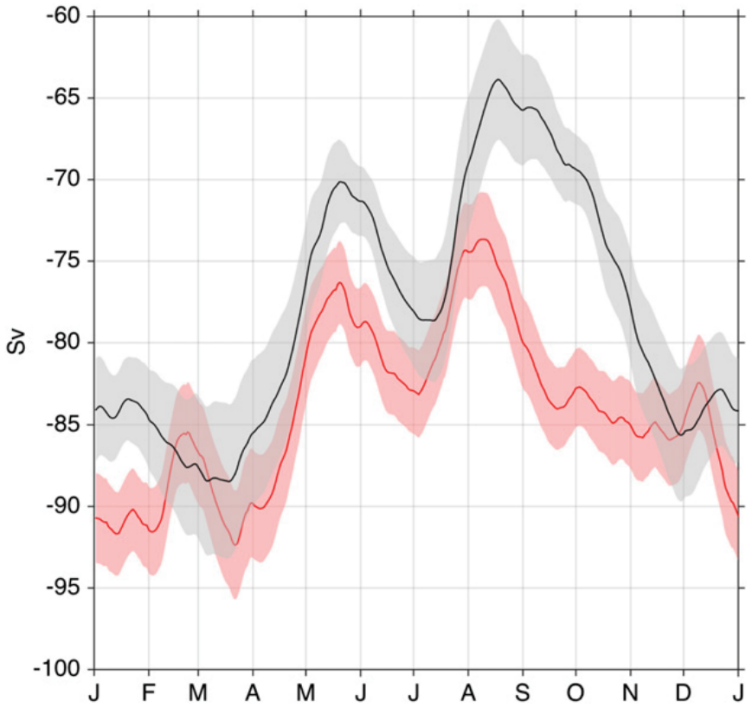

Figure 2.13: *Annual cycle of the Agulhas Current from the ACT mooring array. The box transport is shown in red and the jet in gray. The curves have been filtered using a Nadaraya-Watson kernel estimator with a Gaussian kernel of half-width 30 days. Note that more negative transports correspond to an increase in AC strength. From Beal et al. (2015)*

The position of the ACT array was chosen so that the mooring line directly followed the trajectory of the altimeter ground track number 96. Beal and Elipot (2016) built 9 regression models to relate the local transport at each mooring to the Absolute Dynamic Topography (ADT) slope at that location during each altimeter pass. A 23-year proxy time-series of AC transport was produced. Beal and Elipot (2016) used this proxy to show that the AC is, on average, strongest in March (summer) and weakest in August (winter).

Table 2.14 shows a summary of the various studies that have addressed the seasonal cycle of the AC. The modelling studies of Biastoch et al. (1999); Matano et al. (1999, 2002) and Reason et al. (2003) did not assimilate data, which may explain the incorrect prediction of seasonal maximum and minimum as the models could not be constrained using observations.

The ACT observational data from Beal et al. (2015) and the subsequent 23-year transport proxy Beal and Elipot (2016) both showed that the AC is stronger in summer, confirming the seasonality proposed by Krug and Tournadre (2012). The drivers of this observed seasonality have yet to be explored. This thesis addresses this gap in knowledge by investigating the wind driven contribution to the AC seasonal cycle.

Study	Variable	Maximum	Minimum
Ffield et al. (1997)	Sea Surface Height Anomalies	Summer (March)	Winter (June)
Grundlingh (1980)	Geostrophic Velocities	Autumn-Winter	Summer-Spring
Biastoch et al. (1999)	GFDL Modular Ocean Model (MOM2)	Spring (October-November)	Summer (March)
Matano et al. (1999)	General Circulation Ocean Model	Winter-Spring	Summer-Autumn
Reason et al. (2003)	Regional eddy permitting model based on the Modular Ocean Model (MOM2)	Winter	Summer
Matano et al. (2002)	Parallel Ocean Circulation Model (POCM)	Winter-Spring (August)	Summer (February)
Krug and Tournadre (2012)	Satellite Altimetry	Summer	Winter
Beal et al. (2015)	Current Meter Moorings	Summer (March-April)	Winter (August)
Beal and Elipot (2016)	Transport Proxy	Summer (March)	Winter (August)

Figure 2.14: *Table summarizing the reported maxima and minima of the Agulhas Current seasonal cycle from various studies. Note that "maximum" refers to largest southward-westward (negative) transport.*

.

3 Key Questions and Layout Explained

This thesis is structured so that each results chapter has its own Introduction, Data and Methods, Discussion, and Conclusion sections. The reason for this choice of layout is to facilitate easy reading. Each chapter uses different data and methods, and so it makes sense to locate a description of the respective techniques and data sets in the same chapter as their corresponding results. This is done in place of the more traditional grouping all data and methods together in a single chapter which, in the context of this study, may lead to confusion. There is a final chapter titled "Summary and Concluding Remarks" where the results from all 5 results chapters are linked together and discussed.

The key questions for this study, their motivations, and the respective chapters that address them are as follows:

Chapter 4: How does the Agulhas Current (AC) vary seasonally?
Motivation: Little is known about the seasonal variability of the AC. To address this, the velocity structure and sea surface height patterns of, and around, the AC for summer (January-February-March) versus winter (July-August-September) are explored. The results from this chapter act to inform the interpretation of the idealized model simulations presented in Chapters 6, 7 and 8.

Chapter 5: What is the annual variability of Southern Indian Ocean winds, and what is the nature of the Rossby wave adjustment to this wind forcing?
Motivation: Winds are hypothesized to play a critical role in determining the seasonal transport variability of the western boundary current. The seasonal alterations in wind stress curl (WSC) are thus explored to provide insight into the basin-wide seasonal forcing changes. Results from this chapter inform which wind atlas is most appropriate for further use in this study, and the observed seasonal WSC changes aid interpretation of the reduced gravity model simulations of Chapter 8.

Chapter 6: How does a barotropic adjustment to wind forcing contribute to the observed seasonality of the Agulhas Current?

Motivation: Historic model studies suggest that much of the seasonal adjustment of the Southern Indian Ocean is achieved by barotropic waves. To explore the nature of this barotropic adjustment to wind forcing, and the influence on AC seasonality, a single layer wind driven model is constructed for the Southern Indian Ocean.

Chapter 7: How is the seasonality of the Agulhas Current influenced by a first baroclinic mode adjustment to climatological Indian Ocean winds?

Motivation: Moving beyond the simplest case of a barotropic model presented in the previous chapter, here a first baroclinic mode adjustment to climatological wind forcing is explored using a reduced gravity model. The sensitivity of AC seasonality to Rossby wave speed is investigated and a model solution is presented where the seasonal phasing of the AC is adequately reproduced.

Chapter 8: Which characteristics of Indian Ocean wind forcing predominantly influence the seasonal phasing at the western boundary?

Motivation: The importance of various properties of Southern Indian Ocean WSC in determining the observed seasonal transport phasing of the AC has yet to be explored. To address this, this chapter investigates the influence of zonally varying winds, local winds directly over the current, near- and far-field winds, and background mean wind stress on the seasonality of the AC.

4 Characteristics of Agulhas Current Seasonality

4.1 Introduction

Historic model studies of the South-West Indian Ocean predict a winter-spring maximum in transport of the Agulhas Current (AC) (Biastoch et al., 1999; Matano et al., 2002). Observations from satellite altimetry (Krug and Tournadre, 2012) suggest the opposite seasonality, namely that the current strength is stronger in austral summer. Three years of mooring data, and the resultant 23-year transport proxy from the Agulhas Current Time-series (ACT) experiment confirm this summertime maximum in transport. Models therefore disagree with observations regarding the seasonality of the current. The intention of this chapter is to provide further detail regarding the seasonal variation of the current, adding to the results from the ACT experiment already reported by Beal et al. (2015) and Beal and Elipot (2016). The seasonal characteristics of the AC will be investigated using the velocity profiles from ACT and sea surface height from altimetry. The results from this chapter will inform the interpretation of the idealized model simulations presented in Chapters 6, 7 and 8.

4.2 Key Question

How does the Agulhas Current vary seasonally?

4.3 Data and Methods

4.3.1 The Agulhas Current Time-series Experiment

The ACT experiment ran from April 2010 to February 2013, and provided the first multi-year data set of velocity measurements of the AC. The array consisted of 7 full-depth current meter moorings and 4 Current Pressure Inverted Echo Sounders (CPIES) (Beal et al., 2015). Each current meter mooring consisted of an upward looking Acoustic Doppler Current Profiler (ADCP) that profiled the speed and direction of flow in the near surface layer, and Acoustic Doppler Current Meters (ADCMs) distributed over the rest of the water column

(see Figure 4.1 b). The CPIES were used to estimate the offshore current velocity beyond the geographical extent of the current meters by measuring the round trip travel time of acoustic pulses to the sea surface and back (Kennelly et al., 2007). The velocity and transport approximations from the CPIES were validated by corroborating overlapping velocities measured by mooring G, and were found to be highly correlated with the mooring data. The CPIES, together with the current meter moorings, captured the full AC jet over the entire monitoring period, even during meander events (Beal et al., 2015) (see locations of stations labelled in Figure 4.1).

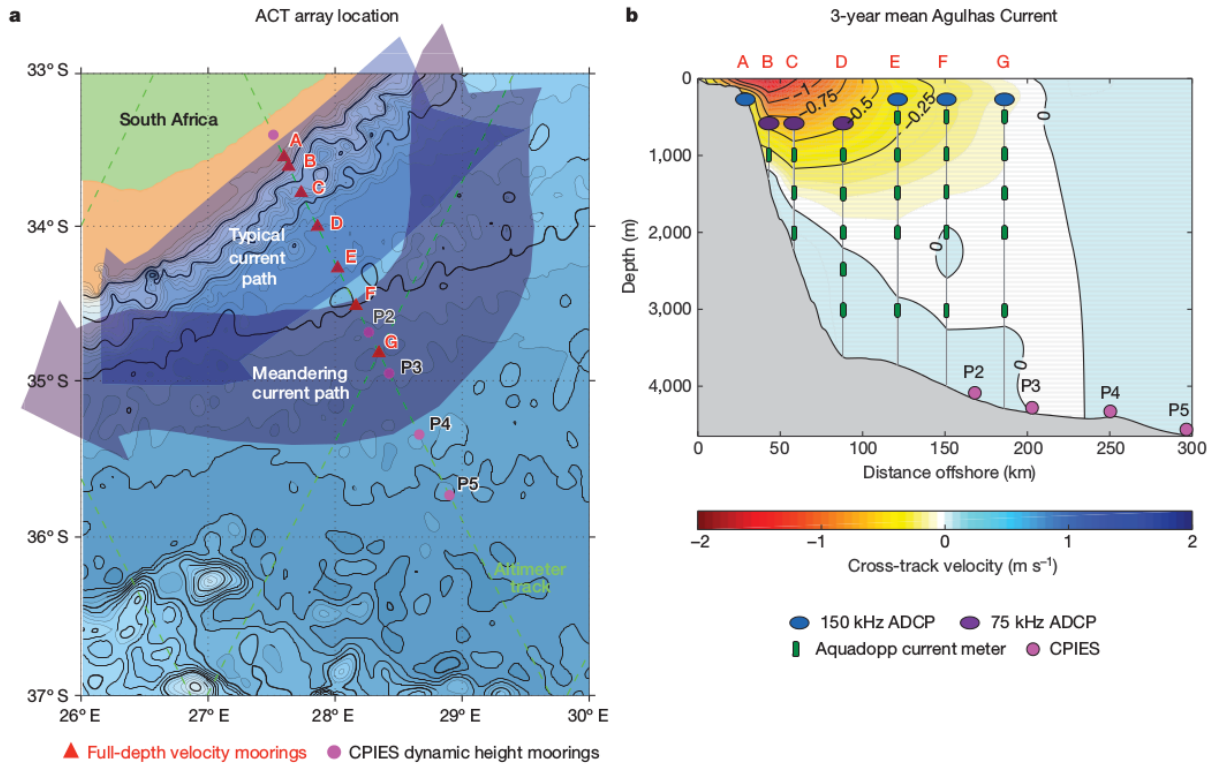

Figure 4.1: *Geographical location of the Agulhas Current Time-series array shown from a bird's eye view in (a) where the positions are overlaid on a background shading showing bathymetry. (b) Vertical section of current showing the 3-year mean cross track velocity. Current meter moorings with ADCPs are located at positions A-G, and CPIES are located at P2-P5. From Beal and Elipot (2016)*

In this study, a gridded product of the array velocities is used. The measurements were interpolated temporally onto 12 hour intervals, and spatially into a vertical grid of 20 meters from the surface down to the ocean floor, and a horizontal grid of 500 meters from the coast out to 300 km offshore (Beal et al., 2015). Where monthly composites are shown, the mean velocities for each month have been computed using a bin average.

Beal et al. (2015) defined two transport estimates, termed Tjet and Tbox. Tjet represents the south-westward jet transport integrated out to the position of the first velocity maximum beyond the length of the half width of the jet (110km). In other words, this estimate only describes the south-westward (poleward) flow of the Agulhas jet and excludes the counter-flows (inertial or eddy-driven re-circulations) at the flanks of the core of the current. Tbox is the 'net' boundary layer transport as it contains both the main south-westward flow and the north-eastward counter-flows. This boundary layer transport is computed out to 219 km offshore. The value of 219 km was chosen as it is the time-mean distance from the coast to the position of the zero velocity isotach (Beal et al., 2015).

The seasonal cycle's of the jet and boundary transports during the ACT mooring observation period were shown in Chapter 2 Figure 2.13. These curves were obtained by Beal et al. (2015) using the Nadaraya-Watson kernel estimator with a Gaussian kernel of half-width 30 days. Both Tbox and Tjet were found to be largest in the southwestward direction during austral summer months (January-March) and minimum during winter (August).

As explained in Chapter 2, Section 2.7.3, a transport proxy was built by Beal and Elipot (2016) to relate the transport at each mooring to the slope of Absolute Dynamic Topography (ADT) at that location during each altimeter pass. Nine linear regression models were built between ADT slope and Tx. The skill, or R^2 values, of these models range from 0.51 at mooring A, to 0.81 over the last CPIES pair (Beal and Elipot, 2016) (see mooring locations in Figure 4.1). An interpolating polynomial function was used to obtain transport values at a 1km resolution across the current. One significant limitation of the proxy, is that it assumes that stratification is not changing over time. This is regarded as an acceptable assumption given the long time scale of water mass changes and the equivalent barotropic nature of the

current (Beal et al., 2015).

It is important to note that the transport proxies presented by Beal and Elipot (2016) possess little skill representing the mean. Hence, the means of the 23-year proxies in the results presented here were constrained to the observed 3-year transport mean from 2010-2013. Figure 4.2 shows the adjusted proxy time-series from October 1992 to April 2016.

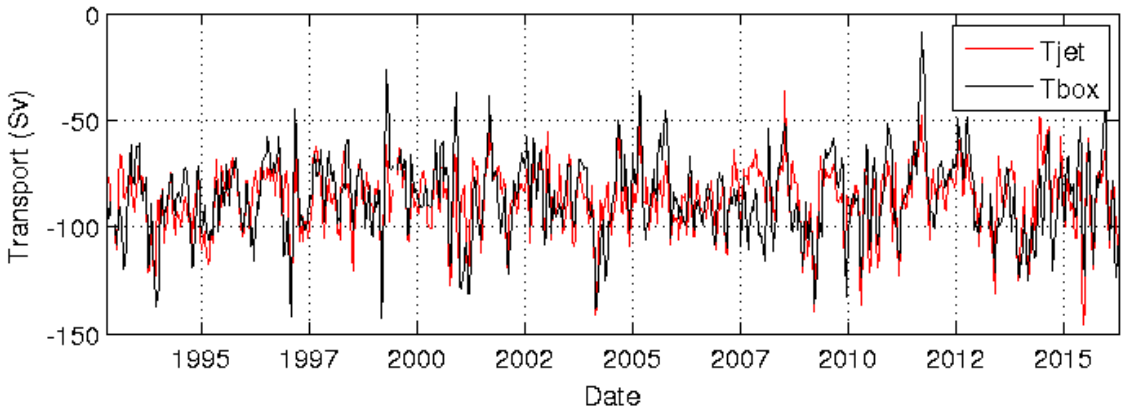

Figure 4.2: *Agulhas Current Time-series (ACT) 23-year transport proxy (Sv) with a 1 month smoothing filter, adapted and recalculated from Beal and Elipot (2016). Jet transport shown in red and boundary layer transport shown in black. Flow direction south-westwards, perpendicular to ACT array, therefore more negative values correspond to an increase in current strength. Adapted and recalculated from (Beal and Elipot, 2016)*

The spectra of the 23-year proxy time-series is shown in Figure 4.3 with 95% confidence shading for a chi-square distribution which was deemed appropriate based on the findings of Beal and Elipot (2016). A multitaper of 5 Slepian tapers was used, using 3 or 7 tapers rendered a similar result. Both the boundary and jet transports have a peak at one cycle per year, the seasonal cycle. The annual cycle peak is significant when compared to a background red spectrum (Beal and Elipot, 2016).

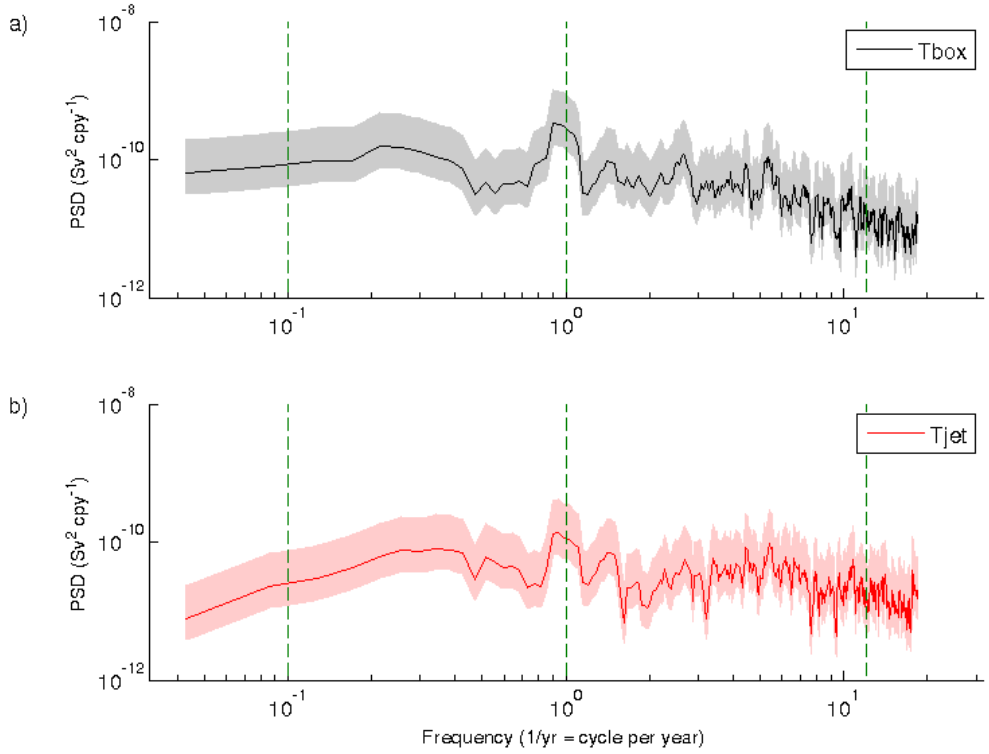

Figure 4.3: *Frequency spectra of 23-year transport proxy time-series using a multitaper with 5 Slepian tapers for a) the boundary layer transport and b) the poleward jet transport. Shading shows the 95% confidence intervals. Vertical lines highlight the frequencies corresponding (from left to right) to 10 years (0.1 cycles/year), 1 year and 1 month (12 cycles/year) periods. Adapted and recalculated from Beal and Elipot (2016)*

694 The seasonal cycle of AC transport from the 23-year proxy is depicted by monthly means
695 in Figure 4.4. The 95% confidence interval assumes a normal distribution which is shown to
696 be reasonable based in histograms of monthly means (see Appendix Figures 12.1 and 12.2
697 as examples).

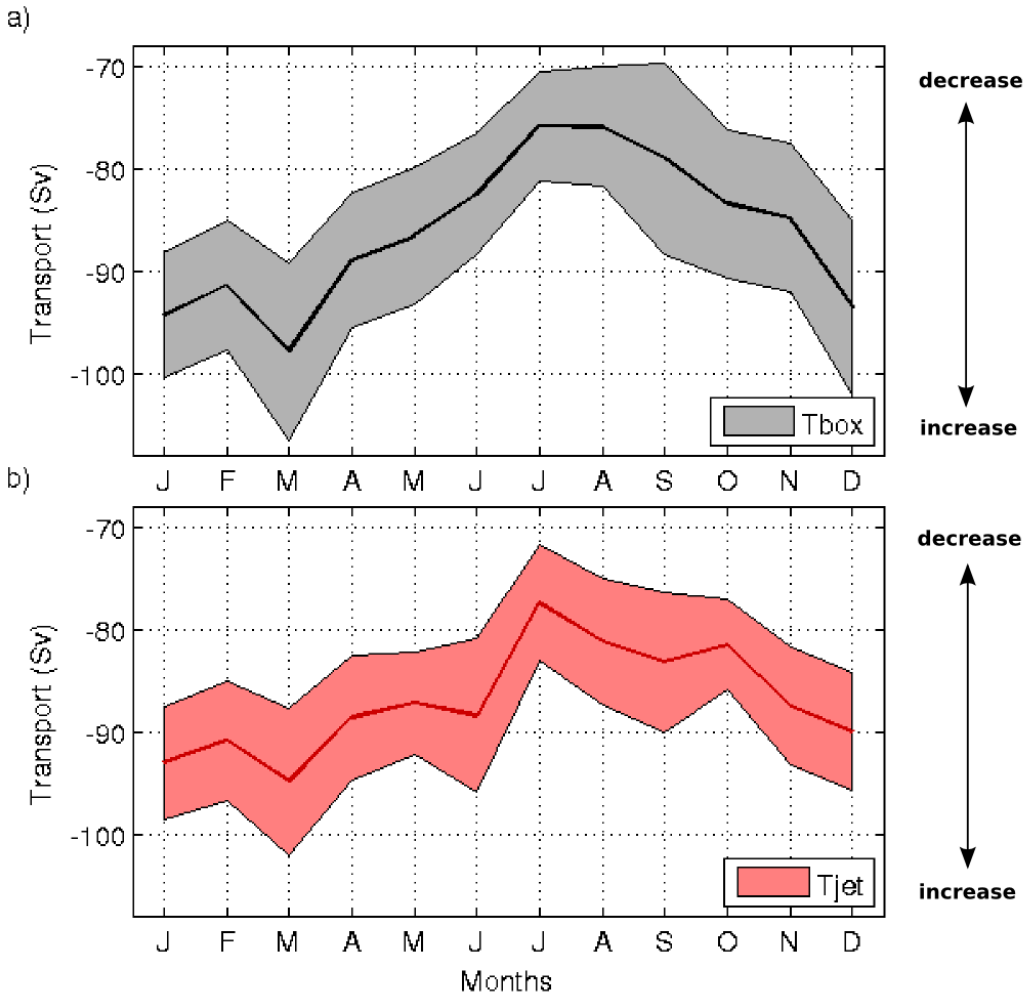

Figure 4.4: *Seasonal cycle of 23-year transport proxy time-series for a) the boundary layer transport (Sv) and b) the poleward jet transport (Sv). Solid lines show the monthly mean values and shading shows the 95% confidence intervals assuming a normal distribution. Note that more negative transport values correspond to an increase in current strength as the Agulhas Current (AC) flows south-westwards.*

698 The transport of the south-westward AC is at a maximum in March and a minimum
699 in July for both the boundary layer and jet estimates. These seasonal cycles compare well
700 with the *in-situ* data, with all estimates indicating a summertime maximum and wintertime
701 minimum in flow. Figure 4.5 shows the seasonal cycle of the boundary and jet transports

for 3 year averages from 1993 to 2016. The phasing of the seasonal cycle is, on the whole, coherent in its summer maximum and its winter minimum over time, even though there is inter-annual variability visible.

For all proceeding chapters, the boundary layer seasonal cycle will be used for comparison with shallow water model results as this is the more traditional transport estimate. The seasonal cycle of the jet transport agrees well with the boundary layer seasonality, indicating that there is no great difference and so either estimate could be used for comparison, but Tbox (boundary layer) is chosen for convenience.

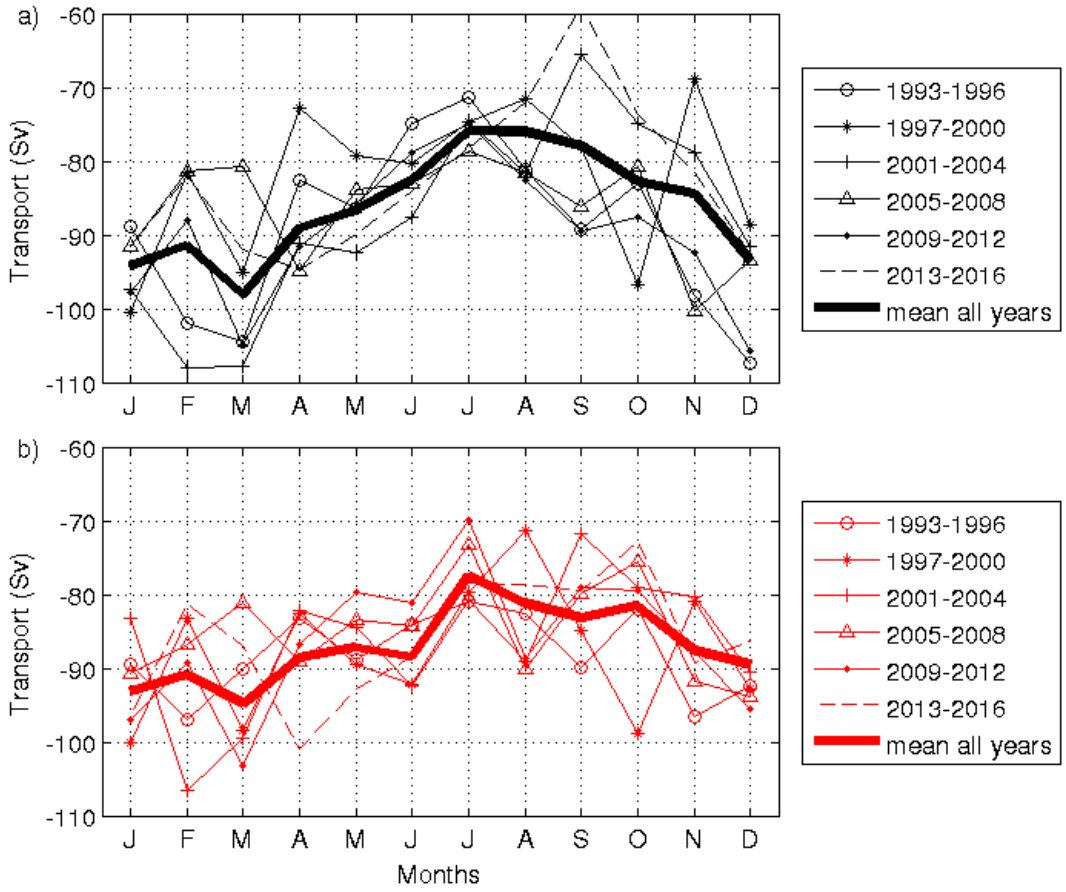

Figure 4.5: *Seasonal cycle of a) the boundary transport (Tbox; Sv) and b) the jet transport (Tjet; Sv) averaged over 3 year time periods from 1993 to 2016.*

4.4 Results

4.4.1 Seasonal Variability of Velocity Structure 2010-2013

The gridded velocities from the ACT *in-situ* data, are used to gain insight into how the AC's velocity structure adjusts between seasons. In particular, the vertical structure of the variability - baroclinic versus barotropic - is examined, to try to infer the dominant mechanisms at play.

Figure 4.6 compares a cross-section of the mean summertime velocity with the winter velocity structure (Figure 4.6). In summer, the core of the current is stronger and broader (seen clearly by the position of the zero velocity isotach in Figure 4.6a). In winter, the current is weaker and the core is shifted farther offshore from the shelf edge (Figure 4.6b). These changes are highlighted in the difference between the summer and winter conditions (summer-winter) shown in Figure 4.6c where a negative anomaly shows that the south-westward flow is stronger in summer than in winter, and vice-versa for a positive anomaly. The cyan shading inshore in Figure 4.6c indicates that overall the surface velocities above the continental shelf edge are 0.2 $m.s^{-1}$ greater in summer than in winter. The positive anomaly located in the upper 500 m, at about 100 km from the coast, reveals that in this 'central' area over the foot of the continental slope, the winter transports are 0.15 $m.s^{-1}$ larger than the mean summer velocities. This represents the offshore shift as the core of the current in winter. This should not be confused with the positive anomaly at depth above the continental slope (Figure 4.6), which represents the Agulhas Undercurrent. An elevated positive anomaly at depth in Figure 4.6c means that the north-eastward flowing Undercurrent is stronger in summer. The full depth negative anomaly from 150 km to 250 km from the coast in Figure 4.6c demonstrates the overall broadening and strengthening of the current associated with the summertime peak in transport.

The mean transport for the January-February-March (summer) composite is -87 Sv, compared to the July-August-September (winter) composite mean of -71.7 Sv. This represents a 17.5% increase in current strength from summer to winter during the 3 years of *in-situ* observations. While the summer-winter changes in the current are surface intensified which

would suggest a baroclinic seasonal pattern, the velocity structure is altered at all depths indicating that the seasonality is equivalent-barotropic.

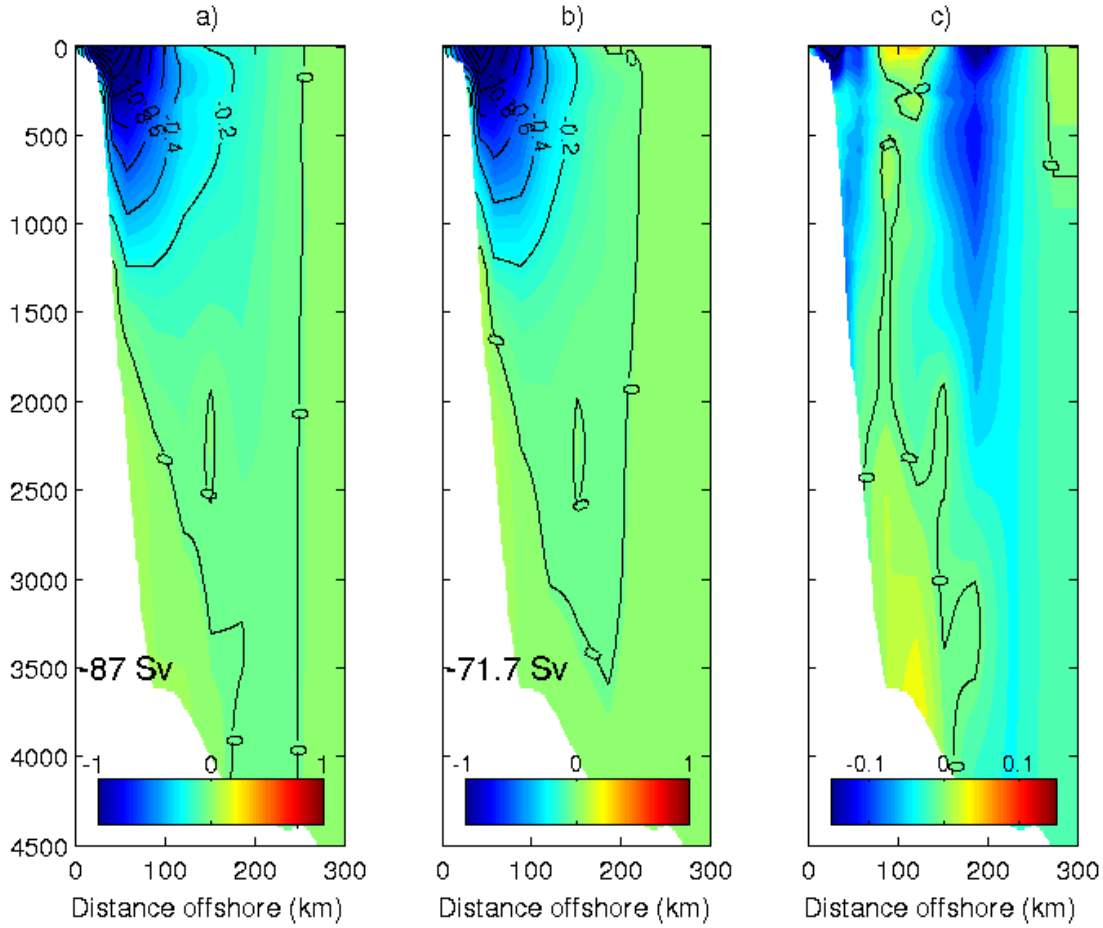

Figure 4.6: *Cross sections of the velocity ($m.s^{-1}$) structure of the Agulhas Current from the ACT in-situ measurements for the a) summer composite of January-February-March, and b) winter composite of July-August-September. The differences (summer-winter) between the two composites are shown in (c). Positive anomalies (red) in (c) indicate a stronger flow in winter than summer, and visa-versa for negative differences (blue). The values quoted on the bottom left of plots (a) and (b) represent the mean 3-month transport for the composite from the 3 years of in-situ data*

Next the year-to-year variability is characterised, so as to explore the coherency of the

seasonality, albeit from only 3 years of data. Figures 4.7 and 4.9 respectively show the monthly mean velocity sections for each summer and winter month during the ACT period for the upper 2000m of the core of the AC. These figures highlight the high levels of inter-annual variability that the current experiences, which must be kept in mind when examining the total monthly averages or seasonal composites. Using February as an example, the mean boundary layer transport for this month from the 23-year proxy is 91.4 Sv (Figure 4.4a). The mean flow was larger than average in 2011 at 103 Sv, dropped in 2012 to a low of 58.9 Sv and then was 'normal' for a February transport in 2013 at a mean of 91.4 Sv (Figure 4.7 d-f). To give insight into what processes drive the inter-annual variability, maps of sea level anomaly (SLA) that correspond to the months shown in Figure 4.7 are provided in Figure 4.8. A stronger February AC (2011) is associated with a large positive SLA offshore (an anticyclonic eddy) which increases the SSH gradient across the AC. This results in a deep, broad current where the flow is entirely poleward over the upper 2000 m of the inner 219 km of the AC (Figure 4.7d). The opposite SLA pattern corresponds to a weaker than average February AC, where a cyclonic (negative SLA) feature is visible along the offshore flank of the current, and a small anticyclone is located inshore (Appendix Figure 4.8e). This SLA pattern forces the core of the AC inshore, bringing the zero velocity isotach in to a distance of 100 km from the coast, with a consequent decrease in mean monthly boundary layer transport (Figure 4.7e).

The lowest 'summertime' transport shown in Figure 4.7 is 48.5 Sv in January 2011. A large meander was passing through the ACT line during this time (Elipot and Beal, 2015). The meander caused cyclonic circulation on the inshore edge of the current (Figure 4.8a) and an upward intrusion of the Agulhas Undercurrent (Figure 4.7a). A limitation of the fixed distance of integration (out to 219 km offshore) of the boundary layer transport is that during a large meander, such as that of January 2011, the current is shifted out of the limits of 'Tbox', resulting in a low reported transport (Elipot and Beal, 2015).

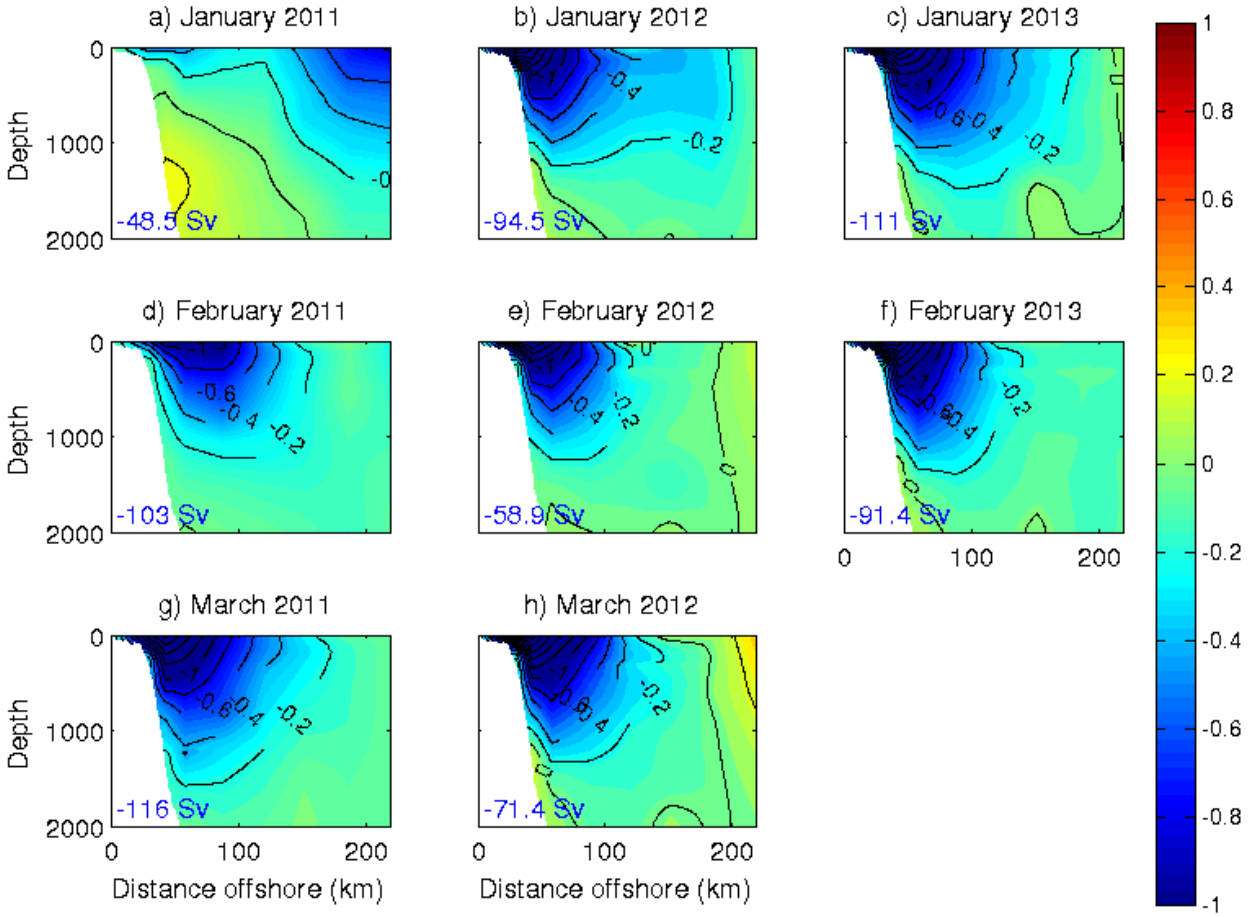

Figure 4.7: *Summertime cross sections of velocity ($m.s^{-1}$) measured by the ACT experiment. Only the upper 2000 m and the inshore portion of the current out to 219 km is shown. 219 km is the horizontal extent of the area of the boundary layer transport integration - the width of the Eulerian mean current (Beal et al., 2015). The values quoted on the bottom left of the plots represent the mean boundary layer transport (Tbox) for the month (Sv). Negative flows are south-westward.*

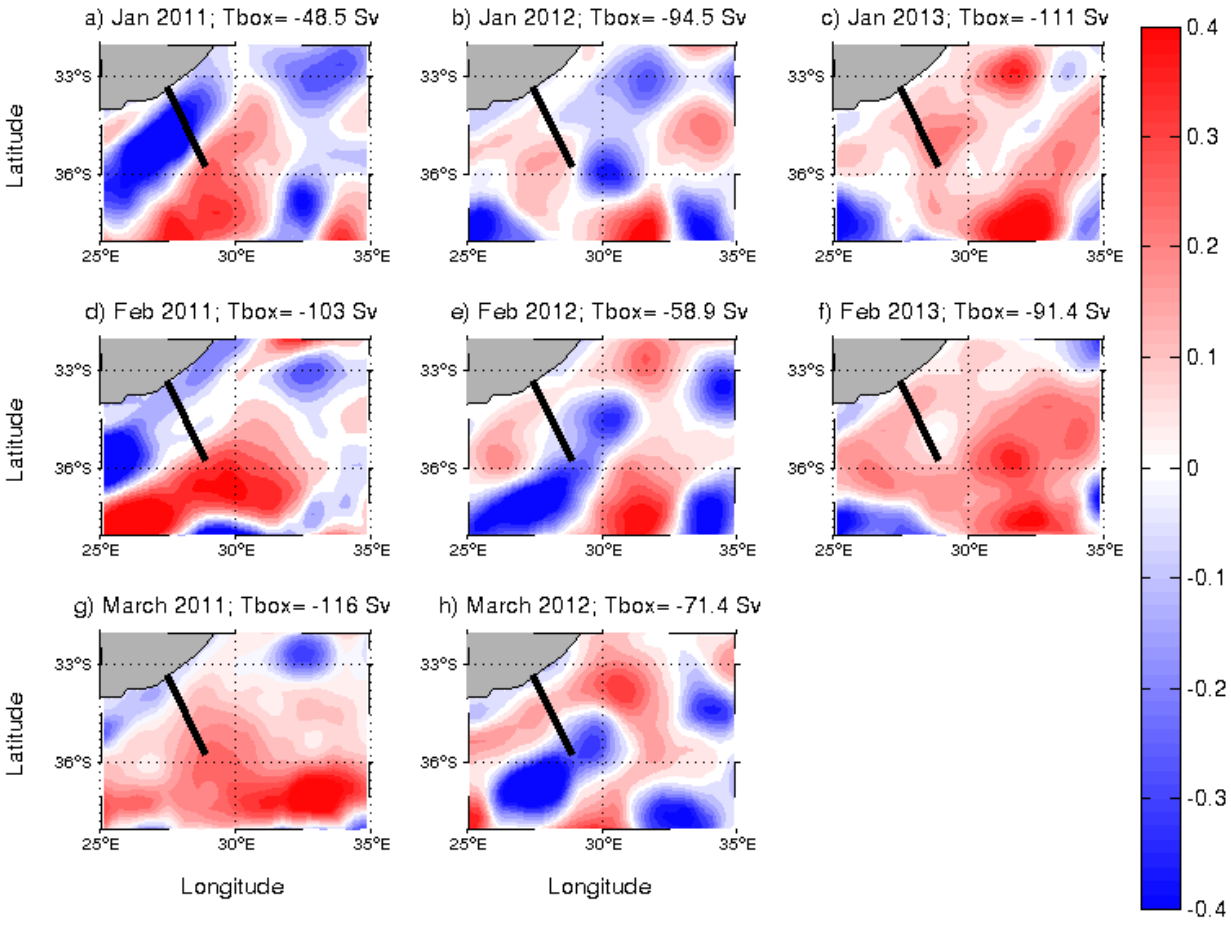

Figure 4.8: *Composite of summertime sea level anomaly (SLA; dynamic meters) maps for in-situ ACT observation period. Position of the ACT array is marked in black. Mean transport of the Agulhas Current perpendicular to the ACT line for that month is quoted in the title of each plot.*

September 2011 is a wintertime outlier (Figure 4.9h), as the mean AC boundary layer transport dropped to -7.78 Sv. This low net transport was due to the presence of a large cyclonic eddy on the offshore flank of the current (Figure 4.10h), resulting in strong northward velocities offshore of 120 km. A larger-than-usual wintertime flow can be seen in September 2010 where a positive SLA (anticyclone) is located at the offshore edge of the ACT array (Figure 4.10g). This steepens the sea surface height (SSH) gradient across the AC,

broadening the current and increasing the volume transport (Figure 4.9g).

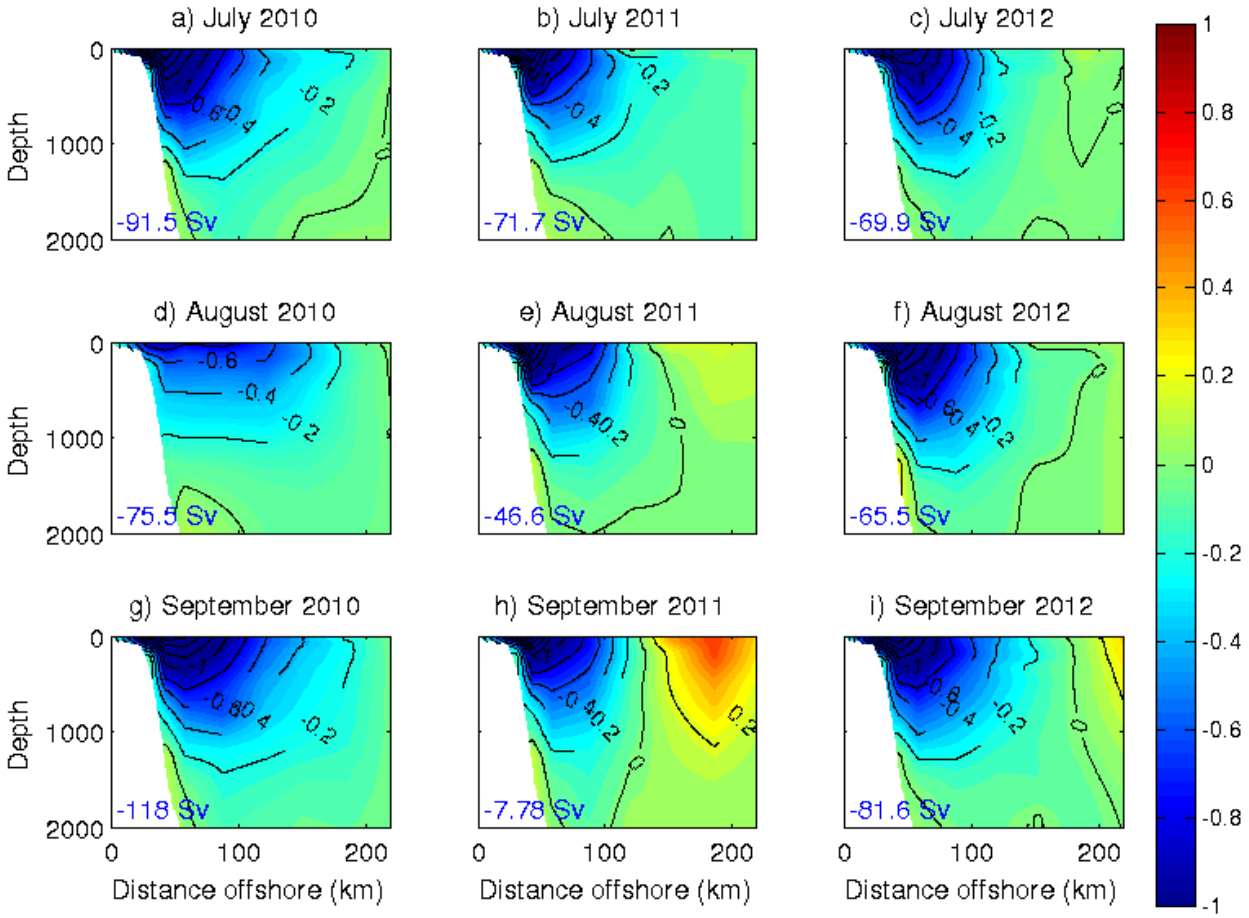

Figure 4.9: *Wintertime cross sections of velocity ($m.s^{-1}$) measured by the ACT experiment. Only the upper 2000 m and inshore core of the current are shown. The values quoted on the bottom left of the plots represent the mean boundary layer transport (Tbox) for the month (Sv). Negative flows are south-westward.*

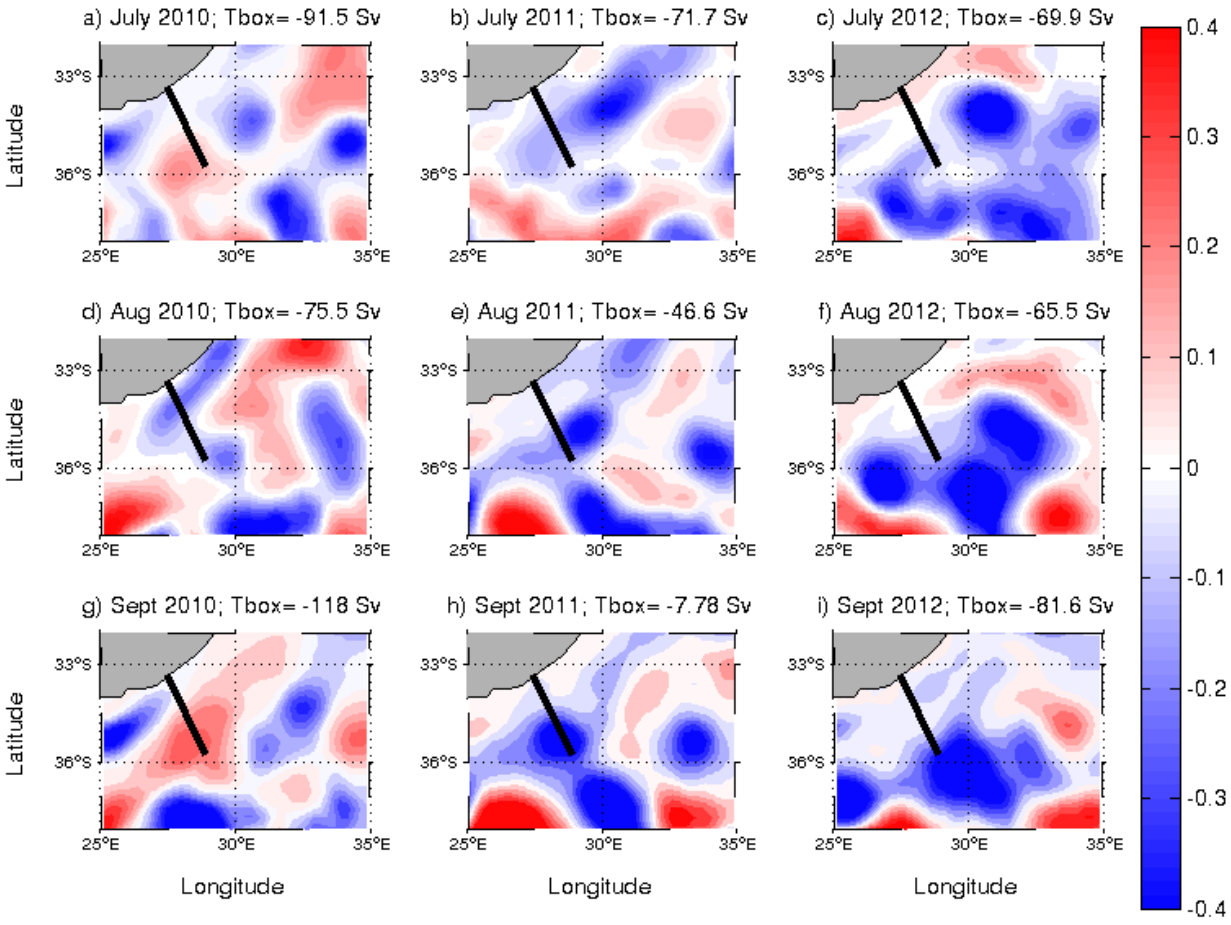

Figure 4.10: *Composite of wintertime sea level anomaly (SLA; dynamic meters) maps for in-situ ACT observation period. Position of the ACT array is marked in black. Mean transport of the Agulhas Current perpendicular to the ACT line for that month is quoted in the title of each plot.*

In summary, the monthly mean velocity cross sections indicate that the year-to-year (interannual) variability of the AC is dominated by meanders and eddies. While this analysis is event based, it is useful in demonstrating the high levels of turbulence present in the AC, and thus exposes the challenge of modelling such a variable system. Over the 23-years of the AC transport proxy, the average standard error of the boundary layer transport is 3.5 Sv. The amplitude of seasonal change from the 23-year transport proxy 22 Sv (Figure 4.4),

indicating that the year-to-year transport variability is 6 times smaller that the seasonal transport variability.

4.4.2 Seasonal Variability of Sea Surface Height

To give further context to the seasonal transport changes (Figure 4.4), and the velocity structure changes (Figure 4.6), composites of SSH are analysed. Figure 4.11 shows the mean SSH for the area around the ACT line for both the three years of *in-situ* measurements (sub-plot a and b) and the 23 years of the transport proxy (sub-plot c and d).

The summertime broadening of the current is clearly visible in Figure 4.11 a and c where larger SSHs are found at the offshore end of the array. The 1.2 dynamic meter contour is closer to the coastline during summer, further supporting the previous observation that the core of the AC, and thus the steepest SSH gradients, are closer inshore in summer. There seems to be a localized offshore recirculation about this region of elevated SSH at the edge of the ACT line. In winter, the 1.2 dynamic meter contour shifts away from the coast, indicating both a decrease in SSH gradient over the AC (and thus a weaker current), and a shift in the core of the current offshore. Two patches of lower SSH can be seen at the southern border of the SSH maps of Figure 4.11. These are associated with the Agulhas Return Current (ARC).

The similarity in the mean dynamic topography of the three year 2010-2013 composites (Figure 4.11 a and b) to the 1993-2016 long time-period composite (Figure 4.11 c and d) is striking. This indicates that while there is sizeable interannual variability (Figures 4.7 and 4.9), the overall summer maximum in transport associated with a steeper SSH gradient over the current, and winter minimum in transport associated with a weaker SSH gradient, holds for both the 3 year *in-situ* monitoring period and the long term 1993-2016 period.

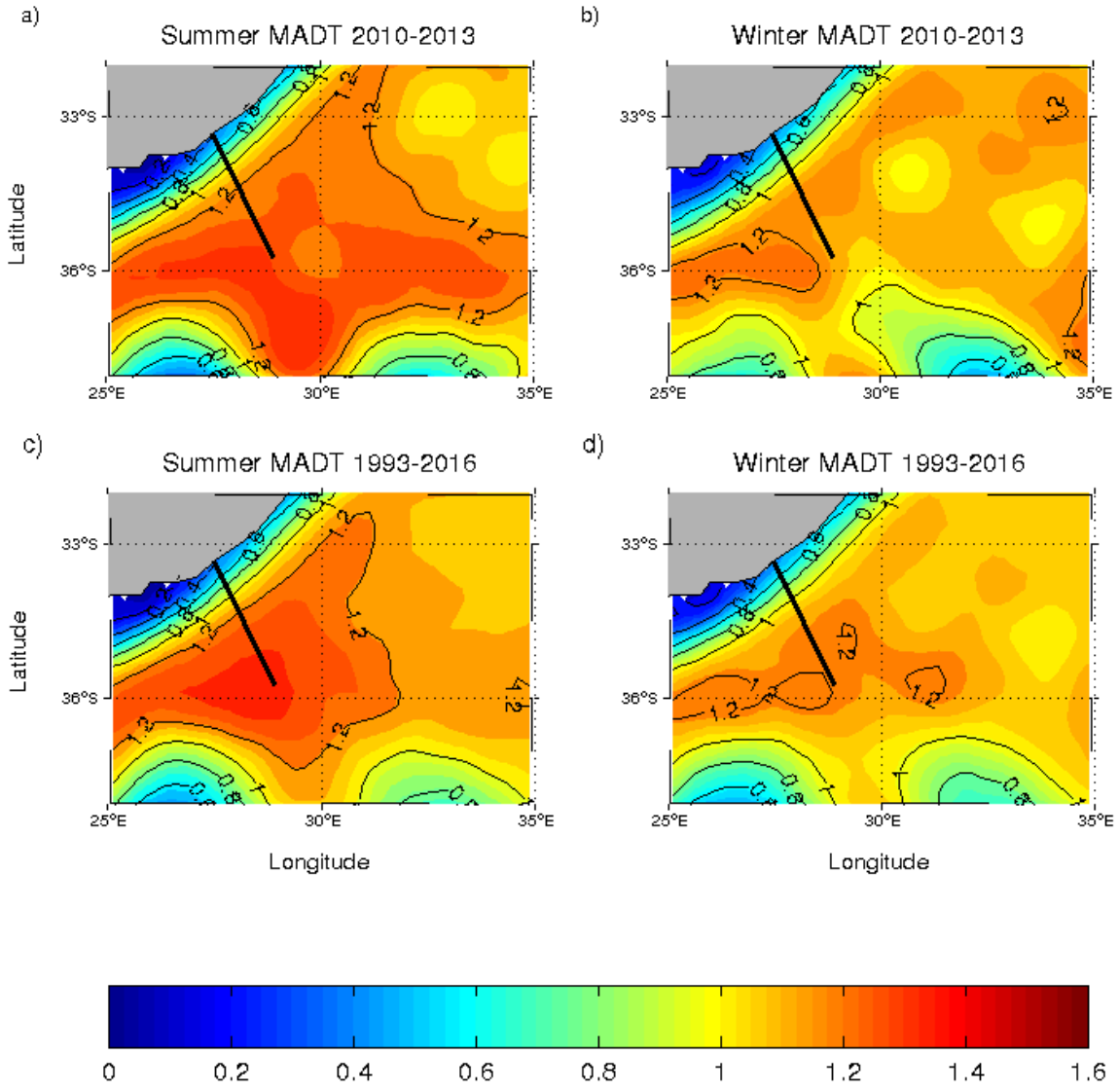

Figure 4.11: *Summer (January-February-March) and winter (July-August-September) mean Maps of Absolute Dynamic Topography (MADT, dynamic meters) for a) and b) the period of the in-situ ACT measurements, and c) and d) the 23-year proxy. Position of ACT array is overlaid in black.*

4.5 Summary and Discussion

Results from the 23-year transport proxy indicate that the AC is stronger in its south-westward direction in summer (March) and weaker in winter (July) (Figure 4.4). The summer transport maximum is associated with a broadening of the jet, but at the same time an intensification of its core over the shelf break. Thus, the summer-winter velocity difference is bimodal with a strengthening of the core and flank of the current and a weakening in the middle, aligned with the foot of the continental slope. In winter, the jet is narrower and its core shifted offshore (Figure 4.6). The seasonal velocity alterations are therefore equivalent barotropic, as even though the largest magnitude of change is concentrated in the upper 1000 m, there are summer-winter differences in transport at all depths. The mean transport of the current increases by 17.5% from winter to summer. Compared to the strong variability of the annual cycle of the Florida Current (Figure 2.9), the annual cycle of AC transport is more robust, with the seasonal phasing remaining consistent when computed over various time periods (Figure 4.5).

The velocity cross sections give a two-dimensional picture of how the AC changes with seasons. To provide further insight into the nature of these seasonal changes, maps of SSH for the region on and around the ACT line were investigated. The inshore SSH did not show sizeable changes with seasons, instead the largest SSH alterations were on the offshore flanks of the AC (Figure 4.11). Year-to-year anomalies from the annual cycle are characterised by mesoscale features related to eddies and meanders. Overall, the summer strengthening of the jet is associated with a regional-scale SSH maximum suggestive of a recirculation cell at the offshore end of the ACT array and pointing to a possible role for inertia supported by a stronger AC jet in summer or local winds over the current. Casal et al. (2009) found no evidence for a mean inertial (barotropic) recirculation between 30°S and 36°S in the AC, but did not investigate the possibility of seasonal recirculation. In winter, the offshore SSH decreases in magnitude, flattening the SSH gradient across the current. These patterns are true for both the 2010-2013 composite and the 1993-2016 long period composite. Whether the increase in SSH gradient in summer is the cause of an increase in flow, or a symptom of

the stronger current, is impossible to discern from the available observations.

A plausible mechanism to explain the sizeable seasonal variability of the AC is seasonal changes in wind stress curl (WSC) pumping across the Southern Indian Ocean. Having characterised the annual cycle of the AC and shown that it is robust, the dynamics that may explain its phasing are explored in the next chapters.

4.6 Conclusion

Based on 3 years of *in-situ* observations and a 23 year transport proxy, the AC is strongest in its south-westward transport in austral summer and weakest in austral winter. This seasonal cycle is robust as the summer maximum falls outside of the winter minimum's 95% confidence envelope. Stronger summertime transports are associated with a broader current and a stronger core of the AC jet. There is some variation in the structure of the current between the summer months of different years, but overall this summer peak in flow is linked to an elevated SSH gradient across the current driven by a positive SLA on the offshore flank of the AC. In winter the core is shifted slightly offshore, and the current becomes narrower and weaker, corresponding to a decrease in SSH gradient across the AC. Southern Indian Ocean WSC is hypothesized to contribute significantly to the seasonal adjustments of the AC, and will therefore be investigating in the next chapters.

5 Climatological Indian Ocean Winds

5.1 Introduction

Wind driven ocean circulation theory suggests that the variability of a western boundary current is related to the large-scale wind stress pattern over the ocean basin to the east of the current (Anderson and Corry, 1985; DiNezio et al., 2009; Atkinson et al., 2010). This would suggest that the observed annual cycle of the Agulhas Current (AC) is related to the large scale pattern of wind stress curl (WSC) over the Southern Indian Ocean (Biastoch et al., 1999). This wind stress variability is communicated across the basin by Rossby waves (Gill, 1982; Killworth, 2001; Subrahmanyam et al., 2001). Theoretically, when there is an alteration in WSC over the Indian Ocean, there is an adjustment of the circulation within the basin, ultimately resulting in a modification in the volume transport of the western boundary current. The objective of this study is to describe the role that Indian Ocean climatological winds play in determining the seasonal variability of the AC. This chapter examines climatological wind stress data and sea surface height (SSH) data for the Southern Indian Ocean. Results from the shallow water model experiments will depend on the wind forcing applied across the basin and on the nature of the Rossby wave adjustment to this forcing. This chapter thus explores the annual cycle of WSC over the Southern Indian Ocean from three wind products and investigates the nature of Rossby wave adjustments at the latitude of the AC. These results will help with the interpretation of the results from the shallow water model experiments presented in Chapters 6, 7, and 8.

5.2 Key Question

What is the annual variability of Southern Indian Ocean winds, and what is the nature of the Rossby wave adjustment to this wind forcing?

5.3 Data and Methods

5.3.1 QuikSCAT Winds

The NASA Quick Scatterometer (QuikSCAT) collected measurements of surface winds over 10 years, from July 1999 to November 2009 (Risien and Chelton, 2008). From these measurements, Risien and Chelton (2008) created a Scatterometer Climatology of Ocean Winds (SCOW) which provides monthly mean maps of wind stress at a 0.25° resolution that are reportedly able to capture small-scale features that are not resolved in other observational atlases (Chelton et al., 2006; Risien and Chelton, 2008). More information regarding the data processing associated with generating the QuikSCAT climatology can be found in Risien and Chelton (2008).

5.3.2 ERA-Interim Winds

ERA-Interim is a global atmospheric reanalysis dataset produced by the European Centre for Medium-range Weather Forecast (ECMWF). ERA-Interim covers the period from 1979 onwards, however only data from July 1999 to November 2009 were used here so that a comparison can be made with QuikSCAT wind fields. The spatial resolution of the wind stress data is 0.25° (Collins et al., 2012). For the purpose of this study, a climatology was created from the monthly mean ERA fields for the Southern Indian Ocean. For more detail regarding the ERA forecast model and the data assimilation method, refer to Dee et al. (2011).

5.3.3 NCEP-NCAR

The United-States National Center for Environmental Prediction and the National Center for Atmospheric Research (NCEP-NCAR) collaborated to produce a global reanalysis of atmospheric fields (Kalnay et al., 1996). The NCEP-NCAR project began in 1991 and has generated updated products every approximately 5 years until the present. The basic idea of the reanalysis project was to use a "frozen state of the art" analysis system to perform data assimilation from 1948 onwards (Kalnay et al., 1996; Collins et al., 2012). The data

used here is a climatology computed from NCEP-NCAR wind fields for the period July 1999 to November 2009 to facilitate a comparison with QuikSCAT data. The NCEP-NCAR wind data possesses a spatial resolution of 2.5°. For more details regarding the NCEP-NCAR reanalysis process, please refer to (Kalnay et al., 1996).

5.3.4 Calculation of Wind Stress Curl

WSC describes the difference in the horizontal shears (vorticity) of the wind stress, given by Pedlosky (1971); Talley (2011):

$$curl\tau = \frac{\partial \tau_y}{\partial x} - \frac{\partial \tau_x}{\partial y} \tag{17}$$

Where τ_x is the east-west (zonal) wind stress (x-plane) and τ_y is the north-south (meridional) wind stress (y-plane). Equation 17 was used to compute the WSC from the various wind stress products.

5.3.5 Sverdrup Transport

The Sverdrup Relation describes the response of the ocean to overlying wind stress forcing (Equation 1), stating that the magnitude of the depth integrated meridional transport at one geographical point is proportional to the overlying WSC (Sverdrup, 1947). Please refer to Section 2.3 for a full description of Sverdrup Dynamics and see Appendix Section 12.2.2 for the full derivation of the Sverdrup Relation. In short, the Sverdrup Relation describes how WSC drives convergence or divergence within the upper ocean, consequently forcing Ekman pumping or suction at the base of the mixed layer. This, in turn, results in a squashing or stretching of the lower section of the water column (Sverdrup, 1947; Pedlosky, 1987). In mid-ocean regions, where friction is small, potential vorticity is conserved (Equation 3), and so a water column will shift to a position of higher or lower planetary vorticity (move poleward or equatorward) in response to overlying WSC. To conserve mass, this meridional transport must be compensated by a flow of equal magnitude, but opposite in direction, located at the boundary (Stommel, 1948). In the case of the south Indian Ocean subtropical

gyre (referred to here as the Southern Indian Ocean), this flow is the poleward AC. This current flows within the frictional western boundary layer thereby removing the vorticity imparted to the Southern Indian Ocean gyre by the overlying positive WSC. The Sverdrup transport was calculated from each wind stress product at every point throughout the basin using Equation 1, and the cumulative transport was obtained by summing the values along the same line of latitude to the east of each point.

5.3.6 Radon Transform

Rossby wave speed can be estimated from patterns of propagating sea level anomalies (SLA) using a Radon Transform. The Radon Transform searches for the direction of largest signal intensity along a line that is normal to a varying angle (Cipollini et al., 2006). The transform 'follows' peaks and troughs in the data, finds their angle of alignment, and determines the dominant direction of signal propagation (De La Rosa et al., 2007). A 2D Radon Transform is used in this study to detect the zonal phase speed of SLA across the Southern Indian Ocean. The SLA data is de-trended to take into account the influence of sea level rise. It is important to note that the transform tool cannot differentiate between eddies and the SSH disturbance associated with a periodic baroclinic Rossby wave (Chelton and Schlax, 1996). This is not a problem, however, as first order baroclinic waves travel westwards at very similar speeds to eddies (Chelton et al., 2007), and so a simple determination of phase speed of SLA is sufficient for the purposes of this study. AVISO (Archiving, Validation and Interpretation of Satellite Oceanographic data) satellite altimetry SLA data is used.

5.4 Results

5.4.1 Seasonal Comparison of Wind Products

To assess the proficiency of the WSC climatologies (described in Section 5.3) in capturing the seasonal differences in WSC, the summer versus winter wind fields for each wind product are compared in Figure 5.1. The high spatial resolution of QuikSCAT is evident as small-scale WSC features are well resolved (Figure 5.1 a and b). The QuikSCAT maps are very

detailed compared to the lower spatial resolution of NCEP-NCAR, where the general pattern is represented, but there is little skill in capturing localised features (Figure 5.1 e and f). For example, mesoscale features related to atmosphere-ocean coupling can be seen over the frontal and eddying regions of the AC, the Agulhas Return Current and the East Madagascar Current in the QuikSCAT data (Figure 5.1 a and b) but are smoothed out in the NCEP-NCAR data (Figure 5.1 e and f). The ERA reanalysis product has the same resolution as the QuikSCAT scatterometer data, however smaller scale features are smoothed out in the ERA product. This is possibly an artefact of the reanalysis procedure aiming to achieve a more spatially coherent representation of WSC. All wind products agree on the general WSC pattern over the Southern Indian Ocean, with negative WSC over the tropics and positive WSC over the mid-latitudes.

Comparing the summer (January-February-March) means on the left hand side of Figure 5.1 with the winter (July-August-September) means on the right hand side reveals how the basin-wide WSC shifts between seasons. In summer the negative WSC of the equatorial regions extends further south and east. In winter, the positive WSC over the center of the basin strengthens and shifts further north, limiting the southward extent of the negative WSC in the tropics, and introducing an area of negative WSC at the southernmost edge of the domain.

The largest differences between wind stress atlases occur close to the coasts. QuikSCAT shows a distinct shift in the value of coastal anomalies between seasons (Figure 5.1 a and b). In summer, negative anomalies along the west coasts of Africa, Madagascar and Australia are strong. These anomalies weaken in winter, except along the South-East coast of Africa where the negative WSC strengthens. The same pattern can be seen in the ERA data, although there is less spatial definition (Figure 5.1 a and b). The NCEP-NCAR WSC pattern is, in general, in good agreement with QuikSCAT and ERA, with small disagreements such as areas of near-zero WSC off the South-East coast of Africa and south of Australia in both summer and winter.

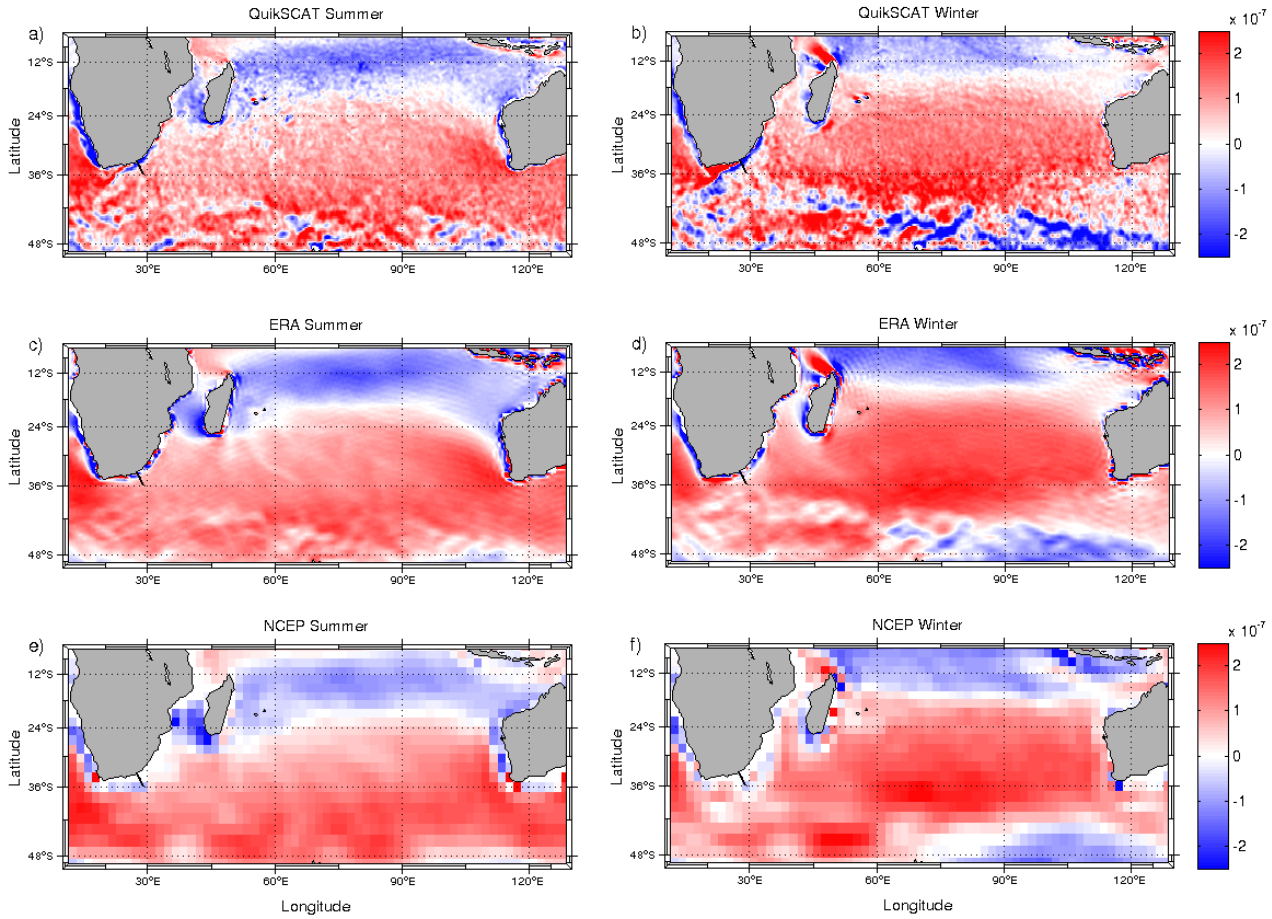

Figure 5.1: *Wind stress curl ($N.m^{-3}$) during summer (January-February-March) and winter (July-August-September) for the Southern Indian Ocean computed from various products. a) and b) QuikSCAT, c) and d) ERA, e and f) NCEP-NCAR. Position of ACT line shown in black off Southern Africa.*

Figure 5.2 shows the summer versus winter Sverdrup transports of the Southern Indian Ocean for each wind product. Note that the Island Rule technique is not applied here for the sake of computational simplicity and the fact that the focus of the study is at 34.5°S where there is no topographical blocking of the western boundary. Integration starts at the eastern boundary of the basin and moves westwards. In the case of the southernmost portion of the Indian Ocean, where there is no clear coastal barrier, the integration is commenced

980 at 160°E.

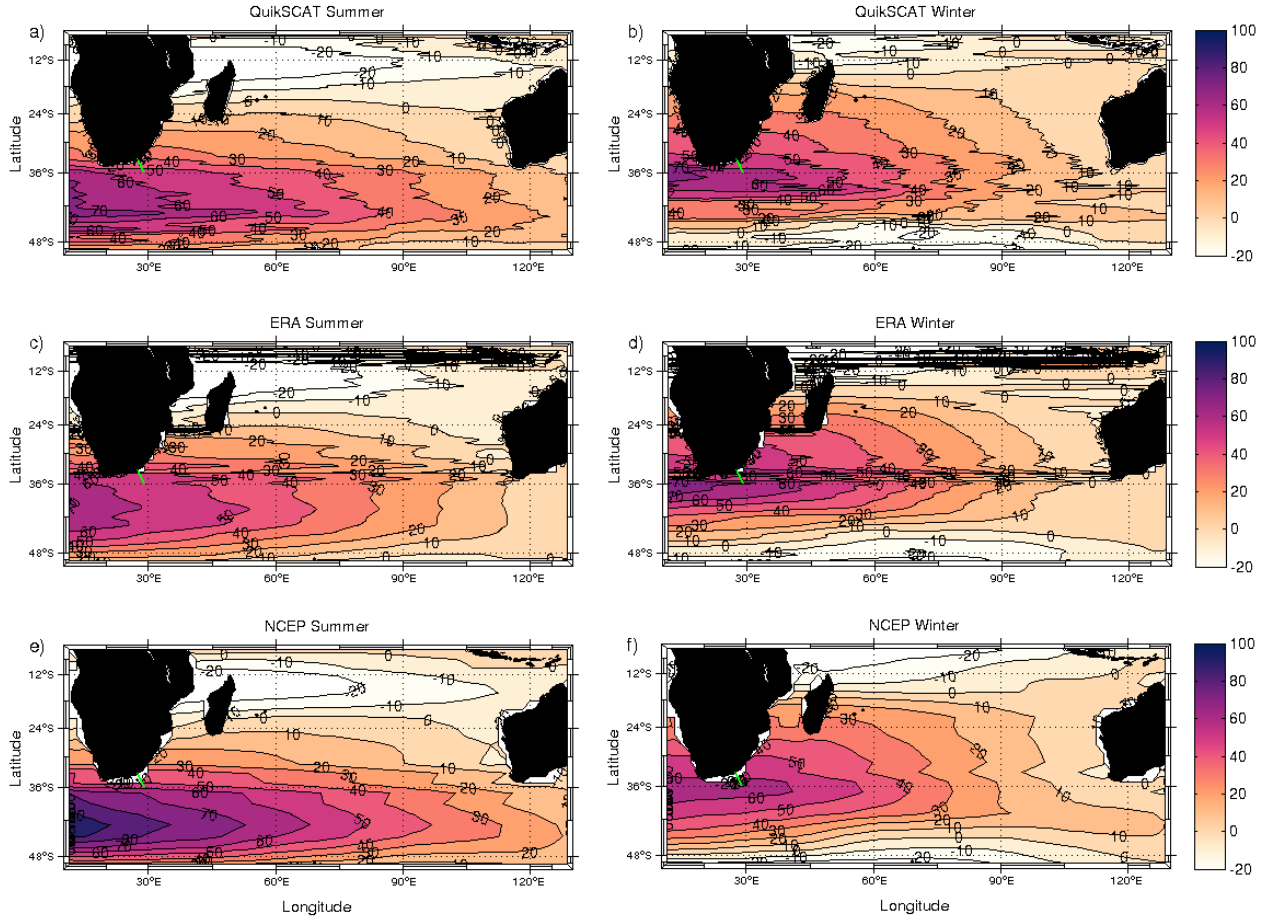

Figure 5.2: *Sverdrup transport (Sv) for the Southern Indian Ocean computed from a) and b) QuikSCAT, c) and d) ERA, e) and f) NCEP-NCAR. Position of ACT line shown in green off Southern Africa.*

981 The wintertime northward shift in maximum WSC can clearly be seen in Figure 5.2 for
982 all wind atlases, as the location of maximum Sverdrup transport shifts closer to Africa. The
983 differences in the wind atlas' skill in resolving features close to the coast observed in Figure
984 5.1 seem to have little bearing on the basin-wide Sverdrup transport with QuikSCAT, ERA
985 and NCEP-NCAR all predicting similar gyre transports. While all wind datasets represent
986 the same wintertime northward shift in maximum of WSC driven transport, the details of the

seasonal basin-wide structure of this transport do differ between products, with the higher resolution datasets exhibiting more jagged transport contours (Figure 5.2). In summertime, the NCEP-NCAR Sverdrup transport south of Africa is larger than the other products with a maximum wind driven transport of 90 Sv, compared to the 70 Sv maximum of the both QuikSCAT and ERA.

Sverdrup theory states that the western boundary current acts to balance the volume of water pumped into the basin by wind stress. It does so by providing an exit route of water south-westwards out of the Indian Ocean basin and simultaneously removes the vorticity imparted to the basin by the winds (Sverdrup, 1947). In the case of the Southern Indian Ocean, this is accomplished by the AC. The monthly mean wind driven component of the AC can thus be obtained by integrating the Sverdrup transport across the basin at the mean latitude of the Agulhas Current Time-series (ACT) mooring line for each month. This calculation could be performed anywhere along the western boundary, and in fact, the magnitude of the transports would increase the further south one goes as this approaches the latitude of maximum wind stress. However, as this study focuses on results at the location of the ACT experiment, the integration was performed for the mean latitude of the ACT line (34.5°S) and the mean volume transport obtained for each month (see Figure 5.3). It is important to note that the Sverdrup balance assumes an instantaneous adjustment to WSC forcing across the basin, while in reality this is not the case as Rossby waves take time to transit the basin and communicate the WSC signal to the western boundary.

The results from each wind product, for each month, are shown in Figure 5.3. There is a good agreement in the monthly implied WSC driven transport at the ACT line for all wind atlases. These winds would hypothetically drive a maximum in southward transport at the latitude of the ACT line in winter (July-August-September) (Figure 5.3). All wind datasets indicate a semi-annual minimum in WSC driven transport with QuikSCAT and ERA at a minimum in April-May and November, and NCEP-NCAR at a minimum in April, June, and November (Figure 5.3). The implied Sverdrup transport at ACT from NCEP-NCAR winds is, on average, larger than the other wind products with annual mean of -52.8 Sv

versus means of -49.0 Sv, -49.6 Sv for QuikSCAT and ERA respectively. The similarity between ERA and QuikSCAT may be largely explained by the assimilation of QuikSCAT measurements into the ERA reanalysis product.

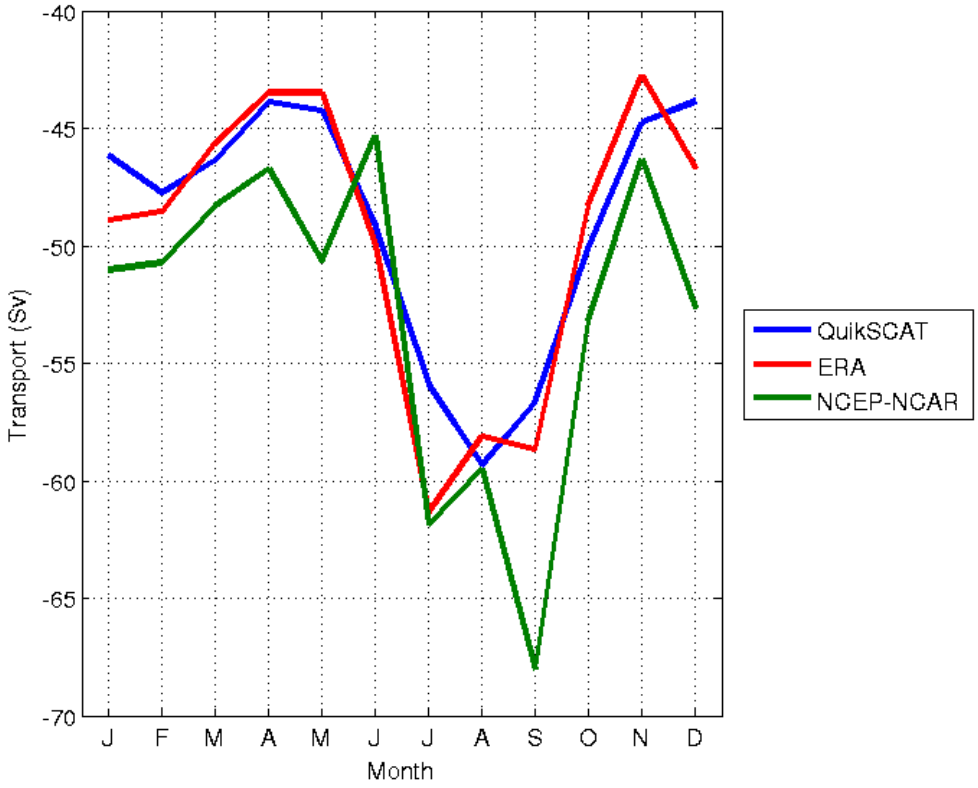

Figure 5.3: *Comparison of seasonal cycles of implied Sverdrup transport at the ACT line for various wind products: QuikSCAT (blue), ERA (red), and NCEP-NCAR (green). Note as this implied Sverdrup transport is southwards, a stronger western boundary flow is associated with more negative transport values.*

5.4.2 QuikSCAT Wind Stress Variability

QuikSCAT winds have a high spatial resolution of 0.25° and span a 10 year period during the middle of the ACT proxy time-series. The wind comparisons presented in Section 5.4.1 highlighted the skill of QuikSCAT in capturing smaller scale WSC features, and showed a good

agreement in seasonal Sverdrup transport with the other wind products. QuikSCAT was deemed the most appropriate for further investigation of the seasonal wind stress alterations across the Southern Indian Ocean.

Figure 5.4 shows the annual mean QuikSCAT WSC over the Southern Indian Ocean with wind stress vectors overlaid. The strong westerly winds can be seen in the southern portion of the domain (south of 40°S), leading to the generally positive wind stress curl over the central Southern Indian Ocean.

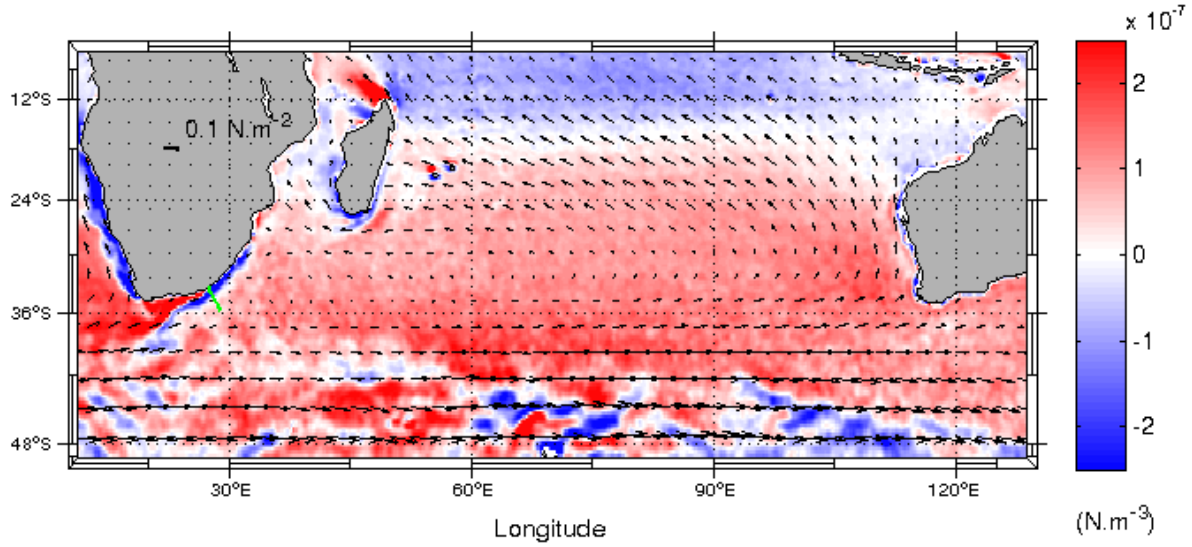

Figure 5.4: *Mean QuikSCAT wind stress curl ($N.m^{-3}$) over the Southern Indian Ocean as background shading overlaid with wind stress vectors ($N.m^{-2}$).*

An Empirical Orthogonal Function (EOF) analysis is conducted to explore the spatial variability of the climatological QuikSCAT WSC fields. The first EOF (Figure 5.5) captures 55 % of the variance of QuikSCAT WSC, and the spatial pattern of the anomalies in Figure 5.5a indicate that the majority of the wind stress curl variability over the Southern Indian Ocean is associated with seasonal meridional shifts in the winds. The changes associated with the first EOF appear to largely represent the seasonal variability, given the cosine shape of the principal component (PC) (Figure 5.5b).

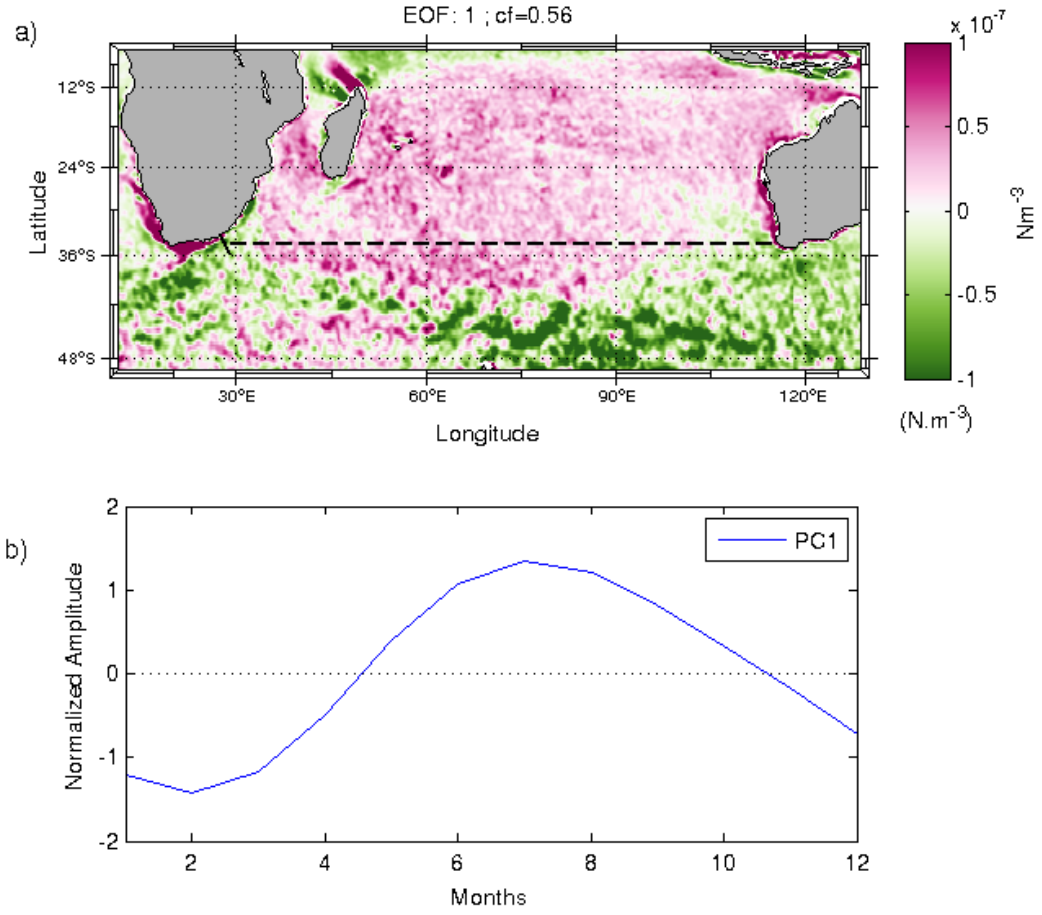

Figure 5.5: *a) First Empirical Orthogonal Function (EOF) of climatological QuikSCAT wind stress curl data. b) Principal Component (PC) time-series of EOF shown in (a).*

Figure 5.5a shows that the Southern Indian Ocean is divided in the seasonality of WSC with the mid-latitudes and tropics exhibiting opposite seasonal anomalies to the southern portion of the domain. This is indicative of the seasonal North-South shift in the wind fields. In austral summertime (beginning and end of year shown on x axis of Figure 5.5b), the principal component (PC) is negative. This indicates a stronger negative WSC over the tropics, weaker positive WSC over the mid-latitudes (20°S to 35°S), and the weaker negative WSC south 36°S. This corresponds to southern position of the Southern Hemisphere wind belts, the trade winds and the westerlies, during austral summer. This pattern inverts

during winter, when the westerlies and trade winds shift northwards, thereby strengthening the positive WSC over the interior of the Indian Ocean, and decreasing the strength of the negative WSC over the tropics.

The seasonal WSC trends are not zonally coherent at the mean latitude of the ACT line (34.5°S, dotted line in Figure 5.5a) as the anomalies at the eastern and western boundaries are opposite in sign to the anomalies over the center of the basin (Figure 5.5a). It is thus challenging to gauge the seasonal WSC changes specifically at the latitude of ACT from Figure 5.5. To clarify this, Figure 5.6 shows the zonal pattern of WSC at the mean latitude of the ACT line (34.5°S) averaged for each season, with the zonal mean overlaid in green. There is little change in value of the zonal mean WSC between spring (October-November-December, summer (January-February-March), and autumn (April-May-June). In winter, however, zonal mean WSC is significantly stronger. While the zonal means are similar from spring to autumn, the pattern of WSC across the basin, is not. In summertime the WSC over the eastern boundary is double the strength of the mean WSC over the whole basin. In winter, the opposite is true, where the WSC at the eastern and western boundaries drop, and the curl over the center of the basin increases. There is no one longitude where the WSC is identifiably strong during all seasons.

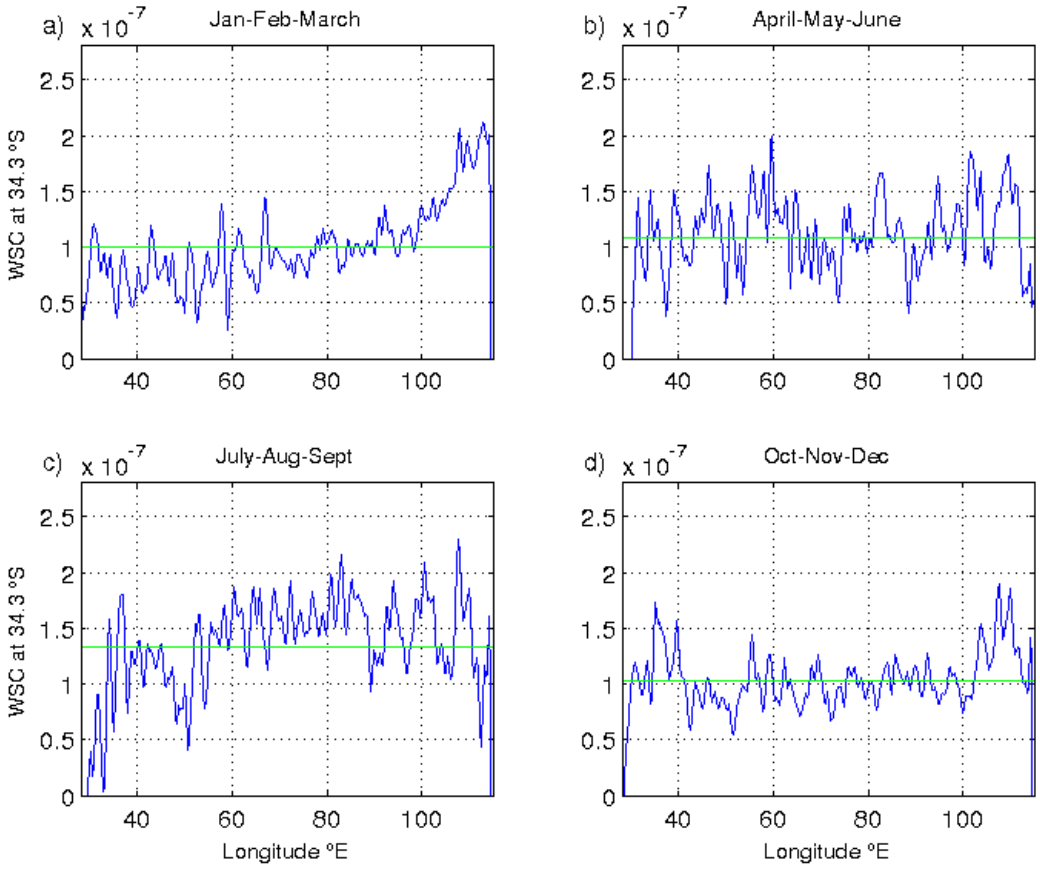

Figure 5.6: *Longitudinal variation of seasonal QuikSCAT wind stress curl (WSC; $N.m^{-3}$) across the Southern Indian Ocean at 34.5°S for a) summer, b) autumn, c) winter and d) spring. Mean seasonal zonal WSC shown in green*

The integrated effect of these seasonal WSC changes is embodied in the monthly mean Sverdrup transport shown in Figure 5.7 for both the climatological QuikSCAT winds (blue) and an estimate computed from the inter-annual wind stress QuikSCAT product spanning the time period 1999 to 2009 (purple). These Sverdrup transports are compared to the seasonal cycles of the boundary (Tbox) transport from the ACT proxy calculated during the QuikSCAT period (black). As mentioned previously, the Sverdrup transport from QuikSCAT winds increases in winter and drops in summer. This is true for both the climatological estimate and the inter-annual. This seasonal cycle is opposite to the seasonality reported

by the ACT proxy. There is evidently not an instantaneous adjustment of the western boundary to WSC fluctuations across the basin at a seasonal timescale as when the wind driven transport is strongest, the current is weakest (Figure 5.7).

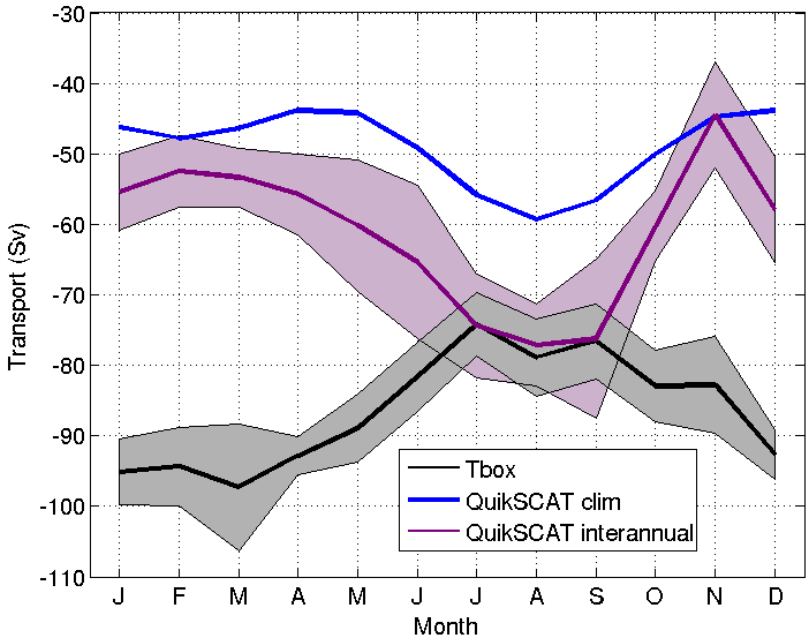

Figure 5.7: *Comparison of ACT proxy boundary layer transport proxy (black) during the QuikSCAT operational period with the seasonal cycle of implied Sverdrup transport at the ACT line from climatological QuikSCAT winds (blue) and inter-annual QuikSCAT winds (purple) from 1999-2009. Shading shows the 95% confidence intervals - note that the seasonal estimate has no error shading as there is by construction no inter-annual variability in this estimate.*

5.4.3 Rossby Wave Propagation in the Southern Indian Ocean

Results presented in Section 5.4.2 revealed that there is not an instantaneous adjustment of the AC to WSC forcing over the Southern Indian Ocean. Winds drive a maximum Sverdrup transport in August (winter) while the results from the 23-year proxy show that the AC is strongest in March (summer). Rossby waves are likely important in communicating the

WSC signal, and so their propagation speed at the latitude of the ACT line is examined here using a Radon Transform on SLA data.

Figure 5.8a shows the results from a 2D Radon Transform performed on SLA data across the Southern Indian Ocean in the latitude range of the ACT line. The minimum speed that the transform can detect is 1.5 $km.day^{-1}$, as the angle associated with slow propagation speeds is too small for the Transform to detect. Figure 5.8a shows that anomalies propagate slowly in the eastern portion of the basin, with speeds dropping to, or below, 1.5 $km.day^{-1}$ at all latitudes over the longitude range 75°E to 95°E. Anomalies speed up towards the western boundary, with SLA propagation speeds reaching a maximum of 5 $km.day^{-1}$ around 33.5°S; 29°E (Figure 5.8a). The observed increase in propagation speeds towards the West is consistent with theory as Equation 15 states that the Rossby radius of deformation is directly proportional to H (depth of the pycnocline/wind driven layer). Pycnocline depth (along with SSH) increases westwards across an ocean basin due to the geostrophic circulation of the gyre. The radius of deformation then also increases westwards and so does the phase speed of baroclinic Rossby waves (Equation 16). Similarly, the SLA speeds are greater in the northernmost portion of the ACT line as this is a position of lower planetary vorticity (f), and the baroclinic Rossby radius of deformation is inversely proportional to f. This does not, however, explain why there is a region of elevated propagation speeds around 100°E, and why speeds then drop in the center of the basin. There is no evidence indicating that this is related to topography (see Appendix Figure 12.3 showing depth of sea floor along 34.5°S). Interference with overlying WSC is one plausible mechanism to explain these observed changes in Rossby wave speed.

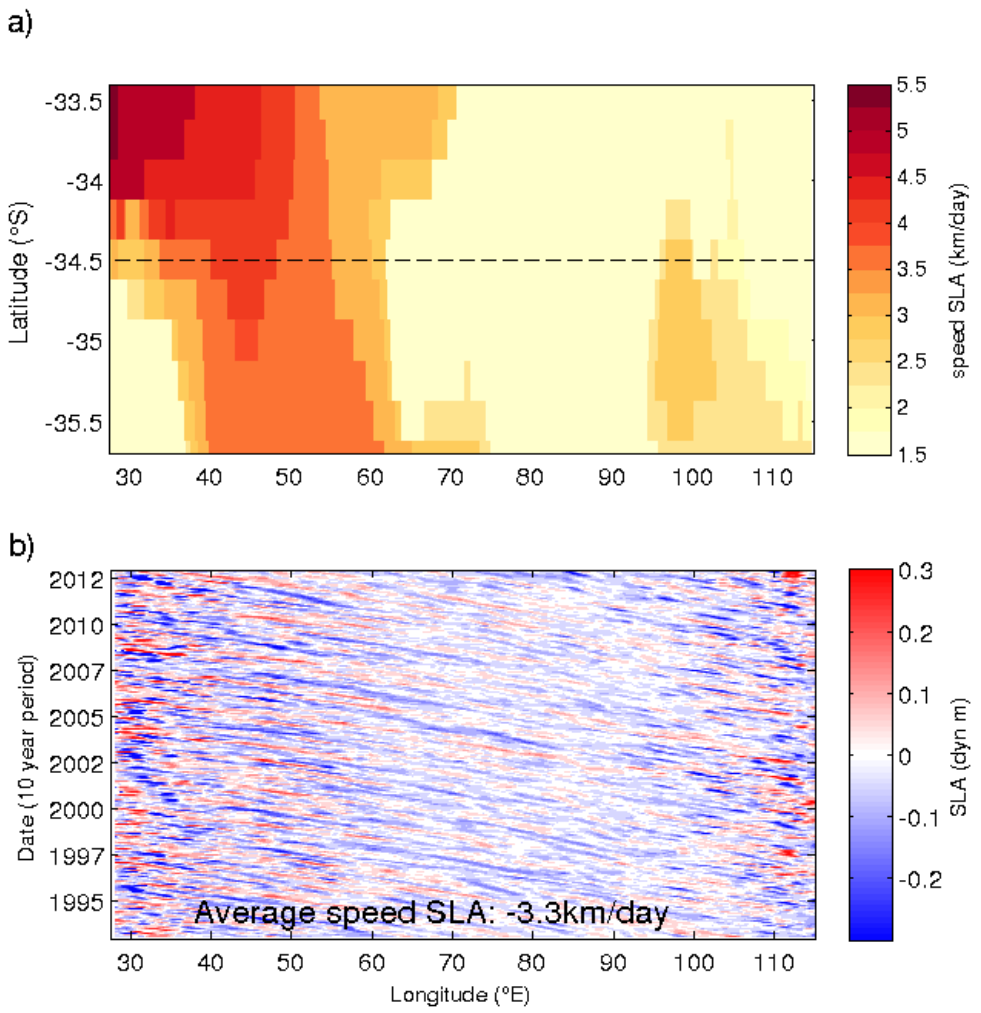

Figure 5.8: *a) Plot showing the results from the 2D Radon Transform ($km.day^{-1}$) executed on SLA data across the Southern Indian Ocean within the latitude range of the ACT line. A 15° longitude window was used. b) Hovmöller plot showing the propagation of Sea Level Anomalies (SLA; m) across the Southern Indian Ocean at the mean latitude of the ACT line (34.5°S; location marked as a dotted line in sub-plot (a)). The mean propagation speed calculated using a Radon Transform is quoted at the base of the plot.*

The average propagation speed of SLA at the mean latitude of the ACT line (34.5°S) is 3.3 $km.day^{-1}$. A Hovmöller plot showing the propagation of SLA across the Indian Ocean at 34.5°S is shown in Figure 5.8b. The magnitude of SLA is greatest at the boundaries,

where there is also an increase in the frequency of anomalies. Propagation of anomalies can clearly be seen, with some coherent signal communication over 20° or more longitude. The mean speed of 3.3 $km.day^{-1}$ is faster than that predicted by linear theory. Chelton et al. (1998) showed that the mean first baroclinic radius of deformation at the latitude of the ACT line is around 35km (Chapter 2 Figure 2.6). This gives a theoretical phase speed of first baroclinic mode waves of 2 $km.day^{-1}$ (Equation 16). Chapter 2 Section 2.6 explains why observed propagation speeds of baroclinic waves are faster than predicted by linear theory. In summary, the most likely explanation for this discrepancy is that the theory is only appropriate for an ocean basin of uniform depth where there is zero background flow (Killworth et al., 1997).

5.5 Summary and Discussion

A comparison of WSC atlases revealed that while there is generally good agreement between QuikSCAT, ERA, and NCEP-NCAR, only QuikSCAT can resolve potentially important small-scale patterns in WSC near the boundaries. Seasonal variability accounts for about 12% of the variance of winds over the Southern Indian Ocean (Figure 5.5). The pattern of seasonal WSC anomaly changes sign from the region of the trades to the Westerlies, with the transition between these regimes coinciding with the latitude of the ACT line. Furthermore, the divide between the two differing wind seasonality zones is not zonally uniform, implying that at the latitude of the ACT line there is not a coherent zonal seasonal strengthening/weakening of WSC. For example, although the zonal mean WSC is larger in winter than in summer (Figure 5.6 a versus c), close to the boundaries the seasonal cycle of WSC is opposite, suggesting a possible role for near-field winds in the seasonal cycle of the Agulhas Current.

The seasonal cycle of implied Sverdrup transport at the ACT line is opposite in phasing to that of the ACT proxy timeseries, indicating that, as expected, there is not an instantaneous adjustment of the western boundary to wind forcing across the basin. A Radon Transform revealed that Rossby waves varied in propagation speed across the basin, largely as a function

of pyncocline depth, with SLA travelling very slowly in the center of the basin and speeding up to a maximum of 5 $km.day^{-1}$ close to the western boundary. The mean propagation speed of anomalies across the Southern Indian Ocean at the latitude of the ACT line is 3.3 $km.day^{-1}$, meaning that it would take approximately 6.6 years for a Rossby wave to cross the basin.

5.6 Conclusion

Results presented here show that Sverdrup theory cannot be used to explain the observed seasonality of AC volume transport. Instead, the implication is that slow baroclinic Rossby waves may carry a large component of the seasonal wind stress signal to the western boundary, causing a lag in the phasing between the interior of the Southern Indian Ocean and the AC. Furthermore, the east and west portions of the Southern Indian Ocean at the latitude of the ACT line have opposing WSC seasonality, adding more complexity to the picture. The respective influences of barotropic versus baroclinic adjustment and of near- versus far-field winds on the seasonal variability of the AC have yet to be determined.

6 Barotropic Adjustment to Indian Ocean winds

6.1 Introduction

Historic model studies suggest that the seasonal adjustment of the Agulhas Current (AC) is achieved by barotropic waves (Matano et al., 2002, 2008). However, Chapter 5 showed that a simple barotropic adjustment to integrated wind stress curl (WSC) forcing across a flat-bottomed ocean basin cannot explain the seasonal cycle of the AC. To explore what role barotropic waves play in determining the seasonality of the AC, taking into account realistic topography, a barotropic single layer wind driven model is constructed for the Southern Indian Ocean. The seasonal cycle of simulated AC transport at the location of the Agulhas Current Time-series experiment (ACT) is then compared with that observed by the 23-year proxy (Beal and Elipot, 2016). This chapter aims to explore the barotropic adjustment of the Southern Indian Ocean to climatological wind forcing, and the contribution of this barotropic response to the seasonal cycle of the AC.

6.2 Key Question

How does a barotropic adjustment to wind forcing contribute to the observed seasonality of the Agulhas Current?

6.3 Data and Methods

6.3.1 Barotropic Shallow Water Model

The barotropic solutions of Navier-Stokes Momentum equations for a homogeneous layer of fluid, forced by surface wind stress and flowing over topography of a varying altitude are as follows:

$$\frac{\partial U}{\partial t} = fV - gH\left(\frac{\partial \eta}{\partial x}\right) + (\tau_w - \tau_b)_x + A_h\nabla^2 U - \frac{\partial}{\partial x}\left(\frac{U^2}{H}\right) - \frac{\partial}{\partial y}\left(\frac{UV}{H}\right) \qquad (18)$$

$$\frac{\partial V}{\partial t} = -fU - gH\left(\frac{\partial \eta}{\partial y}\right) + (\tau_w - \tau_b)_y + A_h \nabla^2 V - \frac{\partial}{\partial x}\left(\frac{UV}{H}\right) - \frac{\partial}{\partial y}\left(\frac{V^2}{H}\right) \tag{19}$$

where U and V are mass transports given by:

$$U = \int_H^0 \rho u dz = \rho H u \tag{20}$$

$$V = \int_H^0 \rho v dz = \rho H v \tag{21}$$

H is the height of the water column (depth of bathymetry) and η describes the height anomaly of the surface of the ocean. τ_{wx} and τ_{wy} are the components of wind stress in an eastward and northward direction, respectively. τ_{bx} and τ_{by} are bottom stresses (friction) in the east-west and north-south direction, respectively. A_h is the coefficient describing horizontal friction (viscosity). The system is said to be 'shallow' as the horizontal scale is much larger than the vertical scale, and therefore horizontal velocities are far greater than vertical velocities. This shallow layer of fluid flows over topography that varies in elevation, thereby changing the height of the water column, and inducing horizontal currents. A graphical representation of the vertical set-up of this model can be seen in Figure 6.1.

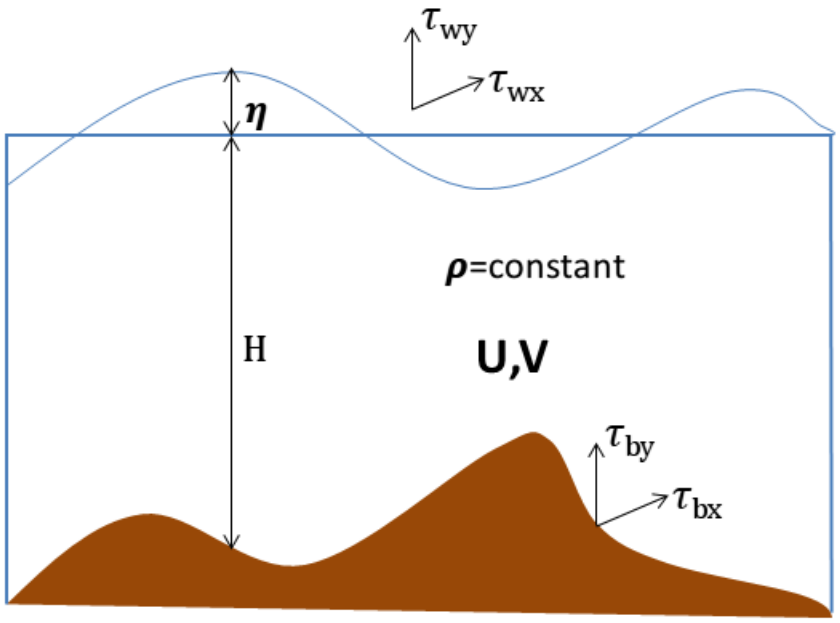

Figure 6.1: *Schematic of a barotropic wind driven model set-up*

6.3.2 Regional Ocean Modelling System - Barotropic Solution

The Regional Ocean Modelling System (ROMS) is a four dimensional free surface, terrain-following coordinate realistic ocean model (Shchepetkin and McWilliams, 2005). ROMS solves the barotropic and baroclinic components of the primitive equations separately using a mode 'time-split' technique. It is common practice in ocean modelling to split the fast and slow motions into barotropic and baroclinic sub-systems. The slowly varying baroclinic processes are solved at longer time steps and the rapidly adjusting barotropic processes are solved at shorter time steps.

The baroclinic sub-system is solved in three-dimensions, as each variable is solved for each depth layer, at every point in space. The barotropic subsystem, on the other hand, can be seen as a two-dimensional system as the variables are integrated over the entire depth of the water column to give one value for the single layer (Figure 6.1). This means that the barotropic component can be solved in two dimensions using simplified versions of the

primitive equations (Equations 18 and 19).

Here, the ROMS framework is used as a platform to run a simple wind driven single layer barotropic model. The grid size is 1/3° (31.5 km), and the domain is limited to the Southern Indian Ocean (5°S - 50°S, 19°E - 119°E). The boundaries are closed and no-slip with a strong nudging coefficient. The model is only forced with climatological winds - there are no thermohaline processes. The model is run for 40 years and the first 14 years are discarded as this is the spin-up time needed to reach a stable solution. A list of the experimental parameters for the barotropic model and their values are provided in Table 1.

Barotropic Model Parameters	Value
zonal domain extent (x)	19°E - 119°E
meridional domain extent (y)	5°S - 50°S
grid resolution resolution (dx;dy)	1/3° (31.5 km)
temporal resolution (dt)	1 minute
time-step of solution	1 month average
run duration	40 years
horizontal friction (Ah)	500 $m^2 s^{-1}$
bottom drag (r)	3×10^{-4} $m.s^{-1}$

Table 1: Experimental parameters and their respective values for the barotropic model run using the Regional Ocean Modelling System (ROMS) framework.

6.3.3 Topographic Sverdrup Relation

Barotropic Rossby waves are driven purely by variations in sea surface height (SSH). As described earlier, these waves have no vertical shear and thus the water can be imagined as moving at a uniform speed at all depths (Talley, 2011). The barotropic response of the ocean to wind forcing is thus strongly modified and guided by the topography of the ocean floor (Anderson and Corry, 1985). The Sverdrup Balance (Equation 1) assumed a flat bottom. Barotropic waves are, however, sensitive to topography and so a Topographic

Sverdup equation is needed. The full derivation of the Topographic Sverdrup Relation can be found in the Appendix Section 12.2.3, and the final equation describing the barotropic adjustment to wind forcing is given as:

$$\beta V - \frac{f}{H}\left(\overrightarrow{U}.\overrightarrow{\nabla}H\right) = \left(\vec{\nabla}\times\vec{\tau}\right) + \frac{1}{H}\left(\tau^x\frac{\partial H}{\partial y} - \tau^y\frac{\partial H}{\partial x}\right) \tag{22}$$

Which then simplifies (see Appendix Section 12.2.3 for full derivation) to:

$$\overrightarrow{U}.\overrightarrow{\nabla}\left(\frac{f}{H}\right) = \overrightarrow{\nabla}\times\left(\frac{\tau}{H}\right) \tag{23}$$

This equation is appropriate for a homogenous layer of variable depth H and describes the process whereby mass transport, ($\vec{U} = \rho \mathrm{H}\vec{u}$) is driven across f/H contours by the curl of wind stress over water column depth ($\frac{\tau}{H}$). Furthermore, wind blowing over a gradient in topography (second term on right hand side of Equation 22) can drive flow across contours of f/H even if there is no WSC.

Koblinsky (1990) constructed global maps of values of f/H and found that from 20°N to 20°S the barotropic response of the ocean resembles that of a flat bottom Sverdrup regime. In the mid-latitudes, however, the response was found to be weak, quasi-stationary, and along isolines of f/H. Both Gill and Niller (1973) and Anderson and Corry (1985) suggested that the flat-bottom Sverdrup relation is unlikely to hold on seasonal timescales and that the variation in bottom topography plays an important role and must therefore be taken into account.

6.3.4 ETOPO2 Bathymetry

It is essential that the barotropic wind driven shallow-water model possesses realistic bathymetry as changes in water column height due to bathymetric features strongly influence the path of a barotropic wave (Equation 23). The bathymetry used is ETOPO2, a two arc minute ocean-floor elevation data set (ETOPO2, 2006), which is smoothed to the grid resolution of the model (1/3°). The model bathymetry is shown in Figure 6.2 with the major features labelled.

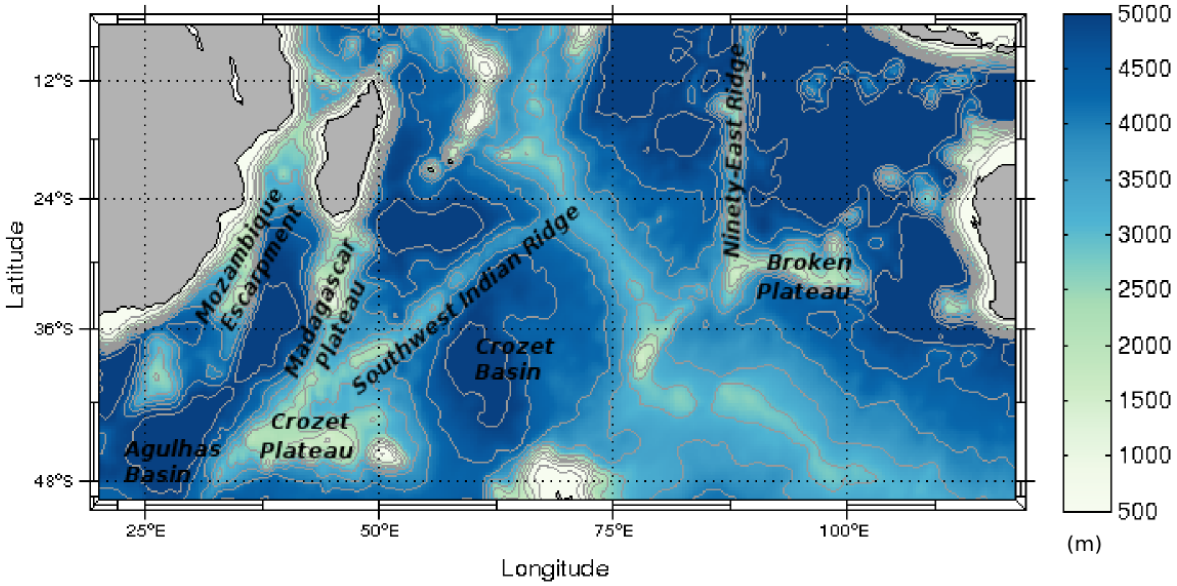

Figure 6.2: *Bathymetry (m) of barotropic shallow water model. Contours show intervals of 500m from the surface down to 5km depth. The major features are labelled.*

A map of f/H for the Southern Indian Ocean derived from ETOPO2 bathymetry can be seen in Figure 6.3. In regions where there are few bathymetric features, such as the tropical Indian Ocean, the barotropic signal can travel westwards across the basin unimpeded by changes in H, as found by Koblinsky (1990). However, in the southern portion of the basin, bathymetric barriers such as the Southwest Indian Ocean Ridge, the Madagascar Plateau, and the Mozambique Plateau may block the western boundary from receiving incoming signals from the eastern portion of the basin, as suggested by Matano et al. (2002). To drive mass transport across these contours of f/H, there must be a curl of wind stress over water column depth (Equation 23). In the absence of an input of vorticity, the flow will be parallel to f/H contours.

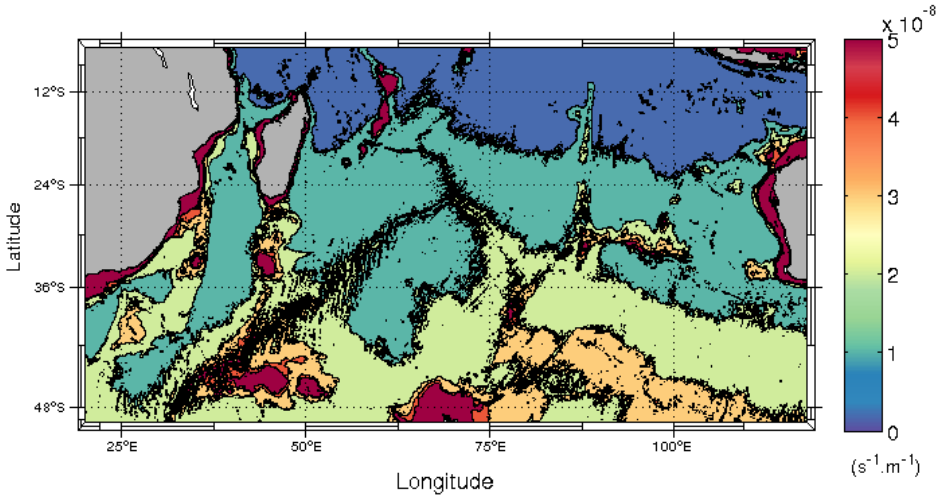

Figure 6.3: *Map of f/H contours for the Southern Indian Ocean. ETOPO2 dataset used to inform bathymetry.*

6.3.5 Climatological Winds

The wind product used to force the barotropic model is a wind stress climatology from the NASA Quick Scatterometer (QuikSCAT) which measured winds near the ocean surface from July 1999 to November 2009 at a 1/4° resolution (Risien and Chelton, 2008). The seasonal cycle is the focus of the research presented here, and thus climatological means were deemed appropriate for this study. For more information on the a comparison of the QuikSCAT climatology with NCEP-NCAR and ERA monthly mean winds, please see Chapter 5 Section 5.4.1.

6.4 Results

6.4.1 Mean circulation of the Barotropic Model

The mean circulation of the barotropic single layer model is shown in Figure 6.4. Two distinct differences between the model's mean circulation and reality are immediately evident. The first is the absence of the Southern Indian Ocean gyre. In its place are smaller sub-gyres,

strongly delineated by bathymetry. The second is that the main western boundary current in this single layer model does not flow along the South African continental slope. Instead, it follows the Mozambique Escarpment and continues directly south to the Agulhas Basin (Figure 6.4). A comparatively weak flow is evident at the actual location of the AC along the continental slope. The majority of the barotropic signal is prevented from reaching the South African coastline due to bathymetric blocking. A comparison of the mean circulation of Figure 6.4 with the map of f/H values shown in Figure 6.3, reveals that the mean flow pattern is largely parallel to isolines of f/H. In certain areas where there are closed contours of f/H, such as around the Crozet Basin (55°E - 75°E; 25°S - 45°S), a semi-isolated closed gyre exists.

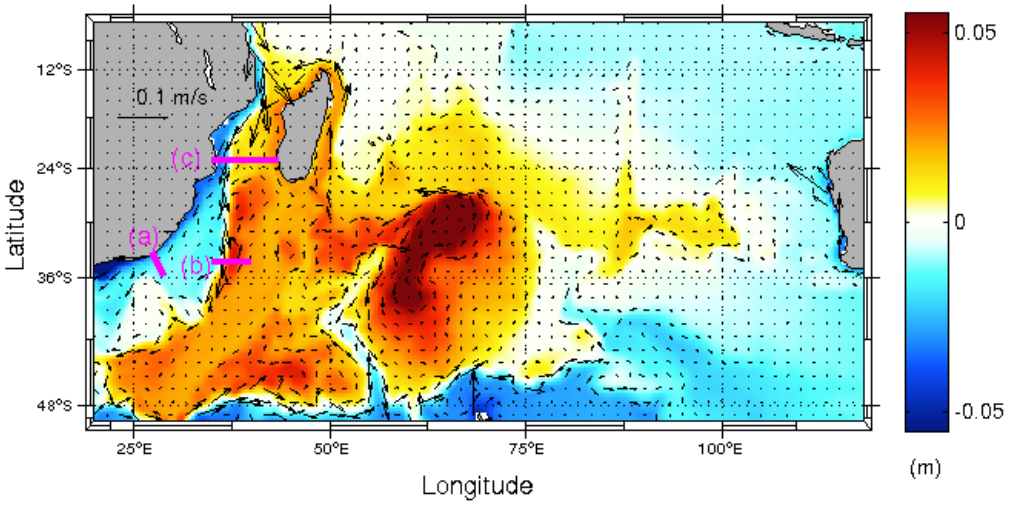

Figure 6.4: *Time mean sea surface height (m) of the barotropic model as background shading with vectors of mean circulation (m/s) overlaid. Location of cross sections mentioned in Section 6.4.2 are shown in magenta.*

6.4.2 Seasonality in the Barotropic Model

Figure 6.5 shows the seasonal anomalies from the mean circulation. In spring and summer the eastern portion of the basin experiences a positive anomaly in sea surface height (SSH) along with the area inshore of the continental shelf at the western boundary (Figure 6.5 a and

d). During these seasons, the western circulation gyres possess a negative SSH, resulting in a northward anomaly in transport of both the simulated barotropic western boundary current and the flow at the location of the ACT line. The opposite is true for autumn and winter where positive SSH anomalies in the western gyre and negative anomalies in the in-shore region of the western boundary result in a southward anomaly in flow at the ACT line and the main western boundary current (Figure 6.5 b and c). The agreement in sign of anomalies along the eastern and western boundaries for all seasons indicates that some form of basin-wide resonance is present.

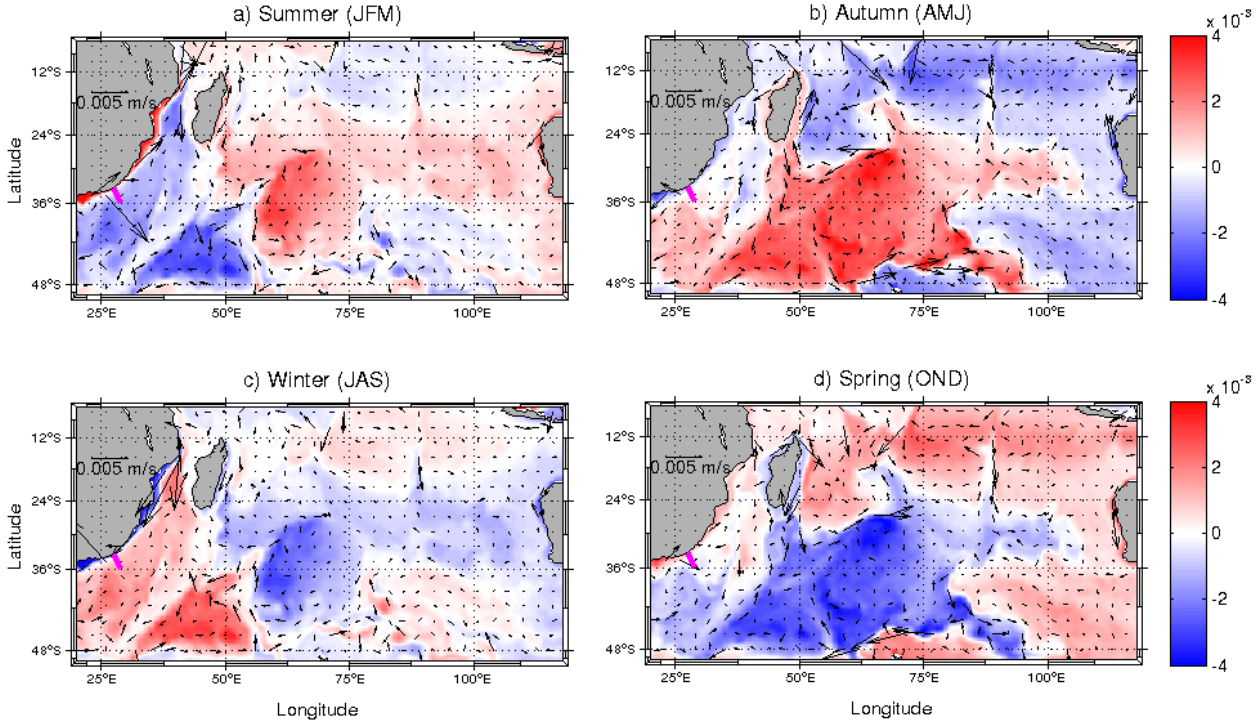

Figure 6.5: *Maps showing seasonal anomaly in sea surface height (m) of barotropic model as background shading with vectors of anomalies from mean circulation ($m.s^{-1}$) overlaid for a) Summer, b) Autumn, c) Winter, and d) Spring.*

In order to compare the seasonality of the model's simulated flow at the location of the ACT line to that observed by the ACT transport proxy, the transport must be calculated in the same way as was done by Beal et al. (2015) for the boundary layer (Tbox). To do so

an imaginary ACT line is placed in the model, and the mean position of the zero velocity isotach is found to be located 247 km from the coast. The net transport perpendicular to the line, integrated out to 247 km, is obtained for each month and the resultant seasonal cycle of the flow is shown in Figure 6.6a. The maximum transport is in July (winter) and the minimum falls in January-February (summer). This seasonality is opposite to the 23-year transport proxy (Beal and Elipot, 2016) (Figure 4.4), and the mean transport of the current is much smaller than reality at -4.75 Sv. The reduced volume of flow on the continental shelf is due to the fact that the main western boundary current is much farther offshore in this barotropic model, flowing along the Mozambique Escarpment with a mean transport of 17.1 Sv. The seasonal variability of this simulated western boundary current was investigated at 34.5°S between 35°E and 40°E (section shown in Figure 6.4 marked (b)), and found to be at a maximum in October and a minimum in April (Figure 6.6b). Further investigation of this seasonality showed that it is highly dependent on latitude, possibly due to the influence of recirculation and input of water south of Madagascar.

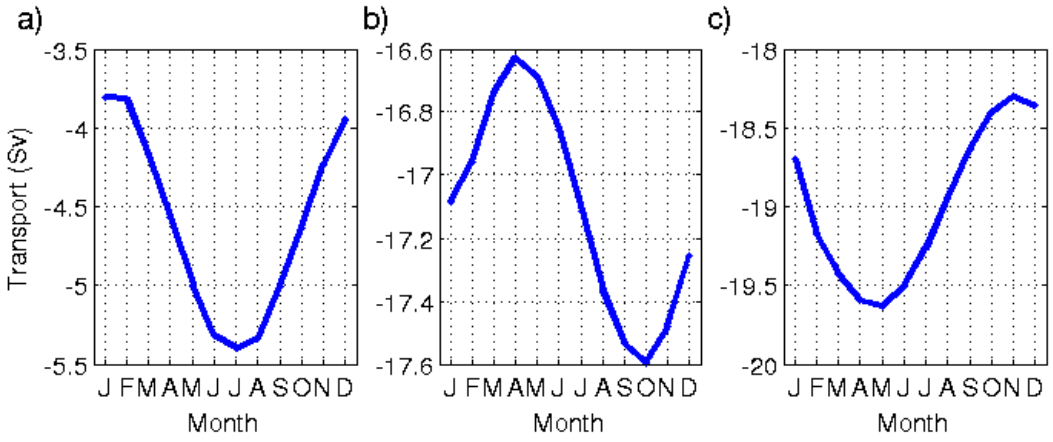

Figure 6.6: *Seasonal cycle in transport at (a) the location of the Agulhas Current Time-series array, b) a transect through the detached western boundary current, and (c) a transect of the Mozambique Channel at 23°S in the barotropic model. The flow is southward, therefore more negative values equate to a stronger current.*

Biastoch et al. (1999) proposed that the AC's seasonality was advected from the Mozambique Channel with a delay of approximately two to three months. *In-situ* measurements at the narrowest section of the Mozambique Channel reported a winter maximum in flow (Ridderinkhof et al., 2010). To investigate whether signal advection from the Mozambique Channel is a dominant process for the seasonality downstream in the barotropic model, the seasonal variability of the transport at 23°S (transect shown in Figure 6.4) is calculated and presented in Figure 6.6c. The transport through the Channel is at a maximum in May and minimum in November, two months ahead of the seasonal cycle at the ACT line. This seasonality is similar to that presented by Biastoch et al. (1999) (Figure 2.11). The magnitude of flow through the Mozambique Channel is on average 14.5 Sv larger than that at the ACT line, indicating that only a small portion of water from the Channel flows along the continental shelf (actual AC region), the majority follows the Mozambique Escarpment.

6.5 Summary and Discussion

This chapter investigated the seasonal response of the Southern Indian Ocean to climatological QuikSCAT winds using a barotropic model with realistic topography. Past model studies simulating the Southern Indian Ocean have suggested that the adjustment to seasonal wind changes is achieved by barotropic waves (Matano et al., 2002). Model studies also claimed that the seasonality of the AC is linked to that of the Mozambique Channel, and predicted a winter-spring maximum in AC transport (Biastoch et al., 1999). *In-situ* mooring data from the Agulhas Current Time-series (ACT) experiment (Beal et al., 2015) and the subsequent 23-year transport proxy (Beal and Elipot, 2016) showed that the AC is strongest in summertime, thereby revealing a disagreement between historic models and recent observations.

To investigate the role of a barotropic adjustment to climatological winds in determining the AC's seasonality, a single layer shallow water model is run using the ROMS framework as a platform. This barotropic model possesses realistic bathymetry and is forced by climatological QuikSCAT winds. The barotropic circulation of the Southern Indian Ocean is

found to be strongly influenced by bathymetry, with the flow largely following contours of f/H (Figure 6.4). This results in subgyres forming and the main western boundary current in the simulation does not follow the South African continental slope, but instead is diverted offshore to flow southwards along the Mozambique Escarpment.

The barotropic model simulated a wintertime (July) maximum in transport at the location of the ACT line (Figure 6.6a).

6.6 Conclusion

The barotropic contribution to AC seasonality is shown to be small. The seasonality of flow at the location of the ACT line in the barotropic model disagrees with observations of the AC seasonal cycle. The results from the barotropic simulation are, however, similar to previous ocean general circulation model studies (Matano et al., 2002; Biastoch et al., 1999), showing an AC seasonality linked to a southward propagation of seasonal signals from the Mozambique Channel, while signals directly from the east are blocked by topography. Topographic blocking is extreme in the barotropic model, with the majority of the western boundary flow diverted to the east of the Mozambique Ridge. In previous ocean general circulation model studies topographic smoothing of the Mozambique Ridge may have allowed for a greater penetration of the barotropic signal onto the South African continental shelf, thus strengthening the reported seasonal winter-spring increase in AC flow (Biastoch et al., 1999; Matano et al., 1999, 2002).

7 First Baroclinic Mode Adjustment to Indian Ocean Winds

7.1 Introduction

Wind driven ocean circulation theory suggests that barotropic and first baroclinic waves communicate the majority of the effects of wind stress curl (WSC) variability within the ocean (Anderson and Corry, 1985; Killworth et al., 1997). Results from the single layer model presented in Chapter 6 indicated that a barotropic adjustment to climatological winds cannot explain the observed seasonality of the Agulhas Current (AC). Moving beyond the simplest case of a barotropic model, the next step in complexity is to investigate the first baroclinic mode adjustment to wind forcing and its contribution to the seasonality of the AC. To do so, a one-and-a-half (1 ½) layer reduced gravity model is built using the Regional Ocean Modelling System (ROMS) as a platform to solve the shallow water equations. The seasonality of the simulated AC at the position of the Agulhas Current Time-series (ACT) line is described in Section 7.4. This chapter aims to investigate whether the first baroclinic mode adjustment of the Southern Indian Ocean to climatological wind forcing can explain the observed seasonal phasing of the AC volume transport. The buoyancy driven thermohaline overturning and the Indonesian Throughflow (ITF) are not simulated by the model. We assume that these features are secondary for the investigation into AC seasonality at 34.5°S.

7.2 Key Question

How is the seasonality of the Agulhas Current influenced by a first baroclinic mode adjustment to climatological Indian Ocean winds?

7.3 Data and Methods

7.3.1 1 1/2 Layer Reduced Gravity Set-up using ROMS Framework

As explained in detail in Chapter 6, Section 6.3.2, ROMS solves the barotropic and baroclinic sub-systems separately using a 'time splitting' technique. This division of the two modes for computations can be utilized to create a shallow water reduced gravity set-up using only the ROMS barotropic time-split solution. The baroclinic solution to the primitive equations is computationally costly as it solves the parameters for multiple depths (three dimensions). The barotropic solution, on the other hand, is computationally cost-efficient as the variables are solved in only two dimensions, for one layer in space (and time). The single active layer is maintained, but in the reduced gravity set-up, instead of having bathymetry determining the water column depth, the depth of the active layer is replaced by an interface dividing the top layer from a bottom inactive later. The interface between these two layers can be thought of as the thermocline or pycnocline (even though the reduced gravity model does not simulate the thermohaline properties of the ocean), as it represents a step function in density and divides an active surface layer from a deep stationary layer. The model is spun up from an initial pycnocline depth with heaving of the interface, and hence changes in thickness of the upper layer, driven by wind stress at the surface. The geographical boundaries of the model are the same as that of the barotropic model in the previous chapter, [-5S -50S; 19E 119E], and they are closed with no-slip conditions. The model is run for 50 years, and the first 14 years of solution are discarded as this is the stabilization time.

Figure 7.1 is a schematic of the reduced gravity model set-up. A frictional coefficient, r, is applied to the interface between the upper active layer and the lower layer (Table 2). Gravity, $g = 9.8\ m.s^{-2}$, is replaced by reduced gravity (g') which is dependent on the density gradient between the two layers:

$$g' = \left(\frac{\rho_2 - \rho_1}{\rho_2}\right) g \tag{24}$$

Where ρ_1 is the constant density of the upper layer, ρ_2 is the constant density of the lower layer.

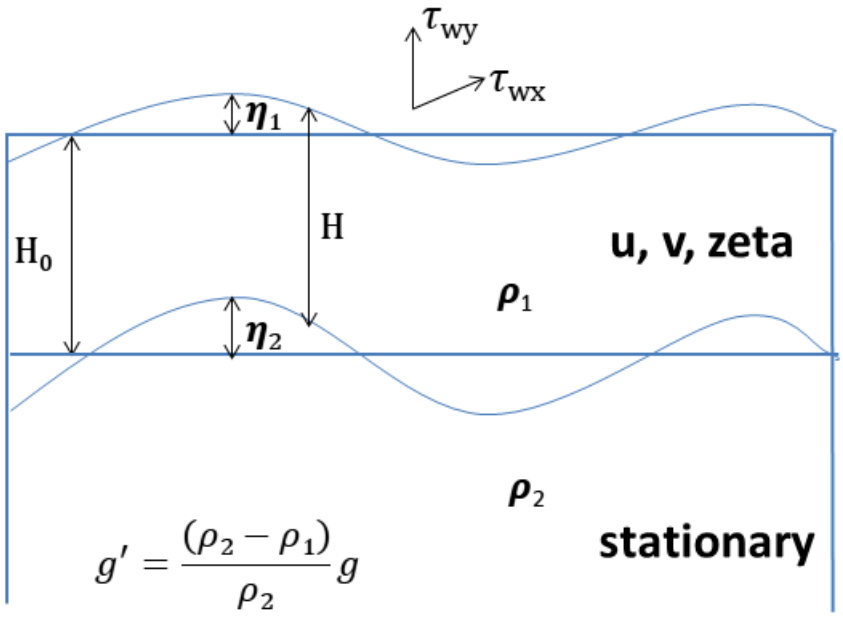

Figure 7.1: *Schematic of the 1 ½ layer reduced gravity wind driven model set-up using the ROMS framework*

To use the ROMS framework for this purpose, the model is instructed to only solve the two dimensional shallow water equations. H, which is usually the thickness of the water column from the surface to the depth of the bathymetry, is replaced by H_o, the thickness of the upper layer from the surface to the initial pycnocline depth, and g is replaced by g'. The model is forced with QuikSCAT climatological winds (see Chapter 5, Section 5.3.1 for description of product). This simulation is computationally highly efficient and suitable for resolving the response of the active layer to wind stress curl forcing. The simplified Navier-Stokes Momentum equations for a reduced gravity model are:

$$\frac{Du}{Dt} = fv - g'\frac{\partial H}{\partial x} + \frac{\tau_{xw}}{H\rho_1} + A_h\nabla^2 u - \left(\frac{r_o u}{H}\right) \tag{25}$$

$$\frac{Dv}{Dt} = -fu - g'\frac{\partial H}{\partial y} + \frac{\tau_{yw}}{H\rho_1} + A_h\nabla^2 v - \left(\frac{r_o v}{H}\right) \tag{26}$$

where u and v represent the vertically averaged flow of the upper active layer (layer 1) in zonal and meridional directions, respectively, and τ_{xw} and τ_{yw} are the easterly and northerly components of the surface wind stress. It is assumed that the stresses at the layer interface are proportional to the velocity of the active layer and so the Rayleigh damping term, $-r_o\vec{u}/\mathrm{H}$ is introduced for vertical friction. Horizontal mixing is represented by an eddy diffusivity $A_h\nabla^2\vec{u}$.

After spin up, the reduced gravity model gives parameters, u,v and *zeta* at each time step, where *zeta* is the anomaly in layer thickness $(H - H_0)$. Changes in *zeta* relate to alterations in sea surface height by:

$$\eta_1 = \left(\frac{\rho_2 - \rho_1}{\rho_1}\right) zeta \tag{27}$$

Table 2 shows the experimental parameters and their respective values for the reduced gravity model run using the ROMS framework.

Reduced Gravity Model Parameters	Value
zonal domain extent (x)	19°E - 119°E
meridional domain extent (y)	5°S - 50°S
grid resolution resolution (dx;dy)	1/3° (31.5 km)
temporal resolution (dt)	30 minutes
time-step of solution	1 month average
run duration	50 years
horizontal friction (Ah)	500 m^2s^{-1}
bottom drag (r_o)	3×10^{-4} $m.s^{-1}$
initial pycnocline depth (H_o)	800 m
reduced gravity (g')	first 0.0134 $m.s^{-1}$, then 0.0076 $m.s^{-1}$

Table 2: Experimental parameters and their respective values for a reduced gravity (first baroclinic mode) model run using the Regional Ocean Modelling System (ROMS) framework.

7.4 Results

7.4.1 Mean Circulation of the 1 ½ Layer Baroclinic Model

The mean circulation of the 1 ½ layer reduced gravity model is shown in Figure 7.2 as vectors overlaid on a background shading of sea surface height. To assess how well the modelled circulation represents the Southern Indian Ocean gyre, a comparison is made with the steric height maps of Ridgway (2007) computed from the CSIRO Atlas of Regional Seas (CARS) and included in the Appendix for convenience, Figure 12.4. The largest differences between the reduced gravity model (Figure 7.2) and the observed surface circulation (Figure 12.4a) result from the absence of an ITF in the model. The absence of the ITF in the model is not expected to impact the seasonal variability of the AC, as its seasonal cycle is around 4 Sv (Shinoda et al., 2012), and there is an advective time scale of 10-30 years between the ITF and the AC (Durgadoo et al., 2017).

Compared to the observed circulation integrated throughout the thermocline (Figure 12.4b), the model performs well as the single active layer is skilled at representing the whole thermocline. The model circulation adequately represents the main features of the Southern Indian Ocean with a simulated South Equatorial Current that crosses the basin at 18°S and bifurcates upon reaching Madagascar, the southern branch then flows along the east coast of Madagascar and travels directly westwards to the African coast to continue southwards in the main western boundary current of the model (Figure 7.2). This simulated western boundary current is in the same position as the AC in reality.

It is worth noting that the buoyancy driven thermohaline overturning is not included in the model, the model is purely wind driven and is highly idealized. Furthermore, the lack of a Southern Hemisphere supergyre means that the finer features of the Agulhas Retroflection and Agulhas Return Current are missing. We assume that these features are secondary for the investigation into AC seasonality at 34.5°S.

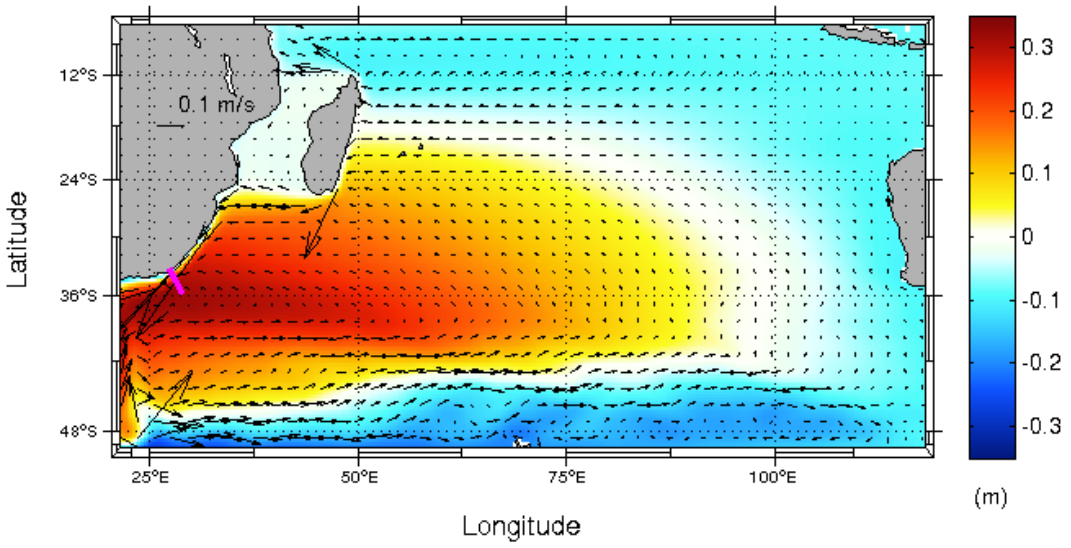

Figure 7.2: *Time mean sea surface height (m) from the 1 ½ layer reduced gravity model as background shading with vectors of mean circulation ($m.s^{-1}$) overlaid. The position of the ACT array is shown in magenta.*

7.4.2 Initialization with Realistic Pycnocline Depth

To calculate the seasonality of the simulated AC at the ACT line, the net transport perpendicular to the ACT line, from the coast out to the time-mean position of the zero velocity isotach (Beal et al., 2015), is obtained for each month. As mentioned in Section 7.3.1, the value of the reduced gravity parameter, g', and the initial depth of the active layer from which the model spins up, H_o, must be overwritten in the initialization stage of the model run. The model restricts initialization to the same pycnocline depth and reduced gravity everywhere. To inform a realistic pycnocline depth, density profiles for the Southern Indian Ocean for the latitude range of the ACT line were obtained from the World Ocean Circulation Experiment (WOCE) (Clarke, 1992). Appendix Figure 12.5 shows a cross section of density of the Southern Indian Ocean averaged over the latitude range of the ACT line. The density gradients were computed and the steepest change in density below 400 m identified

as the pycnocline depth. Data above 400 m were excluded as high density gradients in this area can be related to the shallower seasonal pycnocline. The mean pycnocline depth was found to be 800 m, with a mean density of the upper layer of $\rho_1 = 1026.2\ kg.m^{-3}$ and a mean density of the lower layer of $\rho_2 = 1027.6\ kg.m^{-3}$.

The corresponding reduced gravity parameter is thus:

$$g' = \left(\frac{\rho_2 - \rho_1}{\rho_2}\right) g = \left(\frac{1027.6 - 1026.2}{1027.6}\right) 9.82 = 0.0134 m.s^{-2}$$

The reduced gravity model was consequently initialized with the 'realistic' parameters of H_0=800 m and $g' = 0.0134\ m.s^{-1}$. The simulated flow at the location of the ACT array has a mean speed of -0.23 $m.s^{-1}$ and a maximum speed of -0.61 $m.s^{-1}$. The boundary layer flow is on average 295 km wide (from the shore to the time-mean position of the zero velocity isotach) and 915 m deep. The velocities of the simulated AC are slightly slower than those observed by the ACT *in-situ* measurements, as the observed mean speed of the upper 915 m of the AC is -0.28 $m.s^{-1}$, and the maximum speed of this layer is -1.02 $m.s^{-1}$. Furthermore, the boundary layer of the AC is broader in the simulation compared to the mean width of 219 km reported from the ACT measurements. Figure 7.3 shows the time-average thickness of the wind driven layer for this simulation and the resultant Rossby radius of deformation calculated from Equation 15.

The parameters chosen for initialization set the Rossby radius of deformation, which in turn influences the speed of Rossby wave propagation. The radius of deformation from the simulation initialized with 'realistic' parameters is 45 km at the ACT line. This is 10 km larger than the $\pm$ 35 km observed in the AC area by Chelton et al. (1998) (Chapter 2, Figure 2.6).

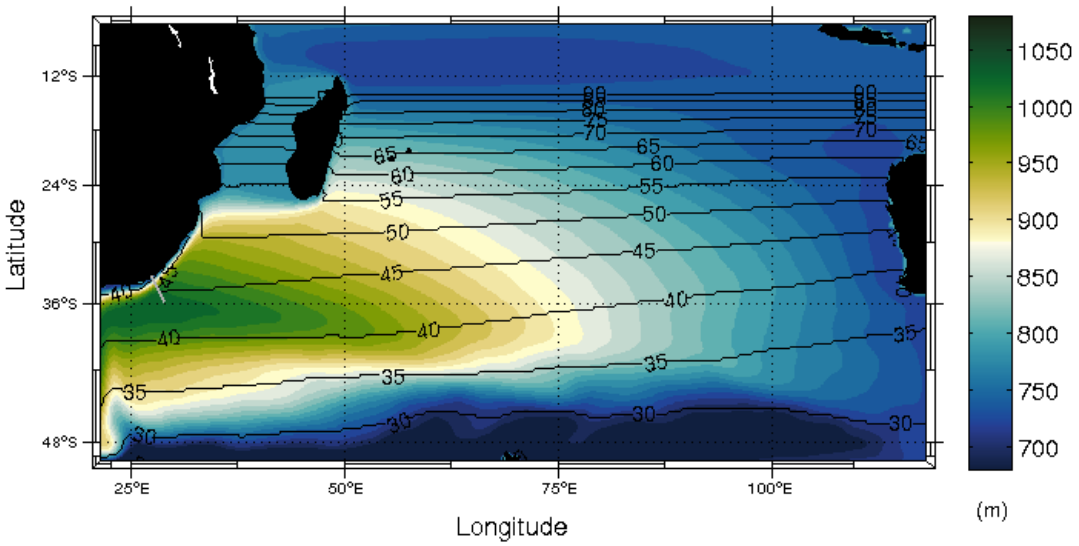

Figure 7.3: *Average depth of wind driven layer (m) for reduced gravity model initialized with* $H_0 = 800\ m$ *and* $g' = 0.0134\ m.s^{-2}$. *Contours showing the corresponding Rossby radius of deformation (km) are overlaid at intervals of 5km from 10km to 90km. Position of an artificial ACT line is overlaid in grey.*

Using this 'realistic' model set-up, the seasonality of the AC boundary layer transport from the model is at a maximum in November and at a minimum in June (Figure 7.4a). This seasonal phasing does not match that observed, as the maximum in flow occurs 3 months earlier in the simulation (Figure 7.4a). The amplitude of seasonal changes is 3.5 Sv, 8% of the total transport. This is small compared to the 22 Sv, 25% of the total transport, seasonal change in boundary layer transport recorded by the proxy time-series during QuikSCAT operation (Figure 7.9).

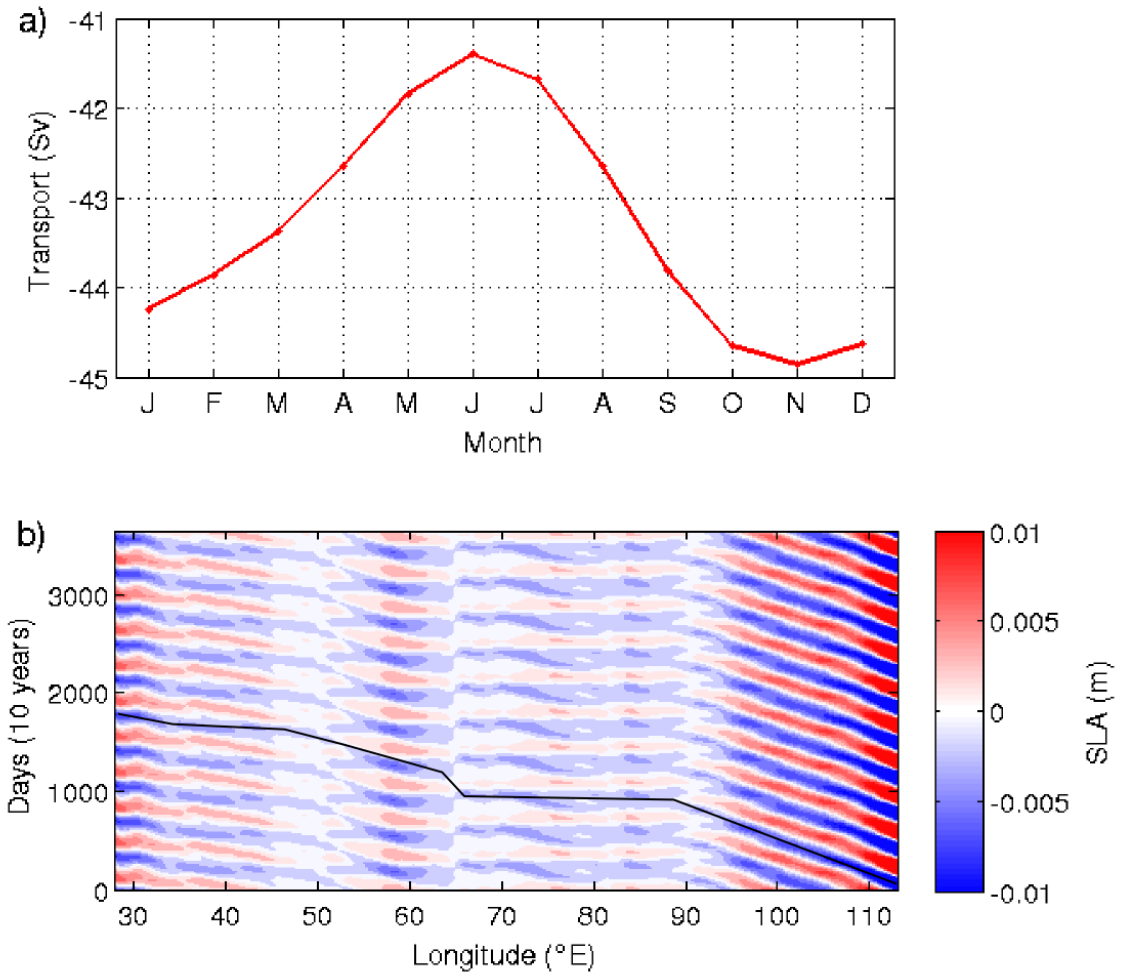

Figure 7.4: *a) Seasonal cycle of Agulhas Current transport (Sv) in model simulation initiated with a pycnocline depth of 800 m and* $g' = 0.0134\ m.s^{-2}$. *The flow is south-westward, therefore more negative values correspond to a stronger current. b) Hovmöller plot showing the propagation of sea level anomalies (m) across the basin at the mean latitude of the ACT line (34.5°S) during the final 10 years of the simulation. The black line tracks the propagation of an anomaly across the basin in order to estimate the average phase speed.*

To understand more about the origin and phasing of the simulated seasonal cycle, the propagation of anomalies across the Southern Indian Ocean at the latitude of the ACT line is investigated (Figure 7.4b). Signals initiated at the eastern boundary propagate for two

years to 90°E, then die out due to destructive interference as they encounter a WSC anomaly of the opposite sign to that which initiated them (see map showing EOF of seasonal WSC in Appendix, Figure **??**). From around 90°E to 65°E, the reduced gravity ocean appears to respond instantaneously to local WSC curl forcing, thereby giving the impression that the waves are travelling extremely fast (Figure 7.4b). Figure **??** in the Appendix showing the first EOF of the seasonal component of QuikSCAT winds reveals that within this longitude range (90°E to 65°E), at the latitude of the ACT line (33.3°S to 35.7°S), there is little seasonal variability in the WSC, thereby accounting for the small amplitude anomalies in the hovmöller (Figure 7.4b). West of 45°E, a coherent propagation of SSH anomalies can be seen. The breaks in propagation of SLAs across the basin (hovmöller of Figure 7.4b) could be interpreted as being associated with changes in WSC. The reduced gravity model by construction does not have topography as the bottom layer is infinitely deep. The changes in propagation speed can therefore not be explained by interaction with ocean ridges, leaving destructive interference with overlying WSC Ekman pumping and suction as the most likely explanation for the observed dissipation of anomalies (Figure 7.4b).

To approximate propagation speed, a negative anomaly initiated at the eastern boundary was tracked across the basin by eye (see black line overlaid on Figure 7.4b). A radon transform was not stable, due to the apparent infinite speeds observed mid-basin, and thus tracking by eye was used. On average, it takes an anomaly 1800 days to cross the 8040 km of the basin, equating to a mean propagation speed of 4.46 $km.day^{-1}$. This is approximately 1 $km.day^{-1}$ faster than that observed from Aviso (Figure 5.8b). Anomalies propagate at approximately 2.6 $km.day^{-1}$ near the eastern boundary, and 6.1 $km.day^{-1}$ near the western boundary. There is no evidence for a coherent transmission of these signals across the whole basin, suggesting that the anomalies arriving at the western boundary are from the near-field area west of 45°E.

The next sections will explore the sensitivity of the simulated AC seasonal cycle in the reduced gravity model to friction and to different initial reduced gravity parameters. In particular, the impacts of friction and propagation speed on the amplitude and phasing of

the simulated AC are considered so as to gain insight into what processes may be most important in the real ocean.

7.4.3 Influence of Friction on the Seasonal Cycle of the Simulated Agulhas Current

For stability reasons, a damping in the form of a linear frictional term (r_o) is present in the reduced gravity model (Equations 25 and 26). This frictional term can be seen as the drag that the upper layer experiences from its movement relative to the lower stationary layer. From a scaling analysis for a 1000m layer and a velocity of 0.1 $m.s^{-1}$, the frictional parameter used in the simulations ($r_o = 3 \times 10^{-4}\ m.s^{-1}$) is equivalent to a vertical turbulent eddy viscosity of 0.3 $m^{-2}.s^{-1}$. This is three to four orders of magnitude larger than reality. Munk (1966) reported a globally averaged diapycnal eddy diffusivity in the order of 10^{-4} $m^{-2}.s^{-1}$, and Gregg (1987) and Ledwell et al. (1998) showed that within the main pycnocline the eddy diffusivity is even smaller, of the order 10^{-5} $m^{-2}.s^{-1}$. The friction in the reduced gravity simulation is required to be large so as to stabilize the simulation and prevent an outcropping of the pycnocline at the eastern boundary. The trade-off is a dampening of circulation, resulting in a reduction in the amplitude of seasonal changes.

To investigate the effect of this frictional coefficient on the phasing of the simulated AC, the frictional parameter used in the initial run was reduced by an order of magnitude, to $3 \times 10^{-5}\ m.s^{-1}$. Figure 7.5 shows the seasonal cycle of the simulated AC in the reduced gravity model with the original friction as a solid red line, compared to the seasonal cycle in the reduced friction case plotted as a dotted line. The seasonal phasing is not altered by a decrease in friction, but the amplitude of seasonal changes increases by 60%, from 3.4 Sv to 8.4 Sv. Furthermore, the mean volume transport of the current is increased by 3 Sv in the low friction case. This indicates that a larger current and increased amplitude in seasonal AC transport changes in the simulation may be achieved by reducing the frictional coefficient. In the real ocean, friction is smaller, allowing for a larger amplitude seasonal cycle, however the reduced gravity model becomes unstable when friction is lowered - especially for lower

values of g' and H_0. In the following chapters, the original frictional parameter is maintained as high stability is needed in order to carry out the reduced gravity parameter sensitivity tests and wind property tests. Note that these tests are carried out with the knowledge that a decrease in friction does not affect the seasonal phasing of the AC, but does increase the amplitude of the seasonal cycle.

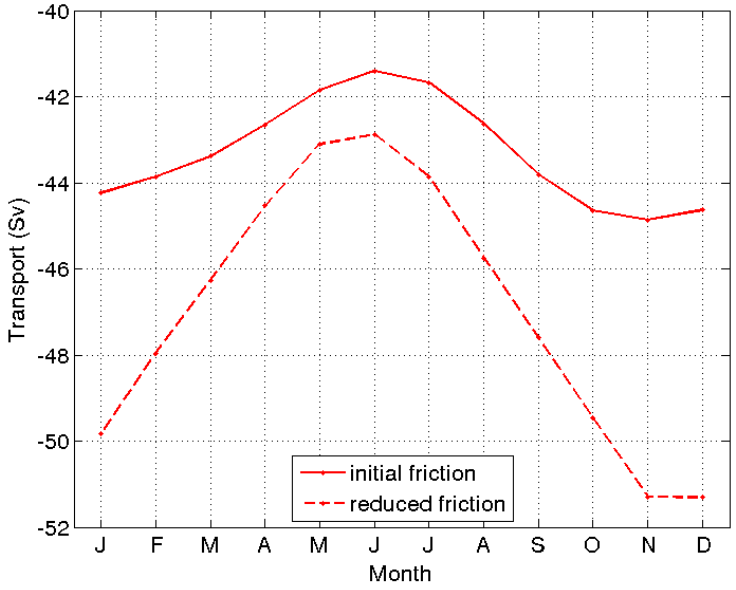

Figure 7.5: *Seasonal cycle of Agulhas Current transport (Sv) in model simulation with a) original frictional parameter of* 3×10^{-4} $m.s^{-1}$ *and b) friction reduced by an order of magnitude to* 3×10^{-5} $m.s^{-1}$. *'Realistic' parameters were used for initialization in both cases, namely* $H_0 = 800$ m *and* $g' = 0.0134$ $m.s^{-2}$. *Larger negative transport values correspond to a stronger simulated AC.*

7.4.4 Sensitivity of Simulated Seasonal Cycle to Reduced Gravity Parameters

The influence of the density difference ($\triangle\rho$) between the active and passive layers of the reduced gravity model (expressed by $g' = (\frac{\triangle\rho}{\rho_2})g$), and the initial depth of the active layer (H_0), on the amplitude and phase of the AC seasonal cycle are tested here. To isolate the respective effects, one of the parameters is incrementally increased in value, while the

other is kept fixed (Figure 7.6). Increasing the active layer/pycnocline depth (H_0) results in a shift of the seasonal phasing backwards in time (from black line to cyan line, Figure 7.6a). Changing the thickness of the active layer also affects the amplitude of the seasonal cycle, with a deeper pycnocline resulting in a greater mean transport and larger seasonal amplitude (e.g. cyan line Figure 7.6a). Figure 7.6b shows the shift in the seasonal cycle of the simulated AC at the ACT line when H_o is kept constant at 800 m and g' is increased to match the Rossby radius of deformation changes shown in Figure 7.6a. An increase in the density gradient between the two layers (bigger g') also results in a slightly larger seasonal amplitude, and more notably, a backwards shift in the seasonal phasing. In Figure 7.6b, a 6th model simulation is included where the initial radius of deformation is set at 30 km. The seasonal cycle of this simulation is shown in magenta, with a maximum in transport in February and a minimum in July, matching observations. It was not possible to initialize a simulation with a radius of deformation of 30 km and a pycnocline of less than 500 m as the pycnocline outcrops and the model blows up. Appendix Figure 12.7 shows the change inseasonal phasing starting from a higher g' of $0.0155 m.s^{-2}$ and a shallower active layer thickness of $H_0 = 500$ m. Similarly, when either g' or H_0, the seasonal phasing is shifted backwards in time. For the simulation where $g' = 0.0155 m.s^{-2}$ and $H_0 = 500$ m, the summer time maximum and wintertime minimum is also obtained as in this simulation the mean propagation speed of anomalies also matches aviso observations (Appendix Figure 12.8). The tests in Chapter 8 were also performed for this simulation and the results were the same.

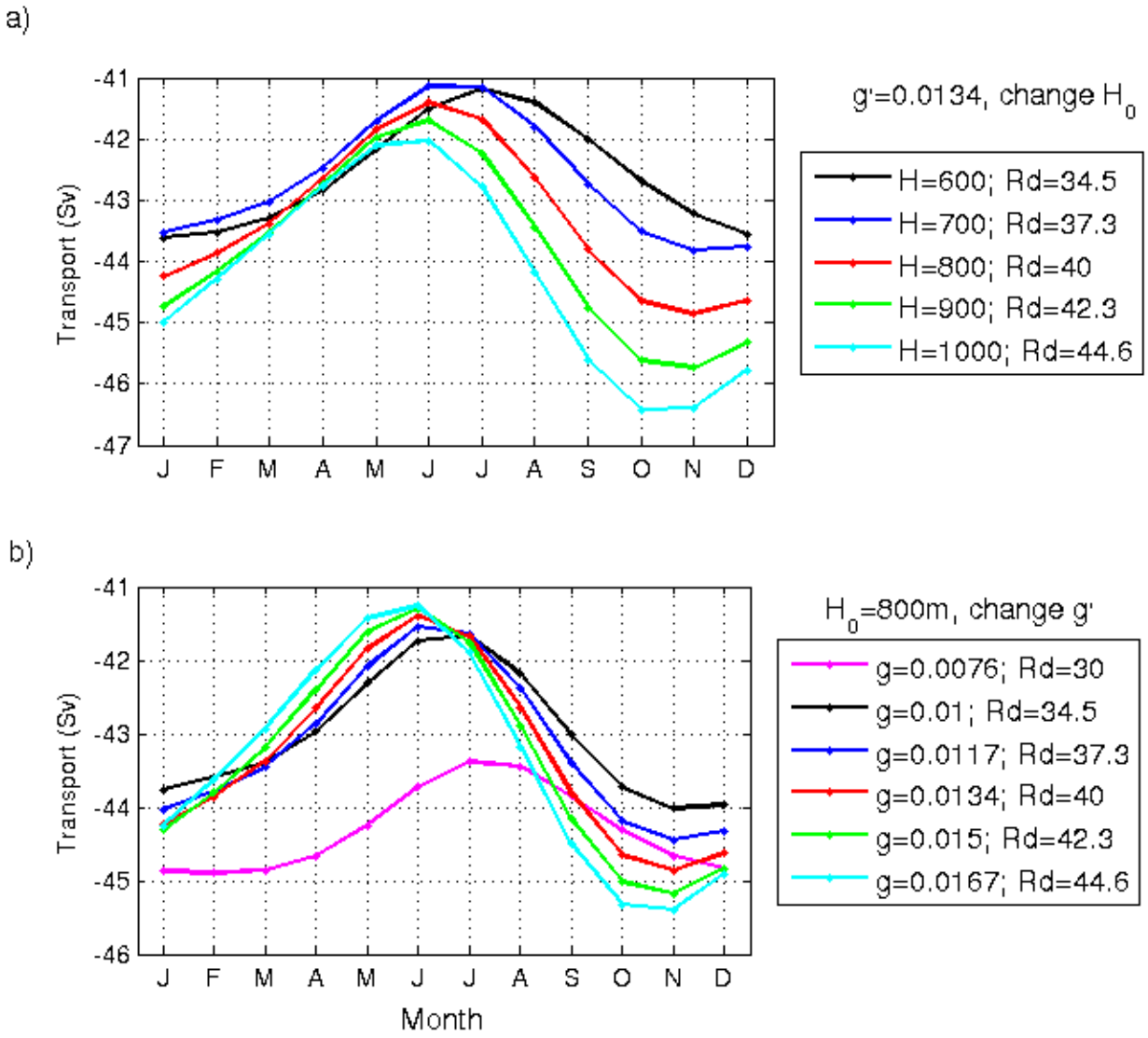

Figure 7.6: *Plots showing sensitivity of the phase and amplitude of the seasonal cycle in volume transport (Sv) at a hypothetical ACT line to reduced gravity parameters g' and H_o. A change in the density gradient between the two layers in the model is expressed in g' and a change in the active layer depth is described by H_0. In plot a) g' is set at 0.0134 $m.s^{-2}$ and H_o is increased in 100 m increments. The resultant alterations in Rossby radius of deformation are shown in the legend. In plot b) H_0 is set at 800 m and g' is increased so that the alterations in the radius of deformation match those shown in plot (a). An extra simulation is plotted in (b) showing the effects of a further decrease in g'.*

Figure 7.6 illustrates the trade-off between obtaining either a realistic amplitude or phasing of the seasonal cycle. The reason for this is that both g' and H_o influence the Rossby radius of deformation (Figure 7.6), and in turn affect the phase speed of westward propagating anomalies (Equation 16). Decreasing the depth of the active layer by 400 m (from 1000 m to 600 m) results in a 3 month shift of the seasonal maximum, from October to January (Figure 7.6a). Similarly, halving the reduced gravity parameter, from 0.015 $m.s^{-2}$ to 0.0076 $m.s^{-2}$ corresponds to a forward shift in the seasonal peak by 3-4 months, from a November peak to a February-March peak. The month of maximum AC transport thus falls later on in the year as the baroclinic Rossby waves take longer to transmit the wind stress signal to the western boundary.

The theoretical dependence of Rossby wave speed (Equation 16) and pycnocline depth on density gradient is illustrated in Figure 7.7. The simulation with a larger reduced gravity value (Figure 7.7a) has a smaller pycnocline gradient across the basin, indicating that g' acts to dampen the response of the active layer to wind forcing. The effect of a much larger g', however, overshadows the influence of the slightly smaller H on theoretical phase speeds, such that propagation is faster (1.5 $m.s^{-1}$ at the latitude of the ACT line), despite the shallower pycnocline depth at the western boundary (Figure 7.7a compared to Figure 7.7b). Conversely, a smaller density gradient results in slower theoretical phase speeds of anomalies (0.9 $m.s^{-1}$ at the latitude of the ACT line; Figure 7.7b).

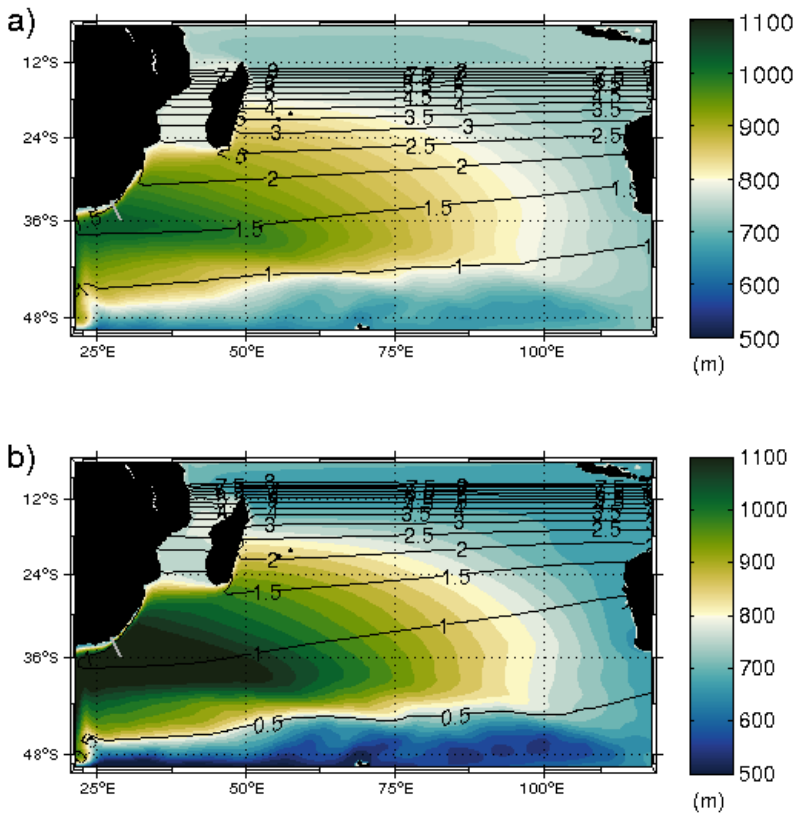

Figure 7.7: *Comparison of depth of wind driven layer (m) as background shading for simulations initialized by an H_o depth of 800 m and a g' value of a) 0.0076 $m.s^{-2}$, and b) 0.01344 $m.s^{-2}$. Contours of theoretical phase speeds ($m.s^{-1}$) are overlaid.*

In summary, if the density difference between the active and passive layers of the model is greater, Rossby waves reach the western boundary quicker, communicating a wind stress curl signal and a deepening of the thermocline to the western boundary earlier on in the year. This explains the difference in phasing between the red line and magenta lines in Figure 7.6b. Hence, although the realistic initial parameters of 800 m and 0.0134 $m.s^{-2}$ do not result in a realistic phasing of the simulated AC, a more realistic seasonal cycle can be obtained by reducing g'.

It should be noted that the theoretical phase speeds calculated for Figure 7.7 are, in fact, smaller than the actual propagation speed of anomalies in the simulation. For example, tracing anomalies crossing the basin at the latitude of the ACT line in Figure 7.4b gives a

mean propagation speed of 4.46 $km.day^{-1}$, however the theoretical speed of Rossby waves according to the active layer depths of this same simulation gives an average speed of 1.5 $km.day^{-1}$ (Figure 7.7a). This discrepancy between theoretical and observed speed of Rossby waves is described in Chapter 2, Section 2.6 and can be explained by a gradient in potential vorticity being set up by the background circulation, a process that is not accounted for in linear theory.

7.4.5 Matching Rossby Wave Speeds to Observations

Initially the reduced gravity parameters were chosen so that the initial active layer depth matched the mean depth of the pycnocline across the Southern Indian Ocean at the latitude of the ACT line (800 m), and the reduced gravity parameter ($g' = 0.0134\ m.s^{-2}$) represented the observed density difference between the upper 800 m and the lower layer (informed from WOCE observations). These 'realistic' parameters, did not, however result in a model simulation that correctly represented the first baroclinic mode radii of deformation or the phase speeds of baroclinic waves observed in the Southern Indian Ocean. Furthermore, the phasing of the simulated AC did not match that measured by the ACT experiment. This indicates that obtaining realistic radii of deformation, and consequent phase speeds, is critical when endeavouring to correctly simulate the seasonal phasing of the AC. Here, the reduced gravity model is tuned so that propagation speeds of anomalies in the model match those observed in reality. Tests revealed that forcing with the same initial active layer depth, but a smaller reduced gravity value of $g' = 0.0076\ m.s^{-2}$ accomplished this.

The mean radius of deformation at the ACT line is now 34 km, matching Chelton et al. (1998)'s observations (Chapter 2, Figure 2.6). In the simulation the mean current (boundary flow) is 222.9 km wide, comparing well with the 219 km mean boundary layer current width reported by Beal et al. (2015). The mean velocity of the simulated AC is 0.27 $m.s^{-1}$, comparing well with ACT observations, however the peak velocities of the current are slower than observed at 0.59 $m.s^{-1}$. The mean value of simulated AC transport is -44.3 Sv (Figure 7.8a), comparing well with a mean of the implied wind driven Sverdrup transport at the

location of the ACT line of -49 Sv (Chapter 5, Figure 5.7). The average depth of the wind driven layer at the location of the ACT line in the simulation is 997 m. The mean transport of the upper 997 m from the 3 years of ACT *in-situ* observations is -66.8 Sv. The difference of 22.5 Sv is similar to the cumulative volume of the buoyancy driven overturning circulation and the Indonesian Throughflow (Sprintall et al., 2009; le Bars et al., 2013), both of which are absent in the model.

The current is maximum in its south-westward direction in February (prolonged maximum January-March) and minimum in July (Figure 7.8a). This phasing agrees well with Figure 7.9 showing the seasonal cycle of the boundary layer transport from the ACT proxy during the years that the QuikSCAT scatterometer was in operation (QuikSCAT winds were used to force the model). The mean amplitude of seasonal change from the ACT proxy is 23 Sv. This, however, is the total (wind + buoyancy driven overturning) transport change, and so is not wholly appropriate for comparison with a purely wind driven model. The amplitude of WSC driven transport changes at the latitude of the ACT line was therefore investigated and found to be 15 Sv (Chapter 5, Figure 5.7). Therefore while the mean transport of the simulated AC is close to that expected for the wind driven gyre and the phasing is close to observations, the amplitude is much smaller than observed. The simulated amplitude of 1.5 Sv is an order of magnitude smaller than expected from that predicted by seasonal WSC forcing. The reason for this small amplitude in seasonal cycle is a combination of the influence of a large frictional parameter and the fact that g' and H simultaneously affect both the amplitude and phase of the seasonal cycle. Increasing either g' or H would increase the amplitude of seasonal variations in transport, but it would also accelerate the propagation speeds of anomalies across the basin and consequently shift the seasonal phasing. Decreasing the frictional coefficient would also increase the amplitude of seasonal change, but would render the model unstable. It is thus not possible here to get both a phase and an amplitude comparable to that observed.

A hovmöller plot of the propagation of simulated anomalies across the Southern Indian Ocean at the mean latitude of the ACT line is shown in Figure 7.8b. Similar to Figure 7.4, an

anomaly is initiated at the eastern boundary, propagates to about 100°E and then dies out due to destructive interference with overlying WSC of the opposite seasonality to that which created it (see Figure 5.5). There does not seem to be a coherent propagation of a signal across the basin, as signals arriving at the western boundary appear to originate from the near field area- this will be explored further in Chapter 8. Once again, a radon transform could not be used to calculate propagation speed as large areas respond semi-instantaneously to overlying WSC forcing, instead the black line overlaid in Figure 7.8b tracks the propagation of a negative SLA across the basin. An enlarged version of Figure 7.8b can be found in the Appendix (Figure 12.6) where the process of tracking of an anomaly by eye can be seen in greater detail. It takes approximately 2500 days to cover the 8040 km of the Southern Indian Ocean basin, this indicates that the phase speed of first baroclinic mode Rossby waves is approximately 3.2 $km.day^{-1}$. This propagation speed closely matches that calculated from Aviso observations (3.3 $km.day^{-1}$; Chapter 5 Figure 5.8b). When propagation speeds in the reduced gravity model match those observed in reality, then the simulated AC possesses a realistic seasonal phasing.

Tuning of the reduced gravity model to propagate anomalies at the same speed as those observed with altimetery, using the same initial active layer depth but a smaller reduced gravity value of $g' = 0.0076\ m.s^{-2}$, resulted in a realistic baroclinic radius of deformation at the latitude of the ACT line, and a phasing of the seasonal cycle of the AC that agrees well with the ACT 23-year proxy.

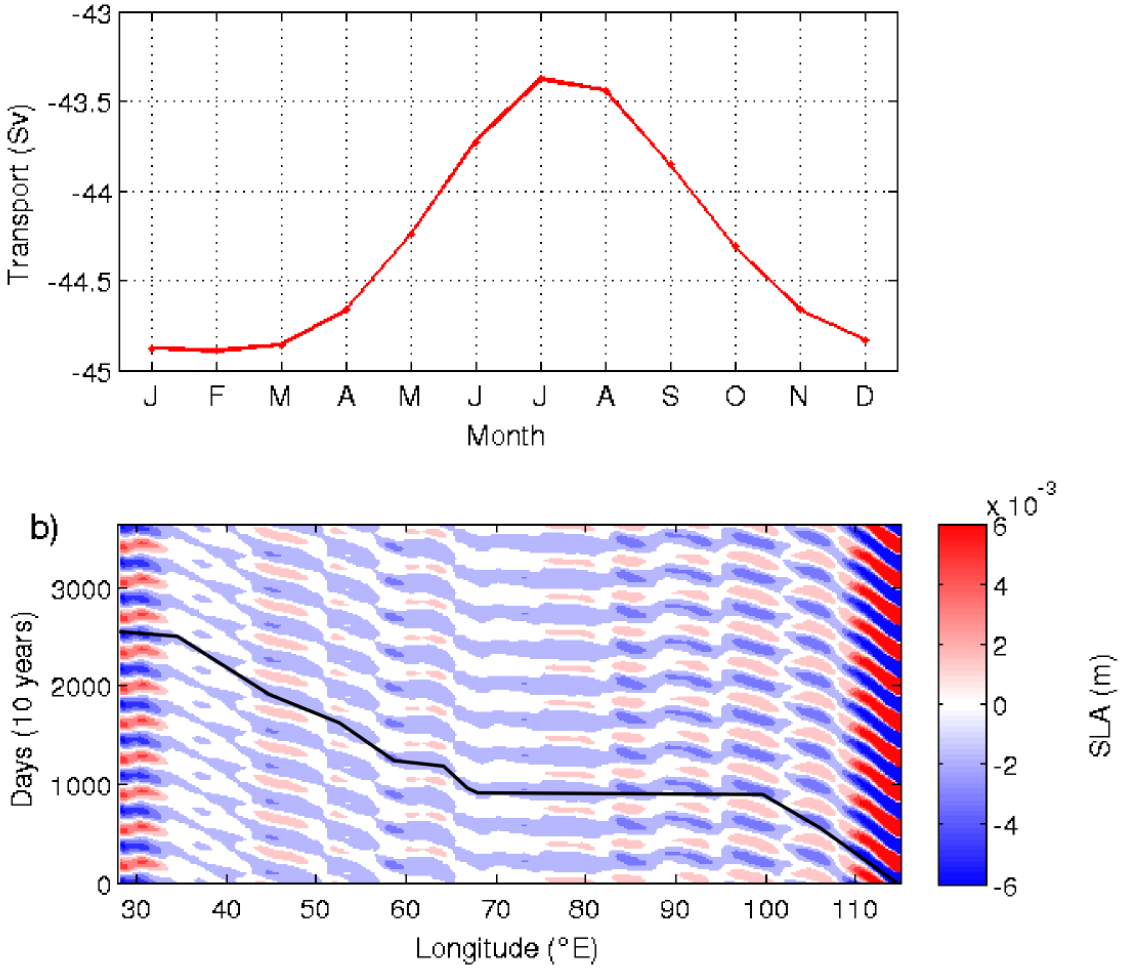

Figure 7.8: *a) Seasonal cycle of Agulhas Current in model simulation initiated with a thermocline depth of 800 m and* $g' = 0.0076\ m.s^{-2}$*. The flow is south-westward, therefore more negative values correspond to a stronger current. b) Hovmöller plot showing the propagation of sea level anomalies (SLA, m) across the basin at the mean latitude of the ACT line during the final 10 years of simulation. The black line tracks the propagation of an anomaly across the basin in order to estimate the average phase speed.*

Historic ocean model studies have been unable to correctly simulate the seasonal phasing of the AC (Biastoch et al., 1999; Matano et al., 2002; Reason et al., 2003). For direct comparison of observations with ocean general circulation models (OGCMs), the seasonal anomalies

of the the Modular Oceans Model (MOM2) of Biastoch et al. (1999) and the Parallel Ocean Circulation Model (POCM) of Matano et al. (2002) have been overlain in Figure 7.9. Also included here are the AC seasonal anomalies at the location of the ACT line in the Western Indian Ocean Energy Sink model (WOES) and the HYbrid Coordinate Ocean Model (HYCOM). WOES has 60 vertical levels and three grids nested into each other with resolution increasing from 1/4°, 1/12° to 1/36° over the AC (Penven, personal communication). This is the state of the art modern ROMS/CROCO regional simulation of the AC. The HYCOM simulation is 1/10° resolution with 30 vertical layers (Vermeulen, personal communication). The data is from a free-running HYCOM used to generate the static ensemble in a data assimilation experiment of the Agulhas region (Backeberg et al., 2014). Figure 7.9 reveals that the two historic OGCMs which have published results on AC seasonality, and the unpublished results from the regional ROMS and HYCOM simulations, all predict a winter-spring maximum in southward AC volume transport with maximums falling between August and November. The historic MOM2 and POCM models are sinusoidal in their seasonality, while the WOES and HYCOM model has high variance at sub-annual time-scales. The AC simulated by WOES is strongest in April, June and November, while the AC in the HYCOM model has peaks in January, May and November. Figure 7.9 highlights the disagreement in AC seasonality between OGCMs and observations, and reveals the comparative skill of the idealized model presented here in simulating the observed seasonal phasing.

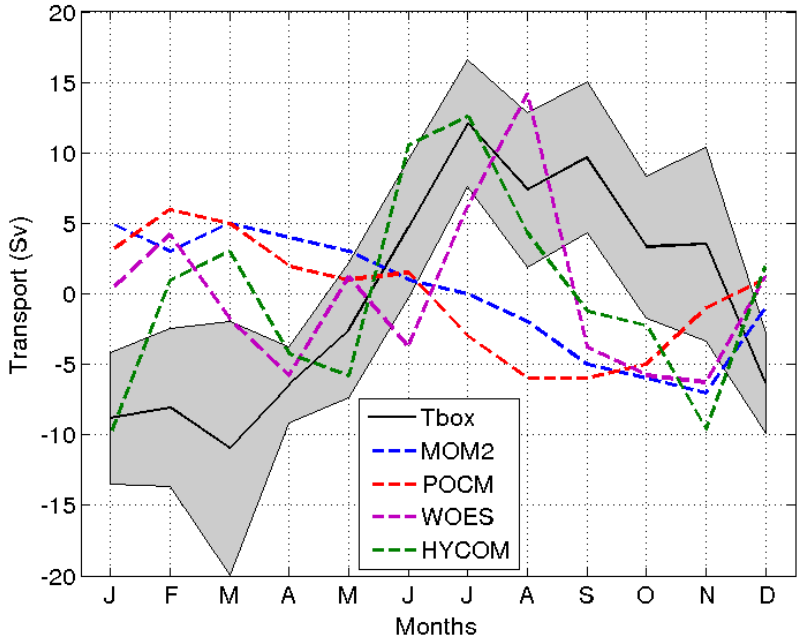

Figure 7.9: *Observed seasonal anomalies of the ACT boundary layer transport (Tbox; black; mean = -86.3 Sv) from proxy time-series over the period 1999-2009. Solid black line shows the monthly mean values and shading shows the 95% confidence intervals assuming a normal distribution. Also shown for direct comparison are the seasonal anomalies in AC transport from the Modular Oceans Model (MOM2; blue) of Biastoch et al. (1999), the Parallel Ocean Circulation Model (POCM; red) of Matano et al. (2002), and the Western Indian Ocean Sink model (WOES; purple) from Penven (personal communication). Negative anomalies in transport indicate a stronger current as the AC flows south-westward*

7.5 Summary and Discussion

A reduced gravity model is able to capture the main features of the pycnocline circulation of the South Indian Ocean subtropical gyre, with a strong narrow western boundary current located in the same place as the AC. The initial set-up of the model was based on WOCE measurements of pycnocline depth and mean density gradient in the latitude band of the ACT line: H_0 = 800 m and $g' = 0.0134\ m.s^{-2}$. In this simulation, however, the speed

of westward propagation of anomalies was about 1 $km.day^{-1}$ faster than observed and the seasonality of the AC was shifted earlier to a maximum in flow in November (Figure 7.4a).

The seasonal cycle of the simulated AC was found to be highly sensitive to the initial conditions of reduced gravity and pycnocline depth. The magnitudes of these parameters are important as they set the radius of deformation, and consequently the phase speed of propagating wind-driven disturbances in the system. When the active layer (H_0) is deepened, or the density gradient between the two layers (g') is increased, the amplitude of seasonal fluctuations in transport increases. This results in a deeper AC with a larger transport and greater seasonal variations. The same is true for increasing the density gradient between the surface active layer and the lower layer, expressed by enlarging the reduced gravity parameter.

The limitation of increasing the amplitude of the seasonal cycle is that the phasing is simultaneously affected. While a larger seasonal variation in transport can be achieved by increasing g' or H_0, these parameters also influence the radius of deformation which consequently leads to faster propagation of Rossby waves and a shift in the seasonal phasing of the AC. The amplitude of seasonal variability would be larger if the frictional parameter in the model were decreased, the illustration of this is unfortunately not possible as the model becomes unstable and blows up.

Tuning the model to observed Rossby wave propagation speed was found to be the key to reproducing the observed seasonal phasing of the AC. An initial thermocline depth of 800 m and a g' of 0.0076 $m.s^{-2}$ yielded anomalies propagating westwards across the basin at the mean latitude of the ACT line at an average speed of -3.2 $km.day^{-1}$. This is very close to the observed phase speed of Rossby waves at the same latitude in the Southern Indian Ocean measured using Aviso data. The seasonality of the transport of the simulated AC became maximum in January-February-March and minimum in July. This agrees well with the seasonality of both the full 23-year proxy shown in Figure 4.4, and the proxy seasonal mean only during the QuikSCAT operational period shown in Figure 7.9. To verify the results from the reduced gravity model, an analytical model was used to simulate the passage of a

baroclinic Rossby wave across the Southern Indian Ocean and the results are presented in Supplementary Material Section 11.1. This simplified set-up showed that a similar implied seasonal phasing of the western boundary current can be obtained by modelling the passage of a first mode baroclinic wave at -34.5°S travelling at -3.2 $km.day^{-1}$.

7.6 Conclusion

A reduced gravity model with one wind driven active layer, and a stationary bottom layer of infinite depth, forced by climatological winds, is able to adequately simulate the major features of the Southern Indian Ocean gyre. This indicates that a first baroclinic mode reduced gravity wave appears to be an adequate representation of the main signal. The seasonality of the AC in this model is found to be highly sensitive to the propagation speed of Rossby waves, which determines the arrival time of the wind stress signal at the western boundary. By tuning the Rossby wave propagation speeds of the model, however, to those observed from altimetry, an AC with a prolonged maximum flow over January-February-March and a minimum flow in July is simulated. This seasonality agrees with observations. When compared with recent unpublished results from realistic ocean models (ROMS-WOES and HYCOM simulations), the highly idealized reduced gravity model presented here shows more skill in capturing the seasonal phasing.

The satisfactory ability of the reduced gravity baroclinic model enables a further investigation into which characteristics of Indian Ocean wind forcing predominantly influence the seasonal phasing at the western boundary, presented in Chapter 8.

8 Sensitivity to Indian Ocean Wind Forcing

8.1 Introduction

Earlier results indicated that sea level anomalies (SLA) from remote wind stress curl (WSC) forcing do not reach the western boundary of the Southern Indian Ocean at the latitude of the ACT line. This suggests that the seasonality of near-field winds, winds within 10° of the western boundary, may play an important role influencing the seasonal variability of the Agulhas Current (AC). Furthermore, results from Chapter 7 suggested that the seasonal cycle of the simulated AC is highly sensitive to the speed of propagation of SLA across the basin. This propagation speed is directly proportional to the depth of the wind driven layer, H, via the relationship with the radius of deformation (Equation 15 and 16). The depth of this layer, and thus the propagation speed of first baroclinic mode Rossby waves, are influenced by a number of factors: local changes in H due to Ekman pumping and suction, a change in H due to an anomaly associated with an incoming Rossby wave, and the mean background H set by the mean WSC over the basin. To decompose the influence of these factors on propagation speeds and the consequent seasonality of the simulated AC, this chapter investigates the influence of zonally varying winds, local winds directly over the current, near- and far-field winds, and background mean WSC.

8.2 Key Question

Which characteristics of Indian Ocean wind forcing predominantly influence the seasonal phasing at the western boundary?

8.3 Data and Methods

8.3.1 1 1/2 Layer Model That Resolves Agulhas Current Seasonality

The set-up and structure of the 1 1/2 layer reduced gravity model using the Regional Ocean Modelling System (ROMS) as a platform is described in Chapter 7, Section 7.3.1. This model simulates the first baroclinic mode response of the upper layer of the ocean to wind forcing, as the lower layer is stationary and of infinite depth (see Figure 7.1 for a schematic of the reduced gravity model set-up). The reduced gravity model is forced by climatological QuikSCAT winds which were identified as the most appropriate wind product for use in this study in Chapter 5.

As described in Chapter 7, the seasonality of the simulated AC is very sensitive to the choice of density gradient between the active and passive layers (reflected in the value of reduced gravity by $g' = (\frac{\triangle \rho}{\rho_2})g$) and the initial depth of the wind driven layer (H_0). Extensive testing in Chapter 7 showed that g' and H_0 values of 0.0076 $m.s^{-2}$ and 800 m, respectively, gave a mean Rossby wave propagation speed and a seasonal phasing of the simulated AC that agreed well with observations. This simulation, where the AC is at a maximum in February and a minimum in July, will be used for the tests undertaken in this chapter. Figure 8.1 shows a summary of results from this simulation. The SLA are measured for the latitude range of the Agulhas Current Time-series (ACT) mooring array, and the seasonal cycle of the simulated AC is calculated as the transport perpendicular to the ACT line. Note that as mentioned in the previous chapter, a similar result is obtained using a shallower active layer and a larger g' (Appendix Figure 12.8). As long as the propagation speed of anomalies across the basin is close to observations, the observed seasonal phasing of the AC is reproduced. The wind sensitivity tests presented in this Chapter where performed for the simulation with alternative (compensating) reduced gravity values and the findings were the same.

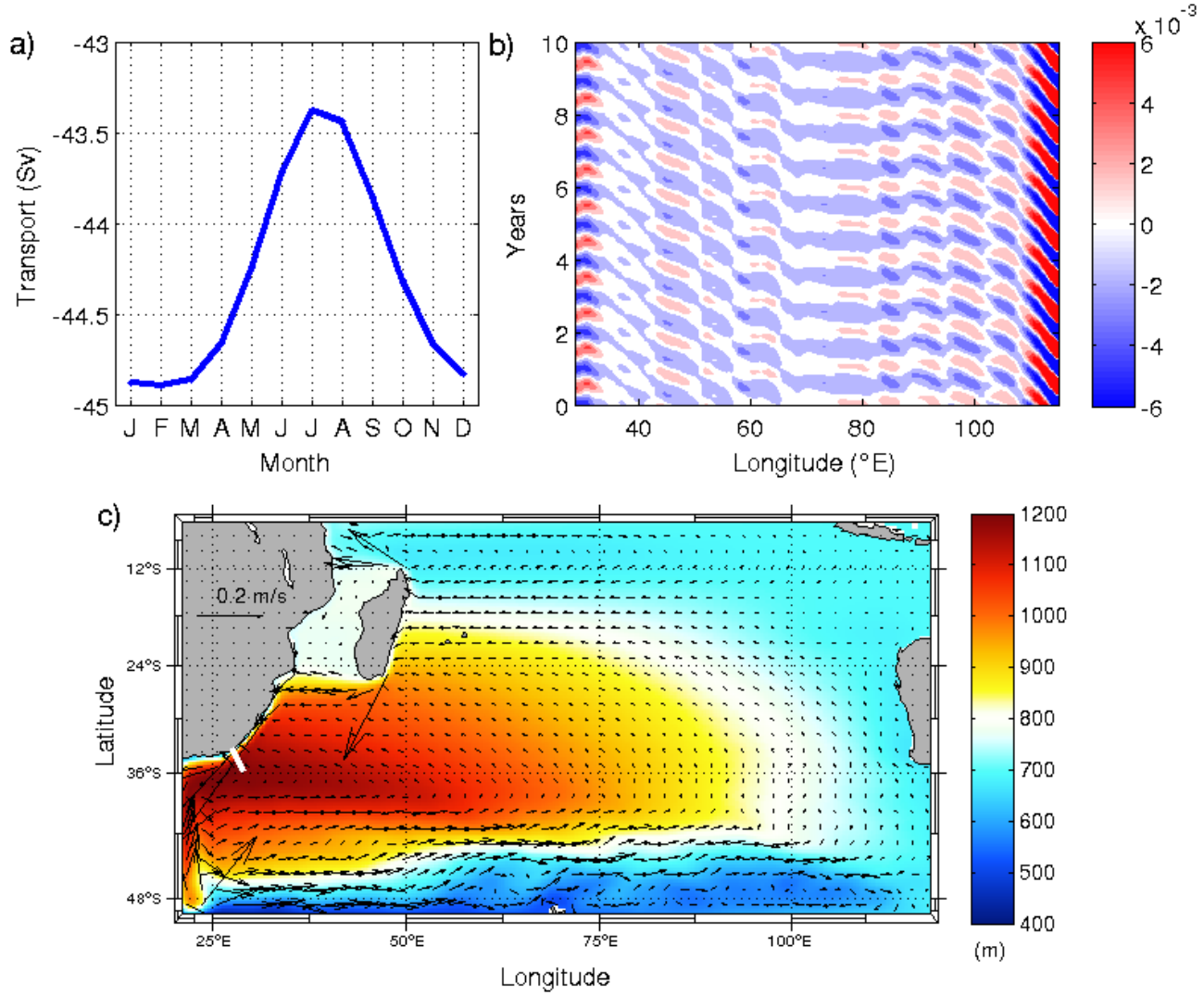

Figure 8.1: *Summary of results from reduced gravity model initialized with an active layer depth of 800 m and a reduced gravity parameter of 0.0076 m.s^{-2}. a) Seasonal cycle of transport (Sv) perpendicular to ACT line in model. The flow is south-westward, therefore more negative values correspond to a stronger current. b) Propagation of sea level anomalies (SLA; m) across the basin at the latitude of the ACT line. c) Mean surface currents of Southern Indian Ocean gyre in model with thickness of active layer (m) as background shading.*

8.4 Results

8.4.1 Role of Zonally Varying winds

Chapter 5 explored how Southern Indian Ocean winds vary with seasons and revealed that different areas of the basin have differing seasonal anomalies at the latitude of the ACT line. To explore the sensitivity of the simulated AC seasonality to this zonal WSC variability, the 1 1/2 layer reduced gravity model is forced with zonally averaged wind stresses for each month. The seasonal cycle of transport at the ACT line from this simulation (Figure 8.2a) is shifted backwards in time by 2 months (compared to Figure 8.4a), to give a December maximum in transport. The July minimum is preserved, and the general similarity in phasing indicates that longitudinal variations in wind stress do not have a dominant influence on seasonality. The mean AC transport is reduced by 3.7 Sv in this run (average=-40.6 Sv), indicating that forcing with zonal mean winds has reduced the strength of the Southern Indian Ocean gyre.

Without the zonal variations in WSC, the instantaneous nature of the sea level response in the central region of the basin can now clearly be seen (Figure 8.2b). WSC kicks off a disturbance at the eastern boundary of the basin, this SLA propagates coherently westwards for approximately 6 months. Thereafter, the magnitude of the SLA is decayed as it encounters a WSC anomaly of the opposite season to that which initiated the disturbance. After one year, the SLA dies out due to destructive interference with overlying winds. SLAs therefore propagate from the eastern boundary to approximately 105°E and are subsequently eroded to near zero. Another small anomaly is initiated at 100°E and propagates to about 95°E, but is then also eroded. The rest of the basin experiences an instantaneous adjustment to wind stress forcing as it receives no signals from incoming Rossby waves. There is evidence that the model has not reached full equilibrium shown by the increasing zonal extent of the negative anomalies located over the center of the basin with time. Given the small magnitude of these anomalies, the influence is deemed negligible. Seasonal changes at the western boundary can be explained by a semi instantaneous response to winds in the area, as there is no evidence suggesting the propagation of a remote signal into the western boundary area from Figure 8.2b.

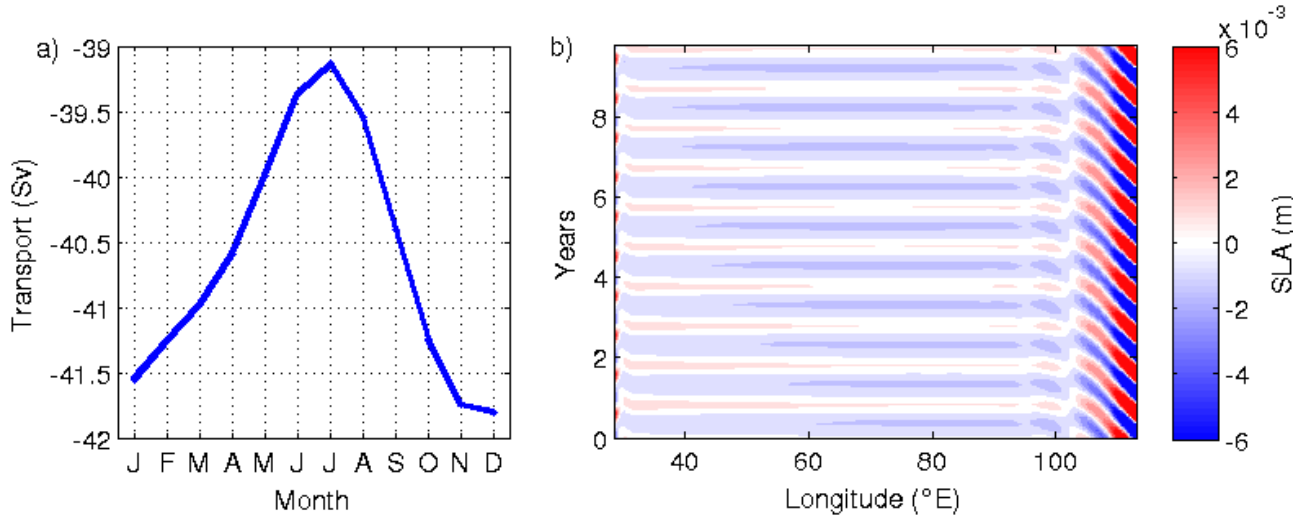

Figure 8.2: *a) Seasonal cycle for transport (Sv) across the ACT line, larger negative values indicate a stronger flow. b) Hovmöller plot of sea level anomalies (SLA; m) at 34.5°S from reduced gravity model forced by only zonal mean winds*

8.4.2 Role of Local Winds

Previous results indicated that signals from remote WSC never reach the western boundary. The influence of local winds that overly the AC is thus investigated here. In this simulation, normal zonally varying winds were used, but the seasonal fluctuations of remote winds were removed. A hyporbolic tangent smoothing function was used to smooth the effects of seasonal changes over an area of 4° longitude. The width of this smoothing band was tested, and 4° was found to be appropriate to avoid the creation of spurious WSC. Starting at the end of the ACT line, at 29°E, the amplitude of seasonal anomalies are tapered off to 33°E, after which the model is forced with mean winds possessing no seasonal alterations. The seasonal phasing of the AC from this simulation (Figure 8.3a) is very similar to that shown in Figure 8.2a where the model was forced with zonal mean winds. The similarity in phasing shows that in both simulations, the western boundary response was dominated by local overlying wind forcing.

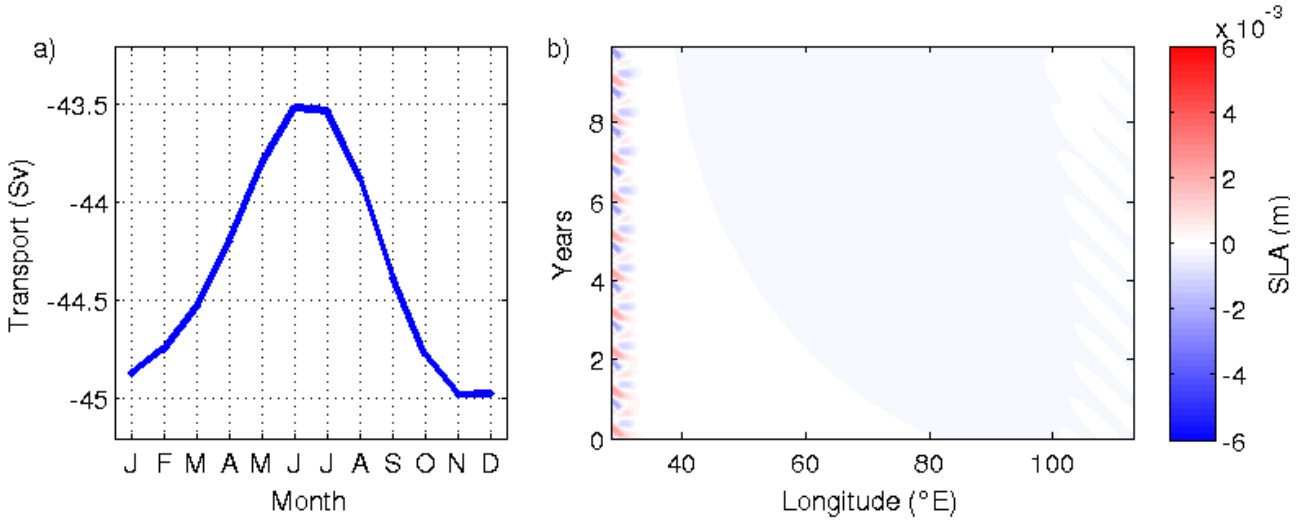

Figure 8.3: *a) Seasonal cycle for transport (Sv) across the ACT line, larger negative values indicate a stronger flow. b) Hovmöller plot of sea level anomalies (SLA; m) at 34.5°S from reduced gravity model forced with seasonally varying winds to the west of 29°E, tapering off to no seasonality east of 33°E*

Looking closely at Figure 8.3b, some spurious blue shading is visible emanating from the eastern portion of the plot. The westward growth of this small spurious anomaly with time once again indicates that the model has not reached full equilibrium. The presence of this anomaly in itself is surprising as wind stress is constant to the east of 33°E and so there is no seasonal wind stress forcing over the majority of the basin. A likely explanation for this is a Kelvin wave that rapidly communicates the anomalies in sea surface height (SSH) experienced at the western boundary clockwise around the basin (along the equator and down the eastern boundary). Evidence of these proposed Kelvin waves can be seen in Appendix Figures 12.9 and 12.10 which show the SLA for the basin for the month of maximum transport of the simulated AC, November, and minimum transport, July. The model outputs monthly mean values, and so the actual propagation of a wave cannot be resolved, but tiny SLA bands along the equator are identified. These signals likely initiate small anomalies in SSH along the eastern boundary. The color bars of all hovmöller plots in this chapter are the same, thereby indicating that the magnitude of this sea level disturbance is very small compared

to the westward propagating anomalies shown in Figure 8.1b. Increasing the sponge layer in the model would likely eliminate these minor features entirely, but as they are thought to have little effect on the solution, the model set-up is left unchanged.

Although the seasonal cycle from this simulation is similar to that from the zonal mean wind test, neither match that of the AC in the simulation forced with normal winds where the phasing is in line with observations (Figure 8.1). This suggests that local winds overlying the ACT line cannot, alone, explain the seasonality observed in AC transport, and that winds from further afield must have an important contribution.

8.4.3 Role of Near-Field Wind Stress Forcing

As local WSC alone cannot explain the AC phasing, the zone of seasonal wind forcing is incrementally expanded so as to determine the threshold beyond which seasonal variations in WSC have little effect. Identical to the local wind experiment, a smoothing area of 4° longitude was used, over which the influence of seasonally varying winds is decreased using a tangent function. To start, 40°E was chosen as the division for seasonally varying winds. First the seasonality of winds to the west of 38°E was preserved and winds to the east of 42°E were fixed to their yearly mean (red line Figure 8.4). Then the inverse was applied so that remote winds in the eastern portion of the basin varied seasonally, while regional winds in the west were fixed to the annual mean (green line Figure 8.4). The original seasonal cycle from the run with normal winds is shown in blue in Figure 8.4.

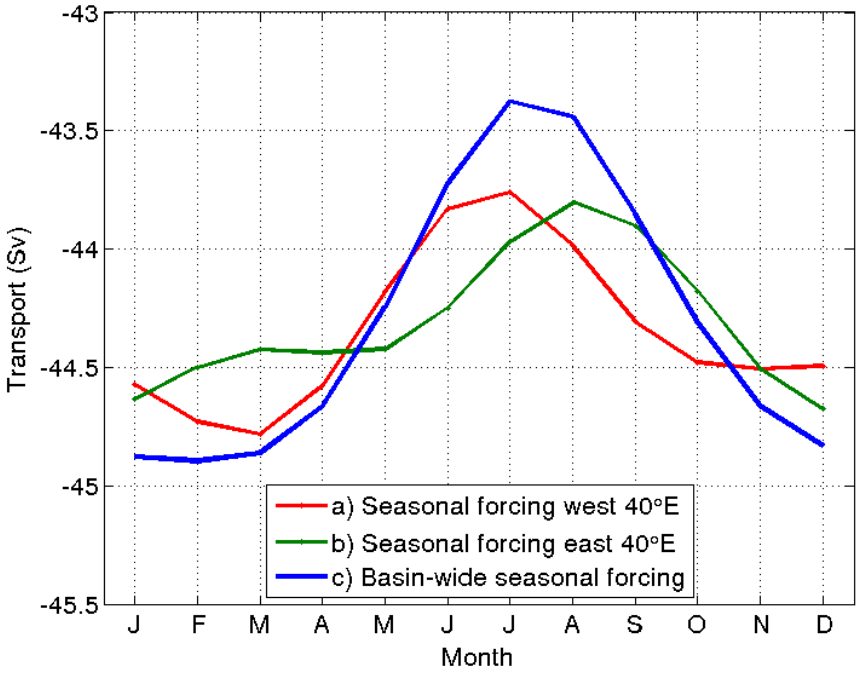

Figure 8.4: *Seasonal transport (Sv) perpendicular to a hypothetical ACT line in the model for simulations forced with seasonally varying winds in different portions of the basin. a) Regional winds seasonally vary while remote winds are kept at the annual mean (red). b) Remote winds seasonally vary while regional winds are kept at the annual mean (green). (c) AC transport from basin-wide seasonal forcing (blue).*

Figure 8.4 shows that neither seasonally varying regional winds (to the west of 40°E), nor seasonally changing remote winds (to the east of 40°E), have a dominant influence on the observed seasonal cycle. Regional winds (red line Figure 8.4) drive changes of a similar phasing to the overall seasonality with maximum in AC transport in February-March and a minimum in July. The amplitude of the regional wind influence is, however, smaller than the total seasonal cycle. This indicates that wind effects from too far afield were included in the 'regional' wind category. The dividing line is therefore moved 5° westwards to 35°E and the seasonal cycle from this simulation is shown in Figure 8.5.

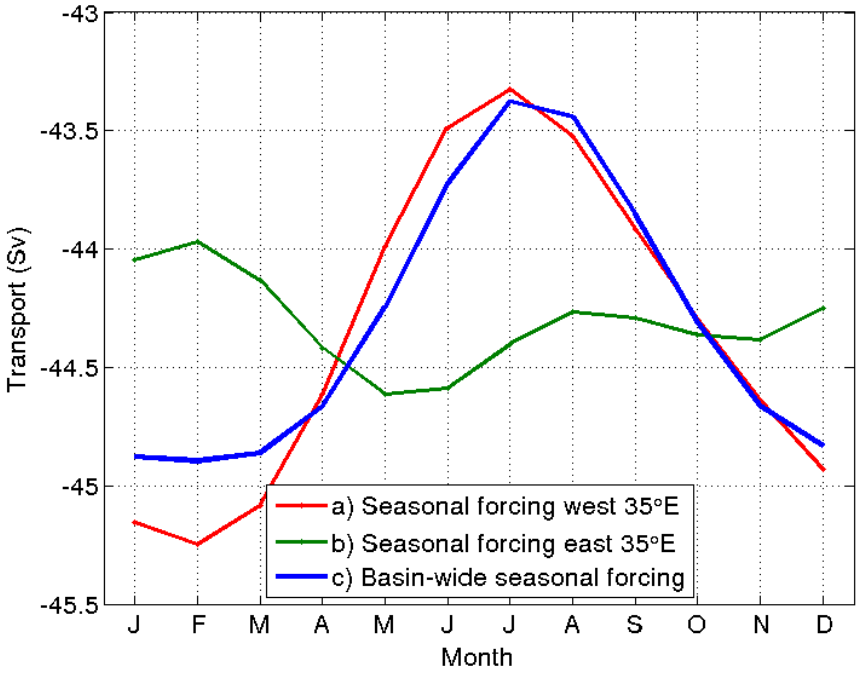

Figure 8.5: *Seasonal transport (Sv) perpendicular to a hypothetical ACT line in the model for simulations forced with seasonally varying winds in different portions of the basin. a) Near-field winds seasonally vary while far-field winds are kept at the annual mean (red). b) Far-field winds seasonally vary while near-field winds are kept at the annual mean (green). c) AC transport from basin-wide seasonal forcing (blue).*

Seasonally varying near-field winds (to the west of 35°E) dominate the total seasonality at the western boundary with a very small contribution from far-field winds (Figure 8.5). Far-field winds act to decrease and broaden the February maximum of the simulated AC, resulting in an overall prolonged January-February-March maximum in the simulation with normal forcing. The 23-year transport proxy indicated that the AC is strongest in March and weakest in July-August (Chapter 4, Figure 4.4). The inclusion of winds slightly further afield than those of the local wind run has shifted the seasonal phasing closer to that observed in reality, revealing the dominant influence of near-field WSC.

8.4.4 Role of Background Circulation

To investigate the influence of the shape of the background gyre circulation on the seasonal cycle at the western boundary, the model is forced with basin-wide wind stress anomalies (mean removed). The resultant seasonal cycle and hovmöller plot at the latitude of the ACT line is shown in Figure 8.6. The seasonal cycle is now effectively the anomaly from the mean as there is no background flow upon which the anomalies are projected. The AC seasonal cycle shows strongest south-westward transport in November, a 3 month backward shift in seasonality. This highlights that the mean WSC, which sets up the gyre circulation, is important in influencing the propagation of anomalies and the consequent seasonality of the western boundary. The active layer, which can be thought of as the pycnocline as it represents a step change in density, acts as a backdrop for the propagation of Rossby waves. A deeper pycnocline will result in faster propagation speeds, whereas the inverse is true for a shallower pycnocline (Equations 15 and 16). These influences are removed in this run as the anomalies are effectively projected onto a flat pycnocline.

Chapter 7 exposed the sensitivity of the seasonal phasing of the simulated AC to the propagation speeds of the SLA communicating the WSC signal. By changing the slope in active layer depth across the basin (removing the mean WSC), the speed of SLA propagation has been altered. A modification of propagation speed in turn changes the areas of constructive and destructive interference with WSC, thereby fundamentally altering the response of the basin to WSC forcing and the consequent seasonal variability at the western boundary.

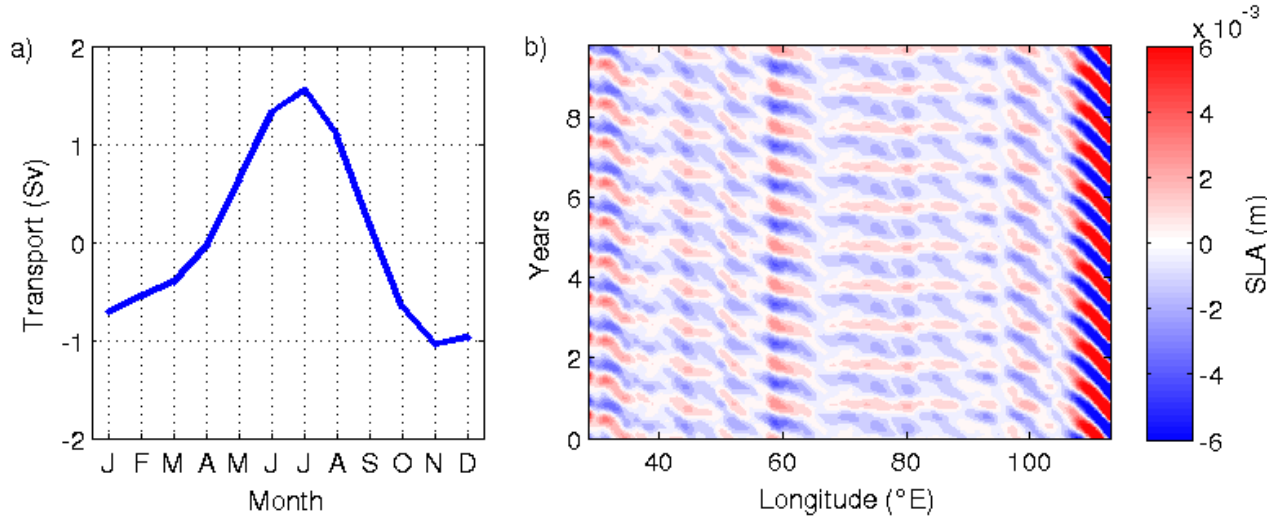

Figure 8.6: *a) Seasonal cycle for transport (Sv) across the ACT line, larger negative values indicate a stronger flow. b) Hovmöller plot of Sea Level Anomalies (SLA, m) for 34.5°S from reduced gravity model run in ROMS framework forced by wind stress anomalies only*

Figure 8.5 indicated that near-field winds dominate the seasonal cycle at the western boundary. The concept that background circulation, set up by mean wind forcing over the whole Southern Indian Ocean, could be important in determining the seasonality of the AC may therefore seem somewhat contradictory. To elucidate this point, the reduced gravity model was forced with seasonal anomalies to the west of 35°E and zero wind forcing in the rest of the basin. The resultant seasonal cycle of the simulated AC, and the hovmöller plot of SLA, are shown in Figure 8.7. The transport anomalies now possess a peak in south-westward flow in March and a minimum in July. This seasonality is different to that shown in Figure 8.6 where the model is forced with basin-wide wind stress anomalies, indicating that in the previous run, SLA from more remote wind forcing were propagating into the western boundary region to influence the seasonal adjustment of the simulated AC. The phasing of the seasonal cycle driven by near-field WSC anomalies alone is in line with the phasing shown in red in Figure 8.5 for total wind forcing (mean + seasonal anomalies) in

the near-field area. The similarity in phasing indicates that close to the western boundary, the absence of a tilt in pycnocline does not significantly affect SLA propagation and the consequent AC seasonal phasing. The absence of background circulation does, however, almost halve the amplitude of seasonal change (1.9 Sv in Figure 8.5a versus 1 Sv in Figure 8.7a). Note that these amplitudes are much smaller than those observed in reality due to the small g' needed to capture realistic Rossby wave speed and the large friction used in the reduced gravity model to maintain stability.

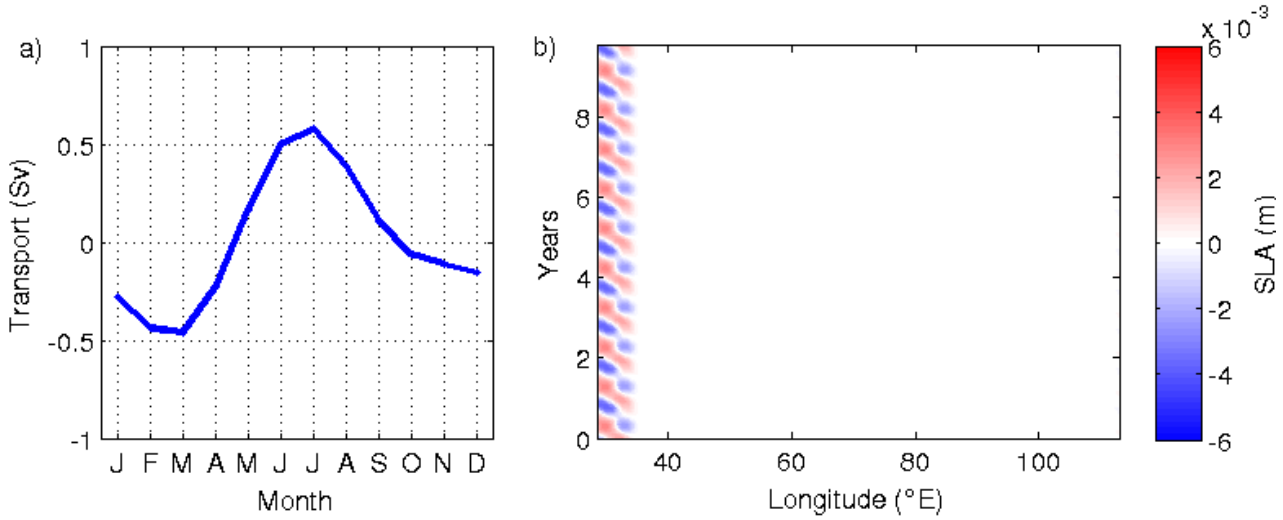

Figure 8.7: *a) Seasonal cycle for transport (Sv) across the ACT line, larger negative values indicate a stronger flow. b) Hovmöller plot of sea level anomalies (SLA, m) from reduced gravity model simulation forced only with wind stress anomalies to the west of 35°E*

8.5 Summary and Discussion

This chapter explored the influence of different elements of Southern Indian Ocean WSC on the seasonal phasing of the simulated AC. Forcing the model with zonal mean seasonal WSC exposed the semi-instantaneous nature of the response to wind forcing over most of the basin. Rossby wave signals originating from the eastern boundary do not coherently propagate across the basin as they die out during their journey westwards due to destructive

interference with overlying WSC. The seasonal phasing of the AC for this run was shifted back in time by 2 months. Forcing with only local seasonal WSC dirctly over the AC, produced an AC seasonal cycle (Figure 8.3a) very similar to that of the simulation with zonal mean winds (Figure 8.2a). This confirms that in the zonal mean wind simulation, the western boundary was responding to overlying winds, alone, with no signals arriving from remote wind forcing. The simulated November maximum in seasonality, however indicates that a local response to overlying winds cannot explain the observed AC seasonal cycle.

Testing the threshold of near- versus far-field seasonal WSC importance in setting AC seasonality showed that winds to the west of 35°E have a dominant affect. Seasonal winds in the rest of the basin have little impact on the western boundary seasonal variability. Included within this near-field wind domain is the influence of local winds, indicating that while these seasonal winds cannot by themselves explain the observed seasonality, they do have a significant influence. Near-field WSC forces an AC transport with a maximum in February and minimum in July. The seasonal fluctuations of WSC from further afield acts to decrease this February maximum to result in a slightly diminished in magnitude and temporally broader January-February-March peak in flow.

The importance of background mean circulation set up by mean WSC was elucidated when the model was forced with WSC anomalies only, and the seasonality of the AC shifted backwards by 3 months. The mean wind stress sets the scene regarding pycnocline depth, without which anomalies are left to propagate essentially on a flat surface. The depth of the pycnocline influences the phase speed of signals carrying the wind stress information, and as was shown in the previous chapter, these propagation speeds are important in setting the timing of the arrival of WSC signals at the boundary. In summary, the seasonal variation of near-field winds is important in exciting SLA which propagate to the western boundary, while the mean winds over the whole basin set the shape of the gyre upon which the SLA are projected. Together, these two affects result in a simulated AC possessing a prolonged January-February-March maximum and July minimum, agreeing well with observations (Figure 7.9).

8.6 Conclusion

Results from wind forcing sensitivity experiments using a reduced gravity model indicate that near-field wind forcing, along with background circulation, play decisive roles in determining the seasonality of the AC. Local winds alone load to a November-December maximum in simulated AC flow, but when combined with near-field winds out to 35°E, the observed AC phasing is recovered. Far-field WSC anomalies die out while crossing the basin and therefore have little impact on western boundary seasonality. Findings from this study elucidate the role of near-field winds and baroclinic processes in determining the seasonal phasing of the AC.

9 Summary and Concluding Remarks

9.1 Summary of Results

This study explored the seasonal variations of the Agulhas Current (AC), and assessed the contributions of barotropic and baroclinic processes, and near- versus far-field winds, to the observed seasonality. The following paragraphs summarize the findings relating to the key questions of the study.

9.1.1 How does the Agulhas Current vary seasonally?

In-situ observations and a 23-year transport proxy from the Agulhas Current Time-series (ACT) experiment showed that the AC is strongest in summer (February-March) and weakest in winter (July-August), with a 17.5% change in volume transport between seasons. The summertime increase in flow is associated with a broader mean current, with the core of the jet located close to the continental shelf edge. In wintertime the current core moves slightly offshore and the width of the AC decreases. While the largest magnitude of change is in the upper 1000 m, the seasonal alterations are full-depth, indicating an equivalent-barotropic nature of change. The sea surface height (SSH) pattern associated with the seasonal shifts show that a broad region of elevated SSH is located at the offshore end of the ACT array in summer, suggesting the presence of seasonal recirculations.

9.1.2 What is the annual variability of Southern Indian Ocean winds, and what is the nature of the Rossby wave adjustment to this wind forcing?

A comparison of wind atlases showed that broad-scale features of seasonal wind stress curl (WSC) are robust between products, but QuikSCAT has the most skill in resolving small-scale features close to the boundaries. QuikSCAT was thus identified as the best product for use in this study, and further investigation revealed that the east and west portions of the Southern Indian Ocean at the latitude of the ACT line have opposing WSC seasonality. The seasonal variation in WSC accounts for 12% of the total wind variance with the integrated

affect of the WSC variation driving a maximum in Sverdrup transport in winter. With the opposite seasonal cycle, the AC is not in instantaneous balance with basin-wide WSC, as could be expected for a baroclinic system, where Rossby waves communicating the WSC signal take on average over 6 years (3.3 $km.day^{-1}$) to cross the Southern Indian Ocean basin at the latitude of the ACT array. The zonal propagation speeds of anomalies were found to vary significantly with longitude. Sea level anomalies (SLA) travel fastest in the western portion of the basin where the pycnocline is deepest, and there is an area from approximately 65°E to 95°E where there is little propagation. This suggests destructive interference from overlying WSC and indicates that signals from remote WSC forcing do not arrive at the western boundary.

9.1.3 How does a barotropic adjustment to wind forcing contribute to the observed seasonality of the Agulhas Current?

A single layer model possessing realistic bathymetry showed that the barotropic contribution to AC seasonality is small, as the barotropic signal is steered away from the South African continental shelf by the Mozambique Plateau. The seasonal cycle of the barotropic flow at the location of the ACT line is maximum in winter (July), disagreeing with observations. Results from the barotropic model indicate that the AC seasonality is linked to a southward propagation of signals via the Mozambique Channel, as has been suggested by previous ocean model studies (Biastoch et al., 1999; Matano et al., 2002). Furthermore the seasonal cycle of the AC and the seasonality of the flow through the Channel in the barotropic simulation are similar in phase to those reported by previous model studies. This suggests that perhaps the barotropic adjustment was too dominant in these models, resulting in a reported winter-spring maximum in AC transport.

9.1.4 How is the seasonality of the Agulhas Current influenced by a first baroclinic mode adjustment to climatological Indian Ocean winds?

By tuning initialization parameters so that Rossby waves in the model propagate on average at the same speed to what is observed at the latitude of the ACT line, a reduced gravity 1 1/2 layer baroclinic model is able to correctly reproduce the observed seasonal phasing of the AC. An initial run using a realistic pycnocline depth and density gradient revealed an AC seasonal cycle that was shifted 3 months earlier than that observed, as propagation speeds of Rossby waves in the model were faster than in reality. The seasonal cycle of the simulated AC was found to be sensitive to Rossby wave speeds, which are governed by the initial values of pycnocline depth (H_0) and reduced gravity (g'). By reducing the density gradient between the active and passive layers so that SLA propagation speeds match observations, a simulated AC with a maximum transport in February (prolonged peak from January to March) and a minimum in July was obtained, agreeing well with ACT observations. The seasonal amplitude of the simulated AC was smaller than what is predicted by seasonal WSC forcing. The reason for this small amplitude could be a combination of the influence of a large frictional parameter and a smaller g' than observed. The same seasonal phasing but a larger seasonal amplitude could be attained by decreasing friction, but the model becomes unstable. When compared with recent unpublished results from realistic ocean models (WOES and HYCOM simulations), the highly idealized reduced gravity model shows skill in capturing the seasonal phasing of the AC, and thus is a useful tool to investigate the influence of winds over the Southern Indian Ocean.

9.1.5 Which characteristics of Indian Ocean wind forcing predominantly influence the seasonal phasing at the western boundary?

Earlier results suggest that signals from more remote wind forcing, beyond about 65°E, do not reach the western boundary. The role of local winds and near-field winds on the AC are therefore isolated and explored. Local winds could drive seasonal upwelling and downwelling along the coast, which would in turn influence the pycnocline gradient and alter

the AC volume transport. These local winds contribute a large part to the seasonality but cannot, alone, explain the observed seasonal phasing as they lead to a November-December maximum in flow. When combined with near-field winds to the east of 35°E, however, the observed AC phasing (January-February-March maximum) is recovered. The seasonal influence of far-field winds is minor, corroborating earlier results that remote anomalies die out during their journey west due to destructive interference with overlying WSC. However, WSC forcing over the whole Indian Ocean remains important in the sense that basin-wide WSC sets up the background circulation upon which the seasonal anomalies are overlaid. Seasonal near-field winds and the mean basin-wide WSC are therefore identified as the main drivers in determining the January-February-March maximum in simulated AC transport.

9.2 Assumptions, Limitations, and Suggestions for Future Work

This study is the first attempt to understand the mechanisms behind the observed seasonality of the AC, and the findings presented here have highlighted that there is much still to be explored on the topic of seasonal variations of western boundary flows. Given the role that the AC is thought to play in influencing South Africa's climate and rainfall, improving understanding of this current's variability is a worthy avenue for future research.

9.2.1 A Smaller Amplitude of Seasonal Change

A shortcoming of this study is that using the reduced gravity model, the near-field winds are identified as being important, but the seasonal transport changes from these winds cannot explain the observed seasonal amplitude of the AC. Since the reduced gravity model becomes unstable when friction is reduced, it is not possible to reproduce a seasonal cycle of the AC where both the amplitude and phasing match observations.

9.2.2 Other Processes at Play?

There are many processes that have not been captured by the reduced gravity model, most notably the influence of thermohaline forcing. Differential heating across the current may have an important role to play in the seasonality. The logic behind this suggestion is that the AC heat budget is strongly influenced by an advective flux from the tropical Indian Ocean. However, offshore of the current towards the center of the gyre, the heat budget is more dependent on air-sea flux. This could mean that the water column offshore experiences a larger thermosteric expansion in summer than the AC, thus increasing the SSH gradient across the current and resulting in an increase in flow. This could explain why most western boundary currents, the AC (Beal and Elipot, 2016), the Florida Current (Meinen et al., 2010), the Kuroshio (Johns et al., 2001) and the East Australian Current (Ridgway and Godfrey, 1997), are all stronger during their respective hemisphere's summers. An observation that is hard to explain based on a baroclinic adjustment, given the differing widths and wind conditions of the various ocean basins. Nof (1983) examined the response of currents to atmospheric cooling using a 2-layer model and found that upon entering a region of cooling, the position of the current is altered, but there is no change in the total transport, indicating that the adjustment of currents to imposed heating or cooling does not involve a transport change (Nof, 1983). Seasonal dynamic height anomalies across the Gulf Stream were investigated by Sato and Rossby (1995), but were found to be too small to explain the amplitude of the observed seasonal transport changes of the Gulf Stream. The same may be true for the AC, as the onshore/offshore dynamic height changes could contribute a portion of the seasonal transport changes. The degree of differential heating/cooling over the AC expressed by air-sea fluxes and dynamic height changes in the core of the current versus offshore has yet to be investigated and is suggested for future research.

9.2.3 Climatological QuikSCAT Winds

The shallow water models presented in this study are only forced with climatological QuikSCAT winds. One of the limitations of the study is that a different wind product may lead to different findings. Using a variety of wind products to force the shallow water models, and the results compared and contrasted, would increase the confidence in the findings. Furthermore, the use of inter-annual winds would enable an investigation into what processes drive an excursion of the seasonal phasing from the norm in years where the AC is not at a maximum in summer and minimum in winter. This was not explored in this study and is suggested for future work.

9.2.4 AC Sensitivity to Rossby Wave Propagation Speeds in Realistic Models?

Results presented in Chapter 7 show that first order baroclinic waves play an important role in determining the seasonal phasing of the AC. A large degree of sensitivity of the simulated seasonal cycle of the AC to the propagation speeds of SLA was observed. The current is found to act like a lens integrating the influence of WSC forcing, and its seasonal phasing is therefore responsive to the arrival time of the anomalies that communicate this wind signal. This finding may act to inform why historic model studies, and more recent unpublished model results, have been unable to simulate the correct seasonal phasing of the AC. This ultra-sensitivity of the seasonal cycle to baroclinic wave parameters was not previously considered, and so investigation of this in modern realistic models may prove to be very enlightening.

9.2.5 Climate Change and Alterations in Stratification

The sensitivity of the seasonal cycle to Rossby wave propagation speeds raises questions regarding what effect modifications in ocean stratification due to climate change may have on the seasonal phasing of the AC. Fyfe and Saenko (2007) looked at how the dynamics of

Rossby waves may change in response to upper-ocean warming and the consequent alteration in density structure. Using climate model simulations of the North Pacific they found that anthropogenic warming of the upper ocean resulted in a speed up of baroclinic Rossby waves. Hypothetically, the same could apply for the Southern Indian Ocean where surface warming would act to increase the density gradient between the surface and deep ocean, and lead to a speed up of baroclinic Rossby waves. This could imply a backwards shift of the seasonal phasing of the AC as the waves communicating the WSC signal would arrive earlier on in the year. This is outside the scope of this study but is planned for further investigation.

9.3 Conclusion

The principal processes that contribute to the seasonal phasing of the AC have, to date, remained largely unknown. This study is the first of its kind to use *in-situ* observations, satellite measurements and idealized ocean models to obtain a better understanding of the drivers of the observed seasonality. While a reduced gravity model is highly idealized and has many limitations, it was able to successfully reproduce the observed seasonal phasing of the AC. Propagation speeds of Rossby waves were found to have a strong influence on seasonality at the western boundary, with the near-field winds identified as having a dominant contribution to the seasonal cycle of AC volume transport. WSC excited anomalies from far-afield were shown to dissipate before reaching the boundary due to destructive interference with overlying wind stress. Basin-wide winds are important as they set the background circulation pattern. This study demonstrates the decisive role that first order baroclinic waves communicating the WSC signal from near-field winds have on the seasonal phasing of the AC.

10 Acknowledgements

My PhD process has not been a solo adventure as I have had many companions along the way who have provided vital support and guidance. Firstly I would like to thank my four supervisors who have each, in their own way, been essential in the completion of this thesis:

Pierrick Penven for his endless patience in teaching me about models and the physics behind them, for our fun-filled conversations, and for devoting his valuable time to me whenever I asked for it.

Lisa Beal who showed me how fascinating science can be, who pushed me and kept me focused when the going got tough, and who opened up the wonderful world of RSMAS to me.

Isabelle Ansorge, my mommy in oceanography, for inspiring me in second year to become an oceanographer and for continuing to support and nurture me throughout my studies.

Juliet Hermes for her unwavering academic, financial and emotional support. For allowing me to pursue my curiosity and encouraging me to embrace opportunities in and outside of the PhD.

There have been other academics who have not been officially involved in my PhD, but who have made themselves available for teaching, listening and brainstorming, and have thus also made critical contributions. Bill Johns taught me wind driven ocean circulation, and made derivations and equations that I previously thought impossible to grasp, just make sense! My thanks goes to Bill for the many discussions and indulging me in my asking a million questions. Shane Elipot opened the world of statistics to me and clarified so many confusions. His dry wit and to-the-point comments, kept me on my mental toes. My appreciation also goes out to the IRD researchers: Steven Herbette, Stephane Pous and Julie Deshayes, for their help and insight. Julie pulled me back into the light during one of the darkest times in my PhD by helping me make sense of my results when I couldn't see the wood for the trees.

To all these brilliant academics - you taught me so much and expected so little - thank

you!

A PhD is, however, not created purely in the world of academia, but spills over into all aspects of the protagonist's life, and so I would have been useless without the support I received from my family and friends. A special acknowledgement goes to my parents; my mom, Rosa Scalabrino, for her edits, her fabulous food, and her motivating pep talks; my dad, John Hutchinson, for being my number one fan and thinking that I rock, PhD or not.

Last, but certainly not least, a big thank you to my partner Damian Weldon, for being my copy-editor, my sounding board, my hand to hold, and my anchor in the PhD storm.

As unconventional as it may be, I would like to dedicate the energy and intention with which I send this body of work forth into the world, to the memory of my Ouma, Carol Scalabrino. It is but a token of all that I was to her, and all that she was to me, but its all I have to dedicate and so I dedicate it to her.

11 Supplementary Material

11.1 Simplification of 1 1/2 Layer Reduced Gravity Model using an Analytical Rossby Wave Simulation

Chapter 7 showed that by matching baroclinic Rossby wave speeds in the model with those observed in reality, a 1 1/2 layer reduced gravity model could correctly reproduce the observed seasonal phasing of the AC. To verify that the results from the numerical reduced gravity model were not just coincidental and that capturing the correct westward travelling speed of anomalies is, in fact, important, an analytical model was developed to simulate the passage of a baroclinic Rossby wave across the Southern Indian Ocean at a latitude of 34.5°S. The idea is that this analytical model resolves the changes in sea surface height due to wind stress pumping on the ocean along the chosen line of latitude. This signal is communicated westwards by a baroclinic Rossby wave travelling at - 3.2 $km.day^{-1}$ which is the mean speed of SLA in the reduced gravity model. This analytical model also has only one active layer of density ρ, which overlays a second layer (density $\rho + \triangle\rho$) of infinite depth. The following equation contains the essential physics governing the forced propagation of baroclinic planetary waves (Qiu et al., 1997; Fyfe and Saenko, 2007):

$$\frac{\partial H}{\partial t} - Cr_1 \frac{\partial H}{\partial x} = -We - RH \tag{28}$$

where H is the thickness of the active layer, Cr_1 is the Rossby wave propagation speed, R is the Rayleigh friction coefficient and We is the Ekman pumping given by:

$$We = \nabla \times \left(\frac{\vec{\tau}_{(x,y)}}{\rho_o f} \right) \tag{29}$$

where $\vec{\tau}(x, y)$ is the surface wind stress, ρ_o is the mean density of the water column and f is planetary vorticity. Equation 28 can be solved analytically at each latitude interval at every point in time to describe the evolution of the active layer in response to wind forcing (Capotondi and Alexander, 2001; Capotondi et al., 2003):

$$H(x,t) = H(x_e, t-t_e)e^{-Rt_e} + \int_{x_e}^{x} \left[\left(\frac{We(\xi, t-t_\xi)}{Cr_1(\xi)} \right) e^{-Rt_\xi} \right] d\xi \tag{30}$$

The first term on the right hand side of the equation, $H(x_e, t-t_e)e^{-Rt_e}$ describes the contribution of waves generated at the eastern boundary (point x_e) reaching point x after transit time t_e. The magnitude of influence of these waves on the thickness of the active layer, H, at point x is eroded by friction, R. The second term on the right hand side describes the contribution of the waves generated by historic Ekman pumping or suction at all latitude points to the east of point x, with the location of these points described using ξ. $t - t_\xi$ thus describes lag time for waves at all points to the east of x, position denoted by ξ, to reach x. The magnitudes of these Ekman pumping generated waves are also exponentially reduced by friction as they travel westwards across the basin. According to Fyfe and Saenko (2007), Cr_1 can be considered independent of longitude in this idealized analytical model. Cr_1 therefore represents the mean value of Rossby wave propagation speed at the latitude for which the analytical model is run for.

An analytical model, based on Equation 30 describing the westward propagation of a Rossby wave, was coded for the latitude of 34.5°S (mean latitude of the ACT array). Climatological QuikSCAT wind stress at 34.5°S is used as forcing, and Cr_1, is set to -3.2 $km.day^{-1}$. It is important to note that this model is a pure analytical solution to an excitement of the first baroclinic mode by climatological winds. The model only resolves the sea surface height changes along one line of latitude. The adjustment of the western boudnary current at this latitude is considered via the rigid lid approximation. Mass cannot accumulate in the Indian Ocean basin and so the western boundary must respond rapidly to these changes in sea surface height gradient caused by the westward propagation of a first baroclinic mode wave. In reality, barotropic waves rapidly communicate this signal, here an instantaneous adjustment is assumed. This model is useful in providing a simplified scenario for the propagation of a baroclinic Rossby wave across the Southern Indian Ocean and the resultant implied transport changes at the western boundary. The analytical simulation thus concatenates the affect of wind forcing over the Southern Indian Ocean exciting a first baroclinic mode Rossby wave,

and the immediate response of the western boundary via an assumed barotropic adjustment in order to conserve mass. The major limitation of this model is that it only takes wind stress forcing at the mean latitude of the ACT line (34.5°S) into account and thus does not resolve the influence of winds over the whole basin on the western boundary variability. There is no background forcing and there are no boundary waves. The aim here is to investigate purely zonal adjustment to winds along one line of latitude.

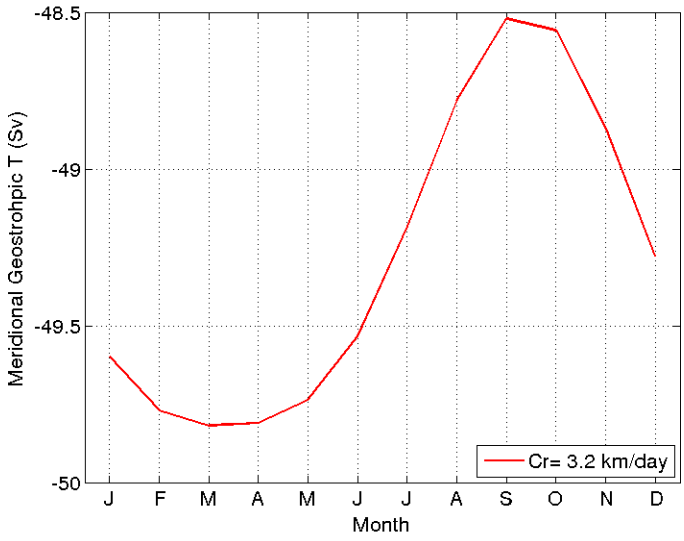

Figure 11.1: *Implied seasonal cycle at western boundary from analytical Rossby wave model run at 34.5°S*

The resultant seasonal cycle of the implied western boundary flow (Figure 11.1) is at a maximum in March and a minimum in September, agreeing well with *in-situ* observations. This seasonal phasing is close to that of the reduced gravity model run in ROMS, but is shifted a month later in the year (Figure 8.1a). Discrepancies in the seasonal phasings of the two simulations may be due to the fact that the analytical model resolves only the southward flow at 34.5°S not the south-westward flow perpendicular to the ACT line, and that the phase speed of the simulated Rossby wave propagation is fixed throughout the ocean basin. The amplitude of seasonal change shown in Figure 11.1 is small at 1.3 Sv, similar to the amplitude observed in the reduced gravity model run using ROMS.

The overall agreement in phasing between the numerical reduced gravity model and the analytical Rossby wave model supports the conclusions of Chapter 7 that a first baroclinic adjustment of the Southern Indian Ocean to seasonal wind forcing can explain the observed seasonal phasing of the western boundary flow. The Rossby wave model shows that a summertime maximum and wintertime minimum in Agulhas Current southward meridional transport can be obtained by forcing the Southern Indian Ocean at 34.5°S with climatological winds and simulating the passage of Rossby wave possessing a propagation speed of -3.2 $km.day^{-1}$. These results act to validate the findings from the reduced gravity model run and encourage confidence in this simulation being utilized for further testing.

12 Appendix

12.1 Supplementary Figures

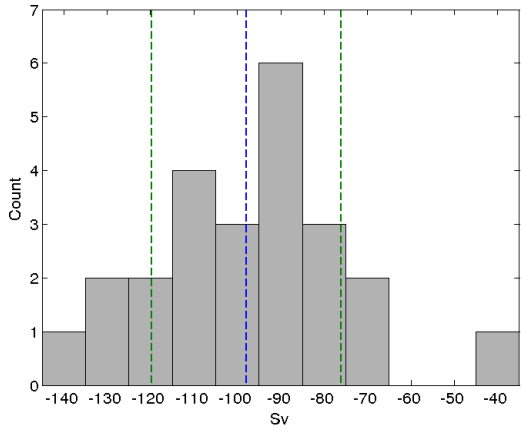

Figure 12.1: *Histogram showing number of years in each transport bin for the month of March. The 23 year mean transport (Sv), and one standard deviation from the mean, are shown in blue and green respectively.*

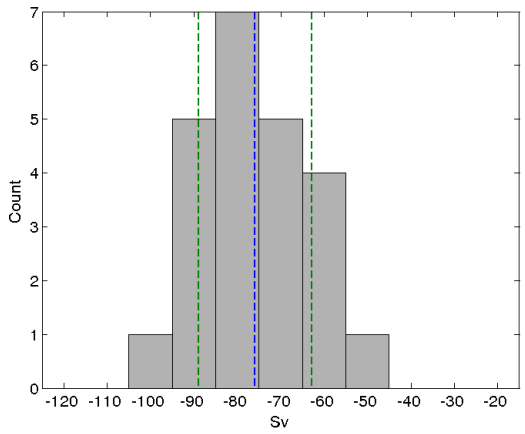

Figure 12.2: *Histogram showing number of years in each transport bin for the month of July. The 23-year mean transport (Sv), and one standard deviation from the mean, are shown in blue and green respectively.*

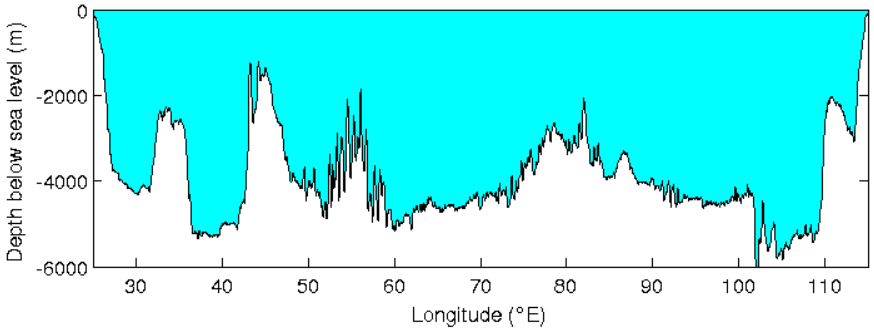

Figure 12.3: *Depth of topographical features below sea level (m) across the Southern Indian Ocean at the mean latitude of the Agulhas Current Time-series array (34.5°S).*

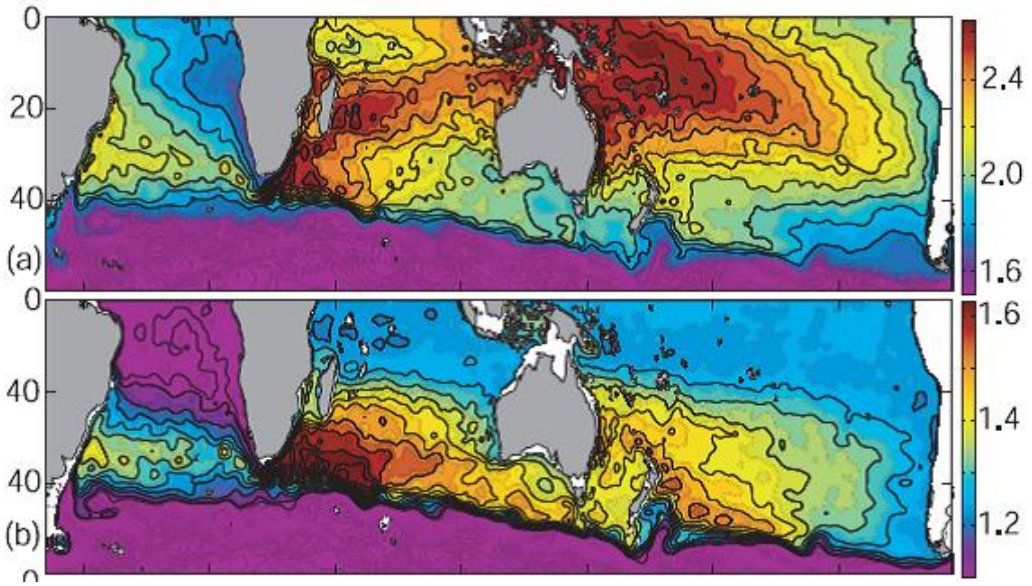

Figure 12.4: *Map showing steric height of Pacific-Indian inter-basin qyre system for a) the surface referenced to 2000 m, and b) the integrated thermocline (400 m) referenced to 2000 m. From Ridgway (2007)*

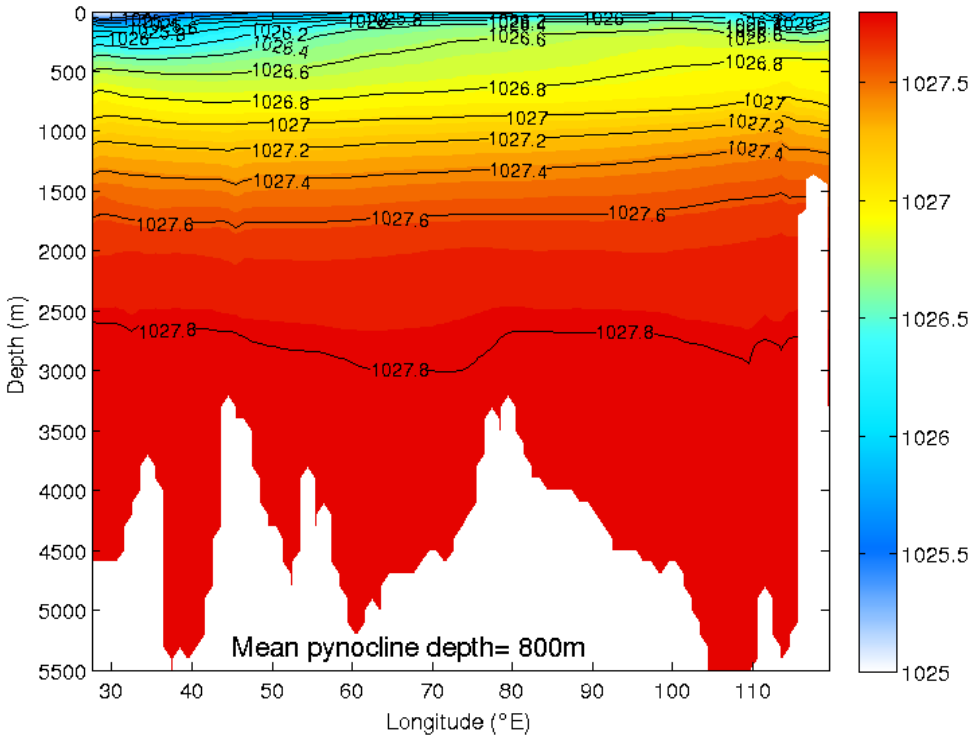

Figure 12.5: *Cross section of density ($kg.m^{-3}$) from the World Ocean Circulation Experiment (WOCE) averaged over the ACT latitude range. The mean pycnocline depth is reported*

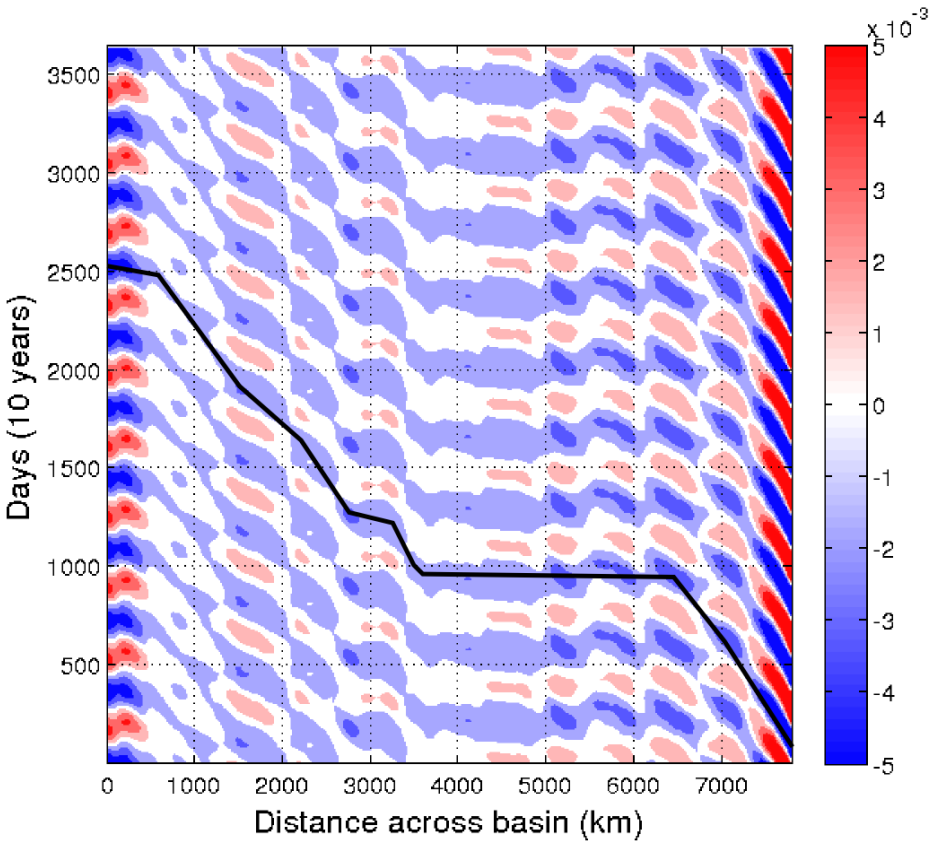

Figure 12.6: *Hovmöller plot showing the propagation of sea level anomalies (SLA, m) across the basin at the mean latitude of the ACT line during the final 10 years of simulation with the x axis as distance from the western boundary. The black line tracks the propagation of an anomaly across the basin in order to estimate the average phase speed.*

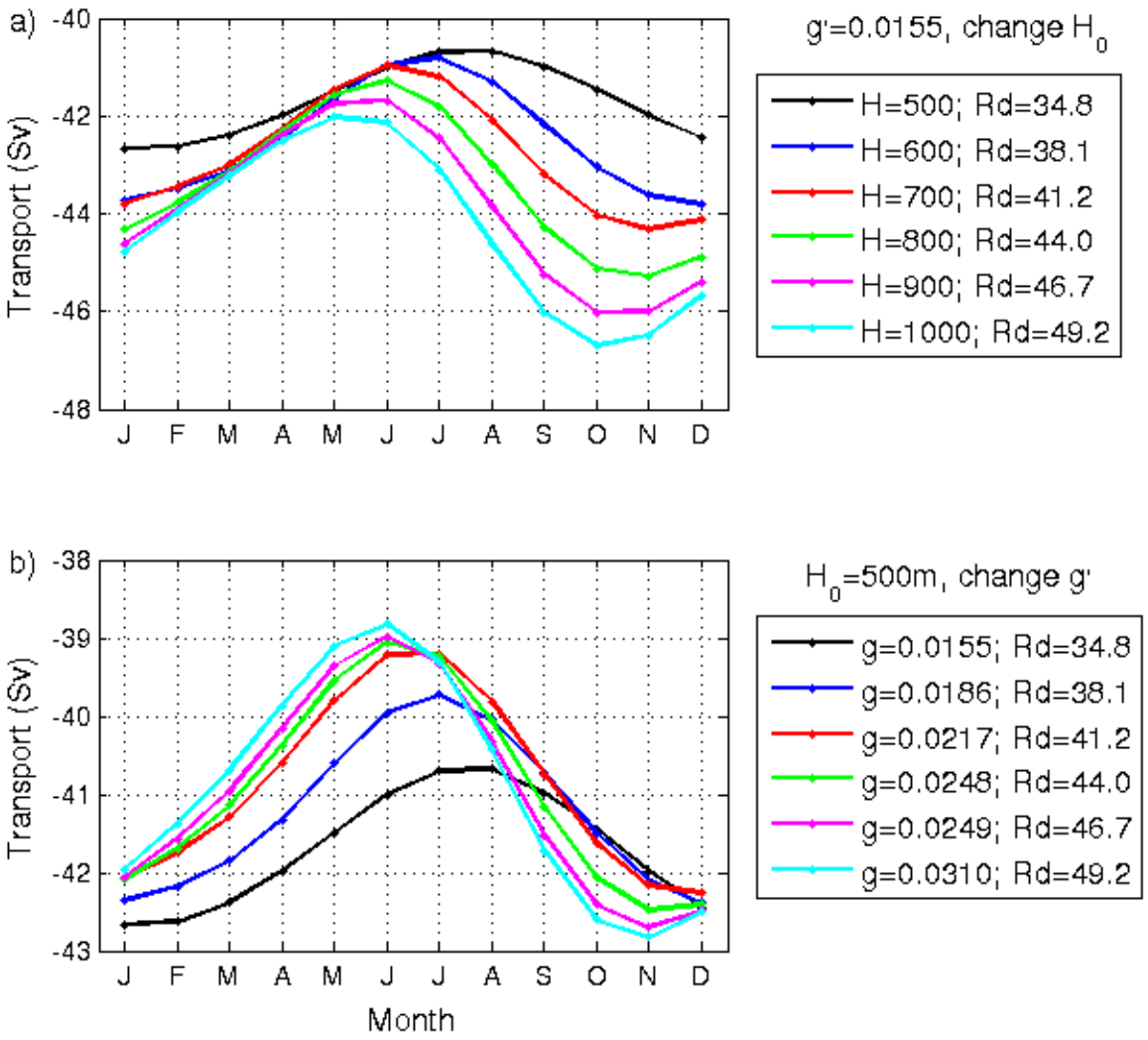

Figure 12.7: *Plots showing similar sensitivity of the phase and amplitude of the seasonal cycle in volume transport (Sv) at a hypothetical ACT line to alternative baseline reduced gravity parameters g' and H_o to those presented in Chapter 7). A change in the density gradient between the two layers in the model is expressed in g' and a change in the active layer depth is described by H_0. In plot a) g' is set at 0.0155 $m.s^{-2}$ and H_o is increased in 100 m increments. The resultant alterations in Rossby radius of deformation are shown in the legend. In plot b) H_o is set at 500 m and g' is increased so that the alterations in the radius of deformation match those shown in plot (a).*

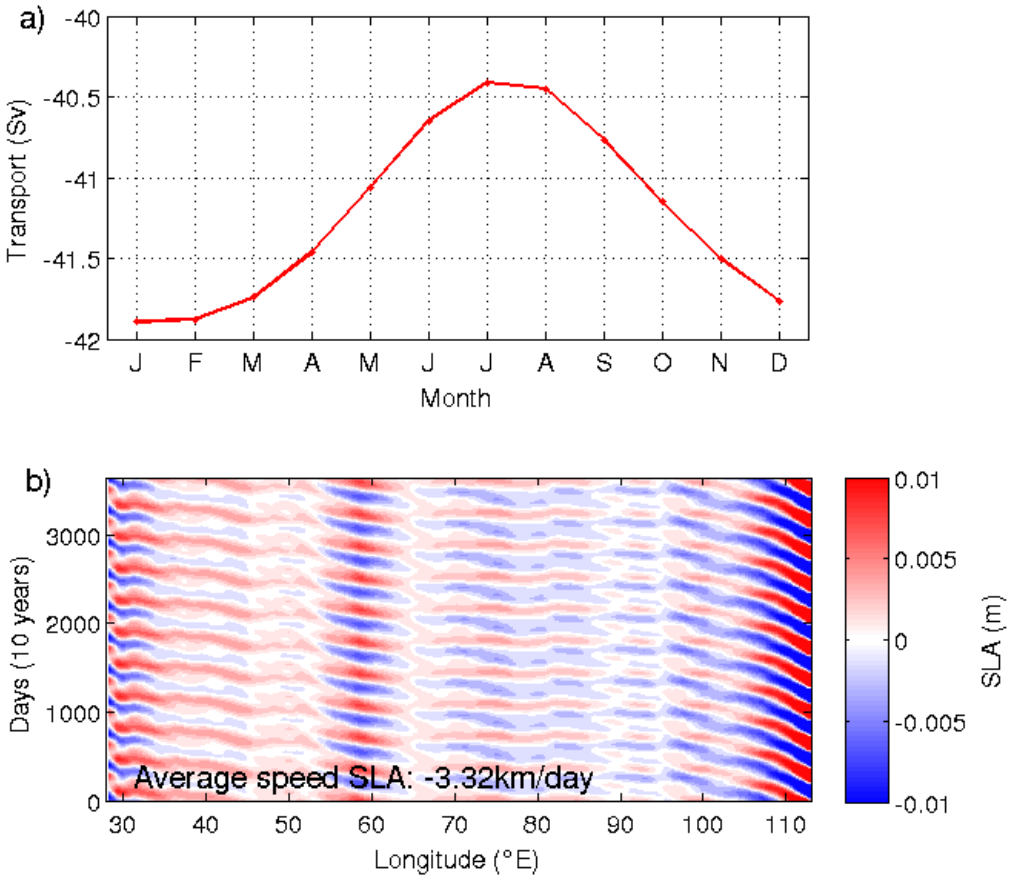

Figure 12.8: *a) Seasonal cycle of Agulhas Current in model simulation initiated with a thermocline depth of 500 m and* $g' = 0.0155\ m.s^{-2}$*. The flow is south-westward, therefore more negative values correspond to a stronger current. b) Hovmöller plot showing the propagation of sea level anomalies (SLA, m) across the basin at the mean latitude of the ACT line during the final 10 years of simulation. The mean propagation speed is printed at the base of the plot*

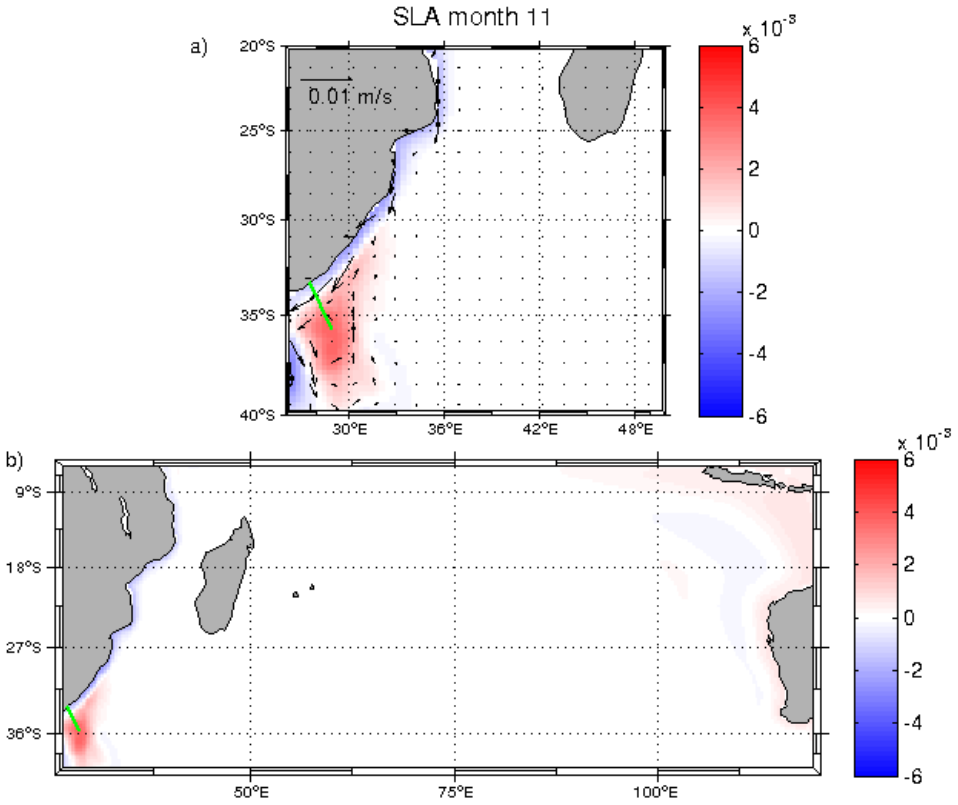

Figure 12.9: *Sea level anomalies (SLA, m) for November for run forced with seasonally varying local wind only. a) Zoom in of western boundary SLA with vectors of anomalies in circulation overlaid. b) Basin-wide SLA.*

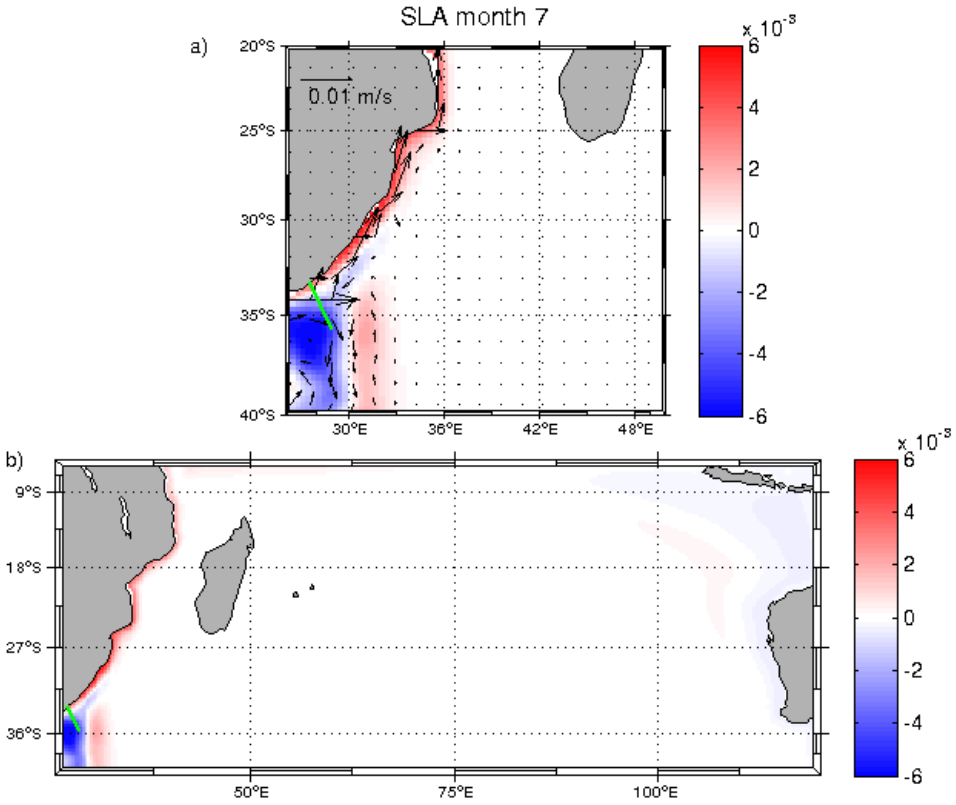

Figure 12.10: *Sea level anomalies (SLA, m) for July for run forced with seasonally varying local wind only. a) Zoom in of western boundary SLA with vectors of anomalies in circulation overlaid. b) Basin-wide SLA.*

12.2 Derivations

12.2.1 Potential Vorticity

Vorticity (ς) is the curl of velocity:

$$\varsigma = \nabla(\vec{v}) = \frac{\partial v}{\partial x} - \frac{\partial u}{\partial y} \tag{31}$$

Vorticity that results from the shear of the local fluid flow is called the relative vorticity (δ) as it describes the spin of a fluid parcel relative to the earth's surface.

Everything on earth also has planetary vorticity (f), which is twice the rotation rate of the planet.

$$f = 2\Omega sin\theta \tag{32}$$

The sum and relative and planetary vorticities ($\delta + f$) is known as the absolute vorticity.

To derive the equation describing potential vorticity, start with the momentum equations:

$$\frac{\partial u}{\partial t} + u\frac{\partial u}{\partial x} + v\frac{\partial u}{\partial y} + w\frac{\partial u}{\partial z} - fv = -\frac{1}{\rho}\frac{\partial P}{\partial x} \tag{33}$$

$$\frac{\partial v}{\partial t} + u\frac{\partial v}{\partial x} + v\frac{\partial v}{\partial y} + w\frac{\partial v}{\partial z} + fu = -\frac{1}{\rho}\frac{\partial P}{\partial y} \tag{34}$$

Assume that the density terms are small and frictional terms can similarly be neglected. Cross differentiating equations (34) and (35) gives:

$$\frac{D}{Dt}\left(\frac{\partial v}{\partial x} - \frac{\partial u}{\partial y}\right) + \left(\frac{\partial u}{\partial x} + \frac{\partial v}{\partial y}\right)\left(\frac{\partial v}{\partial x} - \frac{\partial u}{\partial y}\right) + \left(\frac{\partial w}{\partial x}\frac{\partial v}{\partial z}\right) - \left(\frac{\partial w}{\partial y}\frac{\partial u}{\partial z}\right) + f\left(\frac{\partial u}{\partial x} + \frac{\partial v}{\partial y}\right) + v\frac{\partial f}{\partial y} = 0 \tag{35}$$

The "tilting terms" $\left(\frac{\partial w}{\partial x}\frac{\partial v}{\partial z}\right) - \left(\frac{\partial w}{\partial y}\frac{\partial u}{\partial z}\right)$ are small and can therefore be ignored.

Substituting relative vorticity δ for $\frac{\partial v}{\partial x} - \frac{\partial u}{\partial y}$ gives:

$$\frac{D\delta}{Dt} + \left(\frac{\partial u}{\partial x} + \frac{\partial v}{\partial y}\right)(\delta + f) + v\frac{\partial f}{\partial y} = 0 \tag{36}$$

Substitute $\frac{\partial u}{\partial x} + \frac{\partial v}{\partial y}$ for $-\frac{\partial w}{\partial z}$ according to the continuity equation:

$$\frac{D\delta}{Dt} + \left(-\frac{\partial w}{\partial z}\right)(\delta + f) + v\frac{\partial f}{\partial y} = 0 \tag{37}$$

$\frac{\partial f}{\partial y}$ can be replaced by $\frac{Df}{Dt}$ as the coriolis force does not change with time, longitude or depth.

This then gives the vorticity equation:

$$\frac{D}{Dt}(\delta + f) - \frac{\partial w}{\partial z}(\delta + f) = 0 \tag{38}$$

By integrating the continuity equation $\frac{\partial u}{\partial x} + \frac{\partial v}{\partial y} = -\frac{\partial w}{\partial z}$ over a water column of height H, $\frac{\partial w}{\partial z}$ can be replaced by $\frac{1}{H}\frac{\partial H}{\partial t}$, to give the equation for potential vorticity:

$$\frac{D}{Dt}\left(\frac{f + \delta}{H}\right) = 0 \tag{39}$$

This equation states that the change in potential vorticity over time is zero, and thus $\left(\frac{f+\delta}{H}\right)$must remain constant.

12.2.2 Sverdrup Balance

To derive the Sverdrup Balance one must start by looking at the geostrophic interior and the frictional boundary layer separately, and then combine the two regimes.

Start with the geostrophic equations:

$$-fv = -\frac{1}{\rho}\frac{\partial P}{\partial x} \tag{40}$$

$$fu = -\frac{1}{\rho}\frac{\partial P}{\partial y} \tag{41}$$

Cross differentiate and subtract $\frac{\partial(41)}{\partial x} - \frac{\partial(40)}{\partial y}$ gives:

$$(3)f\frac{\partial u}{\partial x} + u\frac{\partial f}{\partial x} + f\frac{\partial v}{\partial y} + v\frac{\partial f}{\partial y} = 0 \tag{42}$$

The variation of the coriolis parameter with longitude $\frac{\partial f}{\partial x}$ is zero and the variations of coriolis with latitude $\frac{\partial f}{\partial y}$ is known as β. The equation therefore becomes:

$$f\left(\frac{\partial u}{\partial x}+\frac{\partial v}{\partial y}\right)+\beta v=0 \tag{43}$$

Substitute $\frac{\partial u}{\partial x}+\frac{\partial v}{\partial y}$ for $-\frac{\partial w}{\partial z}$ according to the continuity equation:

$$f\left(\frac{\partial w}{\partial z}\right)=\beta v \tag{44}$$

This is known as the geostrophic vorticity equation where the divergence of the flow is shown to be proportional to its meridional velocity. Vertically integrating (5) gives:

$$\int_{zbottom}^{ztop}\beta v\ \mathrm{d}z=\int_{zbttom}^{ztop}f\frac{\partial w}{\partial z}\ \mathrm{d}z \tag{45}$$

Boundary conditions specify that $W(z_{bottom})=0$ and $W(z_{top})=W_{top}$.

In addition, the depth integral of the meridional velocity, $\int v\partial z$, can be replaced with the symbol $\overline{V}$ so that equation (6) becomes:

$$\beta\overline{V}=fW_{top} \tag{46}$$

This states that the depth integrated meridional transport ($\tilde{\mathrm{V}}$) is proportional to the vertical velocity at the top of the geostrophic layer.

Now focus on the surface boundary layer, the Ekman layer.

Start with the geostrophic equations for the wind driven Ekman layer:

$$-fv=\frac{1}{\rho}\frac{\partial\tau_x}{\partial z} \tag{47}$$

$$fu=\frac{1}{\rho}\frac{\partial\tau_y}{\partial z} \tag{48}$$

Cross differentiate and subtract $\frac{\partial(49)}{\partial x}-\frac{\partial(48)}{\partial y}$ gives:

$$-f\frac{\partial w}{\partial z}+\beta v=\frac{1}{\rho}\frac{\partial}{\partial z}\left(\frac{\partial\tau_y}{\partial x}-\frac{\partial\tau_x}{\partial y}\right) \tag{49}$$

The notation $\nabla \times \tau$ can be used instead of $\frac{\partial \tau_y}{\partial x} - \frac{\partial \tau_x}{\partial y}$. Now vertically integrate over the depth of the Ekman later with boundary conditions $W(z_0) = 0$ and $W(z_{Ekman}) = W_{Ekman}$.

$$\int_{zekman}^{0} -f \frac{\partial w}{\partial z} \, \mathrm{d}z + \int_{zekman}^{0} \beta v \, \mathrm{d}z = \frac{1}{\rho} \int_{zekman}^{0} \frac{\partial}{\partial z} \left(\nabla \times \tau \right) \, \mathrm{d}z \tag{50}$$

Which becomes

$$-f(0 - W_{Ek}) - \beta V_{Ek} = \frac{1}{\rho} \left(\nabla \times \tau \right) \tag{51}$$

Away from equatorial regions β is much smaller than f, and so therefore for most of the ocean βV_{Ek} is negligible. This gives:

$$f W_{Ek} = \frac{1}{\rho} \nabla \times \tau \tag{52}$$

This equation shows that the vertical velocity at the base of the wind driven Ekman layer is directly proportional to the wind stress curl.

Now combine equations 46 and 52, as the vertical velocity at the top of the geostrophic layer is equal to the vertical velocity at the base of the Ekman layer $W_{Ek} = W_{top}$.

$$\overline{V} = \frac{1}{\beta \rho} \nabla \times \tau \tag{53}$$

This is the Sverdrup Balance. It states that the vertically integrated meridional velocity ($\overline{V}$) is proportional to the wind stress curl. This equation is appropriate for use in regions where the flow is steady and frictionless below the Ekman layer, and the sea floor is flat.

12.2.3 Topographic Sverdrup Relation

The Sverdrup Balance (Equation 1) assumes a flat bottom. Barotropic waves are, however, sensitive to topography and so a topographic Sverdup equation is needed to describe this adjustment process. This will be developed here following the work of Mellor and Huang (1997) and Pedlosky (1971).

Commence with the momentum equations assuming no bottom stress:

$$-fv = -\frac{1}{\rho}\frac{\partial P}{\partial x} + \frac{\partial \tau^x}{\rho H} \tag{54}$$

$$fu = -\frac{1}{\rho}\frac{\partial P}{\partial y} + \frac{\partial \tau^y}{\rho H} \tag{55}$$

Cross differentiate and subtract gives:

$$f\frac{\partial u}{\partial x} + u\frac{df}{dx} + f\frac{\partial v}{\partial y} + v\frac{\partial f}{\partial y} = \frac{1}{\rho}\left[\frac{1}{H}\left(\vec{\nabla}\times\vec{\tau}\right) + \frac{1}{H^2}\left(\tau^x\frac{\partial H}{\partial y} - \tau^y\frac{\partial H}{\partial x}\right)\right] \tag{56}$$

Put in terms of mass transport, i.e. $U = \rho H u$; $u = \frac{U}{\rho H}$ and $V = \rho H v$; $v = \frac{V}{\rho H}$

$$\frac{f}{\rho}\left[\frac{\partial}{\partial x}\left(\frac{U}{H}\right) + \frac{\partial}{\partial y}\left(\frac{V}{H}\right)\right] + \frac{\beta V}{\rho H} = \frac{1}{\rho}\left[\frac{1}{H}\left(\vec{\nabla}\times\vec{\tau}\right) + \frac{1}{H^2}\left(\tau^x\frac{\partial H}{\partial y} - \tau^y\frac{\partial H}{\partial x}\right)\right] \tag{57}$$

Which then becomes:

$$\frac{f}{H}\left(\frac{\partial U}{\partial x} + \frac{\partial V}{dy}\right) - \frac{f}{H^2}\left(U\frac{\partial H}{\partial x} + V\frac{\partial H}{\partial y}\right) + \frac{\beta V}{H} = \frac{1}{H}\left(\vec{\nabla}\times\vec{\tau}\right) + \frac{1}{H^2}\left(\tau^x\frac{\partial H}{\partial y} - \tau^y\frac{\partial H}{\partial x}\right) \tag{58}$$

Following the continuity equation $\frac{\partial U}{\partial x} + \frac{\partial V}{dy} = 0$ and the above equation becomes:

$$\beta V - \frac{f}{H}\left(\overrightarrow{U}.\overrightarrow{\nabla}H\right) = \left(\vec{\nabla}\times\vec{\tau}\right) + \frac{1}{H}\left(\tau^x\frac{\partial H}{\partial y} - \tau^y\frac{\partial H}{\partial x}\right) \tag{59}$$

Recall that the vertically integrated meridional velocity:

$$V = \int_H^0 \rho v dz = \rho H v \tag{60}$$

is directly proportional to the wind stress curl by the Sverdrup Balance:

$$\beta V = \left(\vec{\nabla}\times\vec{\tau}\right) \tag{61}$$

So Equation 59 then simplifies to:

$$\overrightarrow{U}.\overrightarrow{\nabla}\left(\frac{f}{H}\right) = \overrightarrow{\nabla}\times\left(\frac{\tau}{H}\right) \tag{62}$$

13 Bibliography

References

Alory, G., S. Wijffels, and G. Meyers

2007. Observed temperature trends in the Indian Ocean over 1960-1999 and associated mechanisms. *Geophysical Research Letters*, 34(2).

Anderson, D. L. T. and R. A. Corry

1985. Ocean response to low frequency wind forcing with application to the seasonal variation in the Florida Straits-Gulf Stream transport. *Progress in Oceanography*, 14(1977):7–40.

Ansorge, I. J. and J. R. E. Lutjeharms

2007. The cetacean environment off southern Africa. *Whales and Dolphins of the Southern African Subregion (PB Best).Cambridge University Press, Cape Town, South Africa*, Pp. 5–13.

Atkinson, C. P., H. L. Bryden, J. J. M. Hirschi, and T. Kanzow

2010. On the seasonal cycles and variability of Florida Straits, Ekman and Sverdrup transports at 26N in the Atlantic Ocean. *Ocean Science*, 6(4):837–859.

Backeberg, B., F. Counillon, J. Johannessen, and M.-I. Pujol

2014. Assimilating along-track SLA data using the EnOI in an eddy resolving model of the Agulhas system. *Ocean Dynamics*, 64(8):1121–1136.

Backeberg, B. C., J. A. Johannessen, L. Bertino, and C. J. Reason

2008. The greater Agulhas Current system: An integrated study of its mesoscale variability. *Journal of Operational Oceanography*, 1(1):29–44.

Baquero-Bernal, A. and M. Latif

2005. Wind-Driven Oceanic Rossby Waves in the Tropical South Indian Ocean with and without an Active ENSO. *Journal of Physical Oceanography*, 35(5):729–746.

2327 Baringer, M. O. and J. C. Larsen
2328 2001. Sixteen years of Florida Current transport at 27 N. *Geophysical Research Letters*,
2329 28(16):3179–3182.

2330 Beal, L. M.
2331 2009. A time series of Agulhas Undercurrent transport. *Journal of Physical Oceanography*,
2332 39(10):2436–2450.

2333 Beal, L. M., W. P. M. De Ruijter, A. Biastoch, and R. Zahn
2334 2011. On the role of the Agulhas system in ocean circulation and climate. *Nature*,
2335 472(7344):429–436.

2336 Beal, L. M. and S. Elipot
2337 2016. Broadening not strengthening of the Agulhas Current since the early 1990s. *Nature*.

2338 Beal, L. M., S. Elipot, A. Houk, and G. M. Leber
2339 2015. Capturing the Transport Variability of a Western Boundary Jet Results from
2340 the Agulhas Current Timeseries Experiment (ACT). *Journal of Physical Oceanography*,
2341 45(5):1302–1324.

2342 Beal, L. M., J. M. Hummon, E. Williams, O. B. Brown, W. Baringer, and E. J. Kearns
2343 2008. Five years of Florida current structure and transport from the Royal Caribbean
2344 cruise ship explorer of the Seas. *Journal of Geophysical Research: Oceans*, 113(6):1–11.

2345 Beckley, L. E.
2346 1995. The Agulhas Current ecosystem with particular reference to dispersal of fish larvae.
2347 *In Status and future of large marine ecosystems of the Indian Ocean. A report of an*
2348 *international symposium and workshop.*

2349 Biastoch, A., C. J. C. Reason, J. R. E. Lutjeharms, and O. Boebel
2350 1999. The importance of flow in the Mozambique Channel to seasonality in the greater
2351 Agulhas Current system. *Geophysical Research Letters*, 26(21):3321–3324.

Braby, L., B. C. Backeberg, I. Ansorge, M. J. Roberts, M. Krug, and C. J. C. Reason
2016. Observed eddy dissipation in the Agulhas Current. *Geophysical Research Letters*, 43(15):8143–8150.

Bryden, H. L. and L. M. Beal
2001. Role of the Agulhas Current in Indian Ocean circulation and associated heat and freshwater fluxes. *Deep Sea Research Part I: Oceanographic Research Papers*, 48(8):1821–1845.

Bryden, H. L., L. M. Beal, and L. M. Duncan
2005. Structure and transport of the Agulhas Current and its temporal variability. *Journal of Oceanography*, 61(3):479–492.

Capotondi, A. and M. A. Alexander
2001. Rossby Waves in the Tropical North Pacific and Their Role in Decadal Thermocline Variability. *Journal of Physical Oceanography*, 31(12):3496–3515.

Capotondi, A., M. A. Alexander, and C. Deser
2003. Why are there Rossby wave maxima in the Pacific at 10 degrees S and 13 degrees N? *Journal of Physical Oceanography*, 33(8):1549–1563.

Casal, T. G. D., L. M. Beal, R. Lumpkin, and W. E. Johns
2009. Structure and downstream evolution of the Agulhas Current system during a quasi synoptic survey in February to March 2003. *Journal of Geophysical Research: Oceans*, 114(C3).

Chassignet, E. P. and D. B. Boudra
1988. Dynamics of Agulhas retroflection and ring formation in a numerical model. Part II. Energetics and ring formation. *Journal of Physical Oceanography*, 18(2):304–319.

Chelton, B. and M. G. Schlax
1996. Global Observation of Oceanic Rossby Wavesdf.

Chelton, D. B., R. A. DeSzoeke, M. G. Schlax, K. El Naggar, and N. Siwertz
1998. Geographical Variability of the First Baroclinic Rossby Radius of Deformation. *J Phys Oceanogr*, 28(3):433–460.

Chelton, D. B., M. H. Freilich, J. M. Sienkiewicz, and J. M. Von Ahn
2006. On the use of QuikSCAT scatterometer measurements of surface winds for marine weather prediction. *Monthly Weather Review*, 134(8):2055–2071.

Chelton, D. B., M. G. Schlax, R. M. Samelson, and R. A. de Szoeke
2007. Global observations of large oceanic eddies. *Geophysical Research Letters*, 34(15).

Cipollini, P., G. D. Quartly, P. G. Challenor, D. Cromwell, and I. S. Robinson
2006. Remote sensing of extra-equatorial planetary waves. In *American Society for Photogrammetry and Remote Sensing*. American Society for Photogrammetry and Remote Sensing.

Cipollini, P., A. C. S. Sutcliffe, and I. S. Robinson
2010. Oceanic planetary waves and eddies: a privileged view from satellite altimetry. In *Oceanography from Space*, Pp. 195–209. Springer.

Clarke, R.
1992. World Ocean Circulation Experiment. *National Aeronautics and Space Administration*.

Collins, C., C. J. C. Reason, and J. C. Hermes
2012. Scatterometer and reanalysis wind products over the western tropical Indian Ocean. *Journal of Geophysical Research: Oceans*, 117(3):1–16.

Cummins, P. F. P. F., L. A. Mysak, and K. Hamilton
1986. Generation of Annual Rossby Waves in the North Pacific by the Wind Stress Curl.

Czeschel, L., C. Eden, and R. J. Greatbatch
2012. On the Driving Mechanism of the Annual Cycle of the Florida Current Transport. *J Phys Oceanogr*, 42(5):824–839.

2403 De La Rosa, S., P. Cipollini, and H. M. Snaith
2404 2007. An application of the Radon transform to study planetary waves in the Indian
2405 Ocean. In *SP-636, ESA Envisat Symposium, Montreux*.

2406 de Ruijter, W. P. M., H. Ridderinkhof, J. R. E. Lutjeharms, M. W. Schouten, and C. Veth
2407 2002. Observations of the flow in the Mozambique Channel. *Geophysical Research Letters*,
2408 29(10).

2409 de Ruijter, W. P. M., P. J. van Leeuwen, and J. R. E. Lutjeharms
2410 1999. Generation and evolution of Natal Pulses: solitary meanders in the Agulhas Current.
2411 *Journal of Physical Oceanography*, 29(12):3043–3055.

2412 Dee, D. P., S. M. Uppala, A. J. Simmons, P. Berrisford, P. Poli, S. Kobayashi, U. Andrae,
2413 M. A. Balmaseda, G. Balsamo, and P. Bauer
2414 2011. The ERA-Interim reanalysis: Configuration and performance of the data assimila-
2415 tion system. *Quarterly Journal of the Royal Meteorological Society*, 137(656):553–597.

2416 DiNezio, P. N., L. J. Gramer, W. E. Johns, C. S. Meinen, and M. O. Baringer
2417 2009. Observed interannual variability of the Florida Current: Wind forcing and the North
2418 Atlantic Oscillation. *Journal of Physical Oceanography*, 39(3):721–736.

2419 Domingues, R., M. Baringer, and G. Goni
2420 2016. Remote sources for year to year changes in the seasonality of the Florida Current
2421 transport. *Journal of Geophysical Research: Oceans*, 121(10):7547–7559.

2422 Durgadoo, J. V., S. Rühs, A. Biastoch, and C. W. B. Böning
2423 2017. Indian Ocean sources of Agulhas leakage. *Journal of Geophysical Research: Oceans*,
2424 122(4):3481–3499.

2425 Elipot, S. and L. M. Beal
2426 2015. Characteristics, Energetics, and Origins of Agulhas Current Meanders and Their
2427 Limited Influence on Ring Shedding. *Journal of Physical Oceanography*, 45(9):2294–2314.

ETOPO2

2006. 2-minute Gridded Global Relief Data (ETOPO2) v2.

Ferrari, R. and C. Wunsch

2008. Ocean Circulation Kinetic Energy: Reservoirs, Sources, and Sinks. *Annual Review of Fluid Mechanics*, 41(1):253.

Ffield, A., J. Toole, and D. Wilson

1997. Seasonal circulation in the south Indian Ocean. *Geophysical Research Letters*, 24(22):2773.

Fu, L.-L. and B. Qiu

2002. Low-frequency variability of the North Pacific Ocean: The roles of boundary- and wind-driven baroclinic Rossby waves. *Journal of Geophysical Research: Oceans*, 107(C12):3220.

Fu, L.-L., J. Vazquez, and M. E. Parke

1987. Seasonal variability of the Gulf Stream from satellite altimetry. *Journal of Geophysical Research: Oceans*, 92(C1):749–754.

Fyfe, J. C. and O. A. Saenko

2007. Anthropogenic speed up of oceanic planetary waves. *Geophysical Research Letters*, 34(10):12–15.

Gill, A. E.

1982. *Ocean-atmosphere dynamics*, volume 30. Academic press.

Gill, A. E. and P. P. Niller

1973. The theory of the seasonal variability in the ocean. In *Deep Sea Research and Oceanographic Abstracts*, volume 20. Elsevier.

Gordon, A. L.

1985. Indian-atlantic transfer of thermocline water at the agulhas retroflection. *Science (New York, N.Y.)*, 227(4690):1030–1033.

Gregg, M. C.

1987. Diapycnal mixing in the thermocline: A review. *Journal of Geophysical Research: Oceans*, 92(C5):5249–5286.

Grundlingh, M. L.

1980. On the volume transport of the Agulhas Current. *Deep Sea Research Part A.Oceanographic Research Papers*, 27(7):557–563.

Hermes, J. C. and C. J. C. Reason

2008. Annual cycle of the South Indian Ocean (Seychelles-Chagos) thermocline ridge in a regional ocean model. *Journal of Geophysical Research: Oceans*, 113(4):1–10.

Hermes, J. C. and C. J. C. Reason

2009. The sensitivity of the seychelles-chagos thermocline ridge to large-scale wind anomalies. *ICES Journal of Marine Science*, 66(7):1455–1466.

Hogg, N. G. and W. E. Johns

1995. Western boundary currents. *Reviews of Geophysics*, 33(S2):1311–1334.

Holbrook, N. J. and N. L. Bindoff

1997. Interannual and decadal temperature variability in the southwest Pacific Ocean between 1955 and 1988. *Journal of Climate*, 10(5):1035–1049.

Imawaki, S., A. S. Bower, L. Beal, and B. Qiu

2013. Western boundary currents. *Ocean circulation and climate-a 21st century perspective, 2nd edn, Academic Press, London*, Pp. 305–338.

Johns, W. E., T. N. Lee, D. Zhang, R. Zantopp, C.-T. Liu, and Y. Yang

2001. The Kuroshio east of Taiwan: Moored transport observations from the WOCE PCM-1 array. *Journal of Physical Oceanography*, 31(4):1031–1053.

Johns, W. E., T. J. Shay, J. M. Bane, and D. R. Watts

1995. Gulf Stream structure, transport, and recirculation near 68 W. *Journal of Geophysical Research: Oceans*, 100(C1):817–838.

Kalnay, E., M. Kanamitsu, R. Kistler, W. Collins, D. Deaven, L. Gandin, M. Iredell, S. Saha, G. White, and J. Woollen
1996. The NCEP/NCAR 40-year reanalysis project. *Bulletin of the American Meteorological Society*, 77(3):437–471.

Kennelly, M., K. Tracey, and D. R. Watts
2007. Inverted echo sounder data. *Processing manual*.

Kessler, W. S. and L. Gourdeau
2007. The Annual Cycle of Circulation of the Southwest Subtropical Pacific, Analyzed in an Ocean GCM*. *Journal of Physical Oceanography*, 37(6):1610–1627.

Killworth, P. D.
2001. Rossby waves. *San Diego, USA, Academic Press*, 1(In, Steele, John H., Thorpe, Steve A. and Turekian, Karl K. (eds.) Encyclopedia of Ocean Sciences):2434–2443.

Killworth, P. D., D. B. Chelton, and R. A. de Szoeke
1997. The speed of observed and theoretical long extratropical planetary waves. *Journal of Physical Oceanography*, 27(9):1946–1966.

Koblinsky, C. J.
1990. The global distribution of f / H and the barotropic response of the ocean. *Journal of Geophysical Research*, 95(C3):3213–3218.

Krug, M. and J. Tournadre
2012. Satellite observations of an annual cycle in the Agulhas Current. *Geophysical Research Letters*, 39(15).

Lau, K. M. and H. Weng
1999. Interannual, decadal-interdecadal, and global warming signals in sea surface temperature during 1955-97. *Journal of Climate*, 12(5):1257–1267.

le Bars, D. L. B., H. A. Dijkstra, and W. P. M. De Ruijter
2013. Impact of the Indonesian Throughflow on Agulhas leakage. *Ocean Science Discussions*, 10:353–391.

Leber, G. M. and L. M. Beal
2015. Local water mass modifications by a solitary meander in the Agulhas Current. *Journal of Geophysical Research C: Oceans*, 120(6):4503–4515.

Ledwell, J. R., A. J. Watson, and C. S. Law
1998. Mixing of a tracer in the pycnocline. *Journal of Geophysical Research: Oceans*, 103(C10):21499–21529.

Lee, T. N., W. E. Johns, C.-T. T. Liu, D. Zhang, R. J. Zantopp, and Y. Yang
2001. Mean transport and seasonal cycle of the Kuroshio east of Taiwan with comparison to the Florida Current. *Journal of Geophysical Research: Oceans*, 106(C10):22143–22158.

Lund, D. C., J. Lynch-Stieglitz, and W. B. Curry
2006. Gulf Stream density structure and transport during the past millennium. *Nature*, 444(7119):601–604.

Lutjeharms, J. R. E.
2006. The Agulhas Current. *Springer, Berlin, Heidelberg, New York*, ISBN-10: 3.

Lutjeharms, J. R. E. and W. P. M. De Ruijter
1996. The influence of the Agulhas Current on the adjacent coastal ocean: possible impacts of climate change. *Journal of Marine Systems*, 7(2-4):321–336.

Lutjeharms, J. R. E. and R. C. Van Ballegooyen
1988. The retroflection of the Agulhas Current. *Journal of Physical Oceanography*, 18(11):1570–1583.

Matano, R. P., E. J. Beier, and P. T. Strub
2008. The seasonal variability of the circulation in the South Indian Ocean Model and observations. *Journal of Marine Systems*, 74(1):315–328.

Matano, R. P., E. J. Beier, P. T. Strub, and R. Tokmakian

2002. Large scale forcing of the Agulhas variability: The seasonal cycle. *Journal of Physical Oceanography*, 32(4):1228–1241.

Matano, R. P., C. G. Simionato, and P. T. Strub

1999. Modeling the Wind-Driven Variability of the South Indian Ocean. *Journal of Physical Oceanography*, 29(2):217–230.

Meinen, C. S., M. O. Baringer, and R. F. Garcia

2010. Florida Current transport variability: An analysis of annual and longer period signals. *Deep-Sea Research Part I: Oceanographic Research Papers*, 57(7):835–846.

Mellor, G. and R. X. Huang

1997. Introduction to Physical oceanography. *American Journal of Physics*, 65(10).

Meyers, G.

1979. On the annual Rossby wave in the tropical North Pacific Ocean.

Munk, W. H.

1966. Abyssal recipes. In *Deep Sea Research and Oceanographic Abstracts*, volume 13, Pp. 707–730. Elsevier.

Niiler, P. P.

1973. Seasonal variability of florida current. *Journal of Marine Research*, 31(3):144–167.

Njouodo, A. S. N., S. Koseki, N. Keenlyside, and M. Rouault

2018. Atmospheric signature of the Agulhas Current. *Geophysical Research Letters*.

Nof, D.

1983. On the response of ocean currents to atmospheric cooling. *Tellus A*, 35(1):60–72.

Ou, H. W. and W. P. M. De Ruijter

1986. Separation of an inertial boundary current from a curved coastline. *Journal of Physical Oceanography*, 16(2):280–289.

Pedlosky, J.

1971. Geophysical fluid dynamics. *Mathematical Problems in the Geophysical Sciences*, 1:1–60.

Pedlosky, J.

1987. *Geophysical fluid mechanics*, second edi edition. Springer-Verlag.

Pond, S. and G. L. Pickard

2013. *Introductory dynamical oceanography*. Elsevier.

Qiu, B. and R. Lukas

1996. Seasonal and interannual variability of the North Equatorial Current, the Mindanao Current, and the Kuroshio along the Pacific western boundary. *Journal of Geophical Research*, 101(C5):12,312–315,330.

Qiu, B., W. Miao, and P. Muller

1997. Propagation and Decay of Forced and Free Baroclinic Rossby Waves in Off Equatorial Oceans. *Journal of Physical Oceanography*, 27(11):2405–2417.

Reason, C. J. C.

2001. Evidence for the influence of the Agulhas Current on regional atmospheric circulation patterns. *Journal of Climate*, 14(12):2769–2778.

Reason, C. J. C., J. R. E. Lutjeharms, J. Hermes, A. Biastoch, and R. E. Roman

2003. Inter-ocean fluxes south of Africa in an eddy-permitting model. *Deep Sea Research Part II: Topical Studies in Oceanography*, 50(1):281–298.

Ridderinkhof, H., P. M. Van der Werf, J. E. Ullgren, H. M. Van Aken, P. J. Van Leeuwen, and W. P. M. De Ruijter

2010. Seasonal and interannual variability in the Mozambique Channel from moored current observations. *Journal of Geophysical Research: Oceans (1978-2012)*, 115(C6).

Ridgway, K. R.

2007. Long-term trend and decadal variability of the southward penetration of the East Australian Current. *Geophysical Research Letters*, 34(13).

Ridgway, K. R. and J. S. Godfrey

1997. Seasonal cycle of the East Australian current. *Journal of Geophysical Research: Oceans*, 102(C10):22921–22936.

Risien, C. M. and D. B. Chelton

2008. A Global Climatology of Surface Wind and Wind Stress Fields from Eight Years of QuikSCAT Scatterometer Data. *Journal of Physical Oceanography*, 38(11):2379–2413.

Rousset, C. and L. M. Beal

2011. On the seasonal variability of the currents in the Straits of Florida and Yucatan Channel. *Journal of Geophysical Research: Oceans*, 116(8):1–17.

Roxy, M. K., K. Ritika, P. Terray, and S. Masson

2014. The curious case of Indian Ocean warming. *Journal of Climate*, 27(22):8501–8509.

Sato, O. T. and T. Rossby

1995. Seasonal and low frequency variations in dynamic height anomaly and transport of the Gulf Stream. *Deep Sea Research Part I: Oceanographic Research Papers*, 42(1):149–164.

Schott, F. A., S.-P. Xie, and J. P. McCreary Jr

2009. Indian Ocean Circulation and Climate Variability. *Reviews of Geophysics*, 47(2007):1–46.

Schouten, M. W., W. P. M. de Ruijter, and P. J. van Leeuwen

2002. Upstream control of Agulhas Ring shedding. *Journal of Geophysical Research: Oceans (1978-2012)*, 107(C8):11–23.

Schouten, M. W., W. P. M. Ruijter, P. J. Leeuwen, and J. R. E. Lutjeharms
2000. Translation, decay and splitting of Agulhas rings in the southeastern Atlantic Ocean. *Journal of Geophysical Research: Oceans*, 105(C9):21913–21925.

Shchepetkin, A. F. and J. C. McWilliams
2005. The regional oceanic modeling system (ROMS): a split-explicit, free-surface, topography-following-coordinate oceanic model. *Ocean Modelling*, 9(4):347–404.

Shinoda, T., W. Han, E. J. Metzger, and H. E. Hurlburt
2012. Seasonal variation of the Indonesian Throughflow in Makassar Strait. *Journal of Physical Oceanography*, 42(7):1099–1123.

Siedler, G., J. Gould, and J. A. Church
2001. *Ocean circulation and climate: observing and modelling the global ocean*, volume 103. Academic Press.

Sprintall, J., S. E. Wijffels, R. Molcard, and I. Jaya
2009. Direct estimates of the Indonesian Throughflow entering the Indian Ocean: 2004-2006. *Journal of Geophysical Research: Oceans*, 114(C7).

Stommel, H.
1948. The westward intensification of wind-driven ocean currents. *Eos, Transactions American Geophysical Union*, 29(2):202–206.

Stommel, H.
1965. The Gulf Stream, A Physical and Dynamical Description, 248 pp. *Univ.of Calif.Press, Berkeley.*

Stramma, L. and J. R. E. Lutjeharms
1997. The flow field of the subtropical gyre of South Indian Ocean. *Journal of Geophysical Research*, 102(C3):5513–5530.

Subrahmanyam, B., I. S. Robinson, J. R. Blundell, and P. G. Challenor
2001. Indian Ocean Rossby waves observed in TOPEX/POSEIDON altimeter data and in model simulations. *International Journal of Remote Sensing*, 22(1):141–167.

Sverdrup, H. U.
1947. Wind-Driven Currents in a Baroclinic Ocean; with Application to the Equatorial Currents of the Eastern Pacific. *Proceedings of the National Academy of Sciences of the United States of America*, 33(11):318–326.

Talley, L. D.
2011. *Descriptive physical oceanography: an introduction*. Academic press.

Vallis, G. K.
2017. *Atmospheric and oceanic fluid dynamics*. Cambridge University Press.

van Leeuwen, P. J., W. P. M. de Ruijter, J. R. E. Lutjeharms, P. J. Leeuwen, W. P. M. Ruijter, and J. R. E. Lutjeharms
2000. Natal pulses and the formation of Agulhas rings. *Journal of Geophysical Research*, 105(C3):6425–6436.

Van Sebille, E., L. M. Beal, and A. Biastoch
2010. Sea surface slope as a proxy for Agulhas Current strength. *Geophysical Research Letters*, 37(9):2–5.

Wang, L., C. J. Koblinsky, and S. Howden
2001. Annual Rossby Wave in the Southern Indian Ocean: Why Does It "Appear" to Break Down in the Middle Ocean? *Journal of Physical Oceanography*, 31:54–74.

White, W. B.
1977. Annual Forcing of Baroclinic Long Waves in the Tropical North Pacific Ocean.

Zhai, X., H. L. Johnson, and D. P. Marshall
2010. Significant sink of ocean-eddy energy near western boundaries. *Nature Geoscience*, 3(9):608–612.